SANDIA REPORT

SAND2015-2373
Unlimited Release
Printed March 2015

Supersedes SAND2015-2373
Dated March 2015

Development of Quality Assessment Techniques for Large Eddy Simulation of Propulsion and Power Systems in Complex Geometries

Guilhem Lacaze (PI) and Joseph C. Oefelein,

with the collaboration of A. Ruiz, L. Hakim, M. Khalil and H. Najm.

Prepared by
Sandia National Laboratories
Albuquerque, New Mexico 87185 and Livermore, California 94550

Sandia National Laboratories is a multi-program laboratory managed and operated by Sandia Corporation, a wholly owned subsidiary of Lockheed Martin Corporation, for the U.S. Department of Energy's National Nuclear Security Administration under contract DE-AC04-94AL85000.

Sandia National Laboratories

Issued by Sandia National Laboratories, operated for the United States Department of Energy by Sandia Corporation.

Available to DOE and DOE contractors from
U.S. Department of Energy
Office of Scientific and Technical Information
P.O. Box 62
Oak Ridge, TN 37831

Telephone: (865) 576-8401
Facsimile: (865) 576-5728
E-Mail: reports@adonis.osti.gov
Online ordering: http://www.osti.gov/bridge

Available to the public from
U.S. Department of Commerce
National Technical Information Service
5285 Port Royal Rd
Springfield, VA 22161

Telephone: (800) 553-6847
Facsimile: (703) 605-6900
E-Mail: orders@ntis.fedworld.gov
Online ordering: http://www.ntis.gov/help/ordermethods.asp?loc=7-4-0#online

SAND2015-2373
Unlimited Release
Printed March 2015
Reprinted March 2015

Supersedes SAND2015-2373
dated March 2015

Development of Quality Assessment Techniques for Large Eddy Simulation of Propulsion and Power Systems in Complex Geometries

Guilhem Lacaze (PI)
Combustion Research Facility
Sandia National Laboratories
P.O. Box 969
Livermore, CA 94551-0969
gnlacaz@sandia.gov

Joseph C. Oefelein
Combustion Research Facility
Sandia National Laboratories
P.O. Box 969
Livermore, CA 94551-0969
oefelei@sandia.gov

The collaborative contributions from
Anthony Ruiz,
Layal Hakim,
Mohammad Khalil and Habib Najm
are gratefully acknowledged.

Abstract

Large-eddy-simulation (LES) is quickly becoming a method of choice for studying complex thermo-physics in a wide range of propulsion and power systems. It provides a means to study coupled turbulent combustion and flow processes in parameter spaces that are unattainable using direct-numerical-simulation (DNS), with a degree of fidelity that can be far more accurate than conventional engineering methods such as the Reynolds-averaged Navier-Stokes (RANS) approximation. However, development of predictive LES is complicated by the complex interdependence of different type of errors coming from numerical methods, algorithms, models and boundary conditions. On the other hand, control of accuracy has become a critical aspect in the development of predictive LES for design. The objective of this project is to create a framework of metrics aimed at quantifying the quality and accuracy of state-of-the-art LES in a manner that addresses the myriad of competing interdependencies. In a typical simulation cycle, only 20% of the computational time is actually usable. The rest is spent in case preparation, assessment, and validation, because of the lack of guidelines. This work increases confidence in the accuracy of a given solution while minimizing the time obtaining the solution. The approach facilitates control of the tradeoffs between cost, accuracy, and uncertainties as a function of fidelity and methods employed. The analysis is coupled with advanced Uncertainty Quantification techniques employed to estimate confidence in model predictions and calibrate model's parameters. This work has provided positive consequences on the accuracy of the results delivered by LES and will soon have a broad impact on research supported both by the DOE and elsewhere.

Contents

List of Figures

List of Tables

Chapter 1

Introduction

The current dilemma that the computational fluid dynamics field is currently facing is that the capacity of computers are following an exponential curve while the use of simulation solvers as predictive tools remains very scarce. The main reason is the lack of a proper method to assess the quality of predictions as errors or uncertainties in a flow solver are very difficult to understand, quantify and subsequently control. This is even more the case in Large Eddy Simulation due to the complexity of the solver and models. The objective of the present project is to create a comprehensive framework of metrics aimed at quantifying the quality and accuracy of state-of-the-art LES in a manner that addresses the myriad of competing interdependencies. The goal is to significantly increase confidence in the accuracy of a given solution while minimizing the time obtaining the solution. The approach proposed here will facilitate control of the tradeoff's between cost, accuracy, and uncertainties as a function of fidelity and methods employed. The complexity of the issue of confidence in numerical results is exemplified when the exact same physical problem is tackled by different different solvers based on different numerical and physical frameworks. For example, a flame stabilized behind a triangular flame-holder has been simulated using four different LES solvers from Standford, Georgia Institute of Technology, OpenCFD and Fluent. The same grid and boundary conditions have been employed. This exercise showed that the flame shape and behavior were very different between the approaches. This can even be the case using the same solver just by changing the numerical formulation.

This lack of confidence in numerical results comes from four major aspects: (1) many sources of uncertainties are not controlled in current simulation tools, (2) they come from uncertainties of very different nature (model errors, numerical errors, measurement errors, interpretation errors, etc.), (3) they are coupled in very non-linear manners and (4) some errors are cumulative and depend on the "history" of the simulation.

Points (1) and (2) are shown in Fig. 1.1 that presents the network of the most common error sources present in a Computational Fluid Dynamic (CFD) solver. Error are introduced at different levels; some are very fundamental such as the "choice of the relevant physics" and some are more related to the mathematical framework such as "discretization errors". Point (3): the intricate coupling between errors is not described in this figure. These non-linear connections between uncertainties can be observed if we just focus on model errors in the case of a stable lifted turbulent flame. In this configuration, the following physical processes are present: the fuel jet creates turbulence, leading to turbulent mixing that generates a flammable mixture, the mixture ignites, producing a flame and the flame may stabilize by propagation mechanism (or other mechanisms depending on conditions). Figure 1.2 illustrates these couplings and presents the complex feedback loops that are present in such flows. This shows that if one wants to evaluate the accuracy

of a combustion closure, he/she must ensure that mixing is correctly captured. Indeed, a correct combustion closure can result in an incorrect flame stabilization height (if mixing is not correct) while an erroneous combustion closure may result in the correct height due to error compensation. On the other hand, when the feedback loops shown in Fig. 1.2 are strong (in flame–acoustic interaction for example), it is very complicated to evaluate the accuracy of the combustion model as its outputs (the dynamic of the flame, temperature, and so on) directly impact its inputs (pressure field, upstream flow, mixture state, and so on), and both the combustion closure and the acoustic coupling mechanism have to be correctly accounted for to give the right answer. The fourth characteristics (point 4) that makes error identification very complex is the cumulative behavior of certain errors. If one measures an error between numerical and reference data at a given space-time location $(\mathbf{x},t)$, this error is the accumulation of all errors produced at different space-time locations that have an influence on $(\mathbf{x},t)$. In the case of an incompressible and invicid flow the error at a $(\mathbf{x},t)$ location depends on the sum of all "up-stream" errors produced along the flow path passing through $(\mathbf{x},t)$. This effect results from the fact that information is transported throughout the computation due to various mechanisms. This can make the detection of error sources very difficult. Those complex coupling and cumulative behavior can also result in error cancellation and very non-linear behavior in error prediction. This has been shown by the pioneer work of Meyers et al. [4, 5] and a method called error-landscape has been developed. It inherently accounts for the competing effects of numerical and modeling errors simultaneously. Those different studies demonstrated that errors from models and numerical operators can cancel each other leading to non-intuitive minima in the error landscape. This approach has recently been used by Kempf et al. [6] to analyze error cancellation in a LES simulation of a combustion burner.

Despite all those difficulties significant work has been dedicated to error assessment in computational fluid dynamics of turbulent flows. Two main frameworks have been tackling uncertainties in simulations, namely (1) probabilistic approaches based on Bayesian probabilities [7, 8], and (2) deterministic approaches focusing on error analysis [9], [10], [11], [12], [13]. The probabilistic approach (or Uncertainty Quantification method: UQ) is based on the notion that a certain level of stochasticity influences simulation results. Hence uncertainties can be quantified by analyzing a large number of simulation results where models, boundary conditions, grid spacing are varied. Reviews of this type of techniques can be found in [14] and [15]. The classical method is the Monte Carlo sampling that requires a large number of simulation runs to be performed with semi-random perturbations of inputs. In the LES context this approach is not realistic as the number of samples is usually in the order of 10^5. Most of probabilistic methods for LES rely on the Monte Carlo concept but are developed around efficient techniques such as surrogate construction [16] [17]. For example, the identification of an envelop of uncertainties in simulation results can be achieved by polynomial chaos expansions (PCE) [18, 19] . Simulation results are required only at specific quadrature points to build an accurate surrogate that mimics the LES model and can be used to produce the amount of samples required for statistical analysis. The main problem with this framework is that it has rarely been applied to LES due to the cost of the simulation. It is not yet clear if methods can be used directly or if multi-dimensional approaches are required. The present work has explored these methods and clear benefits have been shown.

The deterministic approach is based on a different concept: simulations results are completely deterministic meaning that for a set of inputs the outcomes will always be the same, hence statistical sampling is not necessary. Terms describing the different sources of errors presented earlier are

identified and deterministic uncertainties can be calculated on quantities of interest. Error indicators have been derived by various groups and reviews on the subject are presented in [11] and [20]. Previous studies aimed at understanding and improving the accuracy of LES mainly focused on the impact of grid resolution on simulation accuracy. Criteria have been developed to assess LES quality in simple geometries, under simple conditions (single phase, low turbulence intensity, non-reacting). Similarly, various algebraic error indicators (such as the Pope 80% criterion) have been developed in an attempt to provide some guiding metrics (see for example [21] and [11]). In TNF9 (Montreal Canada, 2009), algebraic error indicators were applied to the HM1 bluff-body flame to explore their utility in the context of more complex flows including flames and conditions closer to real burner operating points. Those indicators compare the information (turbulent kinetic energy, dissipation,...) resolved in the simulation with the information that is missing in the simulation and reconstructed from model activity. This however can lead to a paradox. For example, in the case of a very poorly resolved LES, the turbulent flow becomes laminar (due to spatial filtering mostly) and the contribution of the model vanishes. The resolved kinetic energy becomes equal to the total energy and the criterion indicates that the LES is of "good" quality, which it is not the case as the dynamics of the flow has been profoundly altered. Also a major deficiency with the quality indicators used to date is that none of them account for the various sources of error rigorously. Only the bulk error from multiple competing sources has been considered instead of the distinct sources of error. Discretization and modeling associated with LES introduces three distinct forms of error: (1) discretization errors associated with the numerical techniques (i.e., temporal integration, spatial differencing, and related stabilization schemes), which can induce damping and dispersion of the broadband flow processes; (2) the total model residual error, which is caused by discretization of the sub-models themselves; and (3) the error associated with the model approximation itself due to both the basic model assumptions and the related range of subgrid- or subfilter- scales it is specified to work over.

A current consensus is that deterministic approaches lack a clear metric to assess quality and the UQ methods are promising but difficult to apply in a LES context. The purpose of the present project is to (1) define a better system of metrics to assess quality in LES and (2) to test non-intrusive UQ methods to estimate model accuracy. For this work, the high-fidelity LES solver Raptor has been used as a numerical platform to perform the different tests. This theoretical framework was developed by Oefelein [22, 23, 24].It provides unified treatment of high Reynolds-number, high-pressure, real-gas/liquid, reacting flows over a wide Mach operating range. It has been used to study non-reacting and reacting flows [25, 22, 26, 23, 24].

This report is organized as followed, in the following section metrics are identified to assess the quality of LES and tested in two different configurations. Then advanced UQ approaches developed at Sandia are evaluated with the present LES framework. Those methods are used to establish accuracy of closures and calibrate models. Conclusions are drawn and the impact of the project is discussed before presenting current and future work.

Figure 1.1. Error network in computational fluid dynamics (errors are framed in red). In the present study, only the errors framed in bold are of interest.

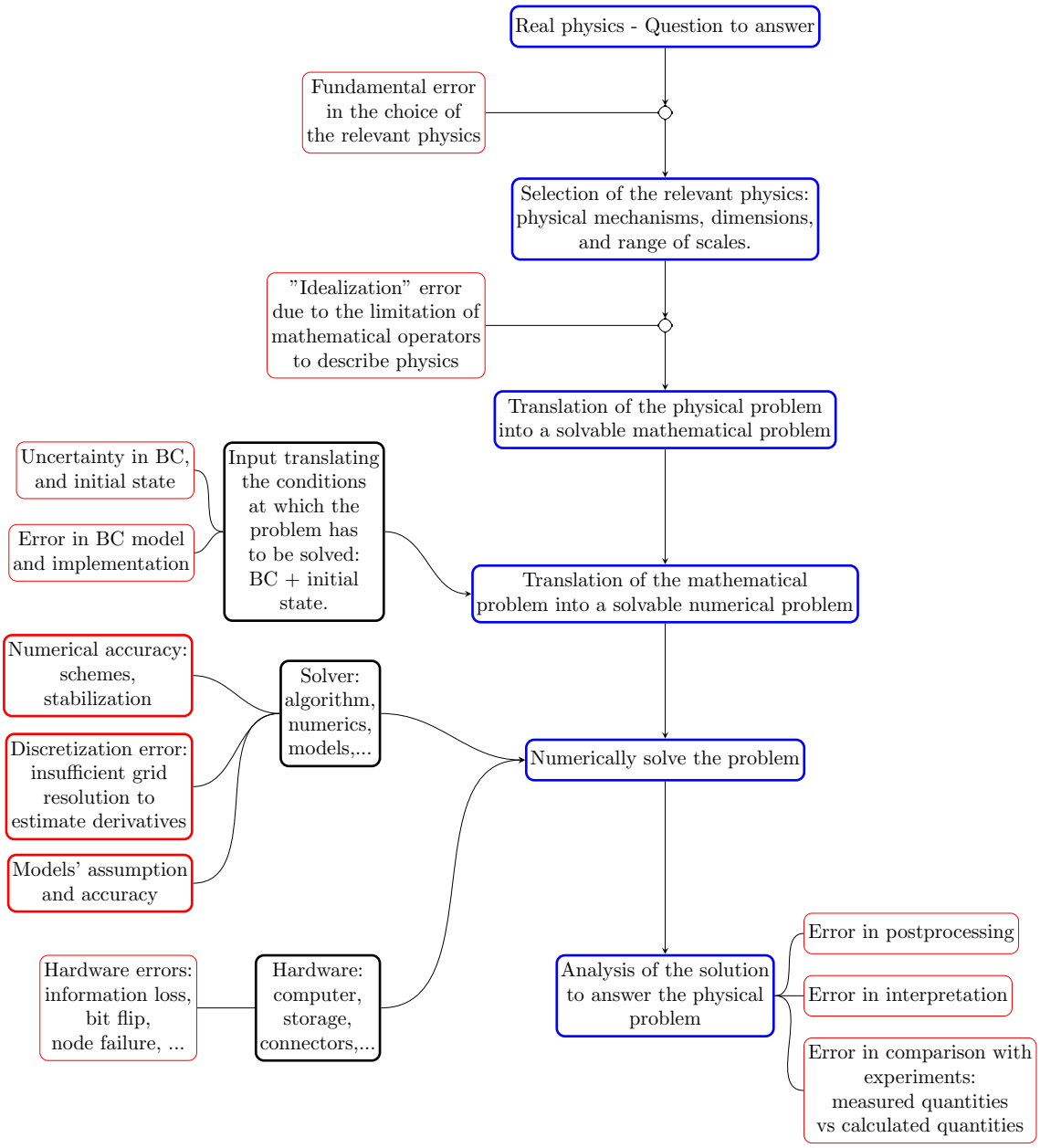

Figure 1.2. Example of coupling between models for the case of a stable turbulent lifted flame.

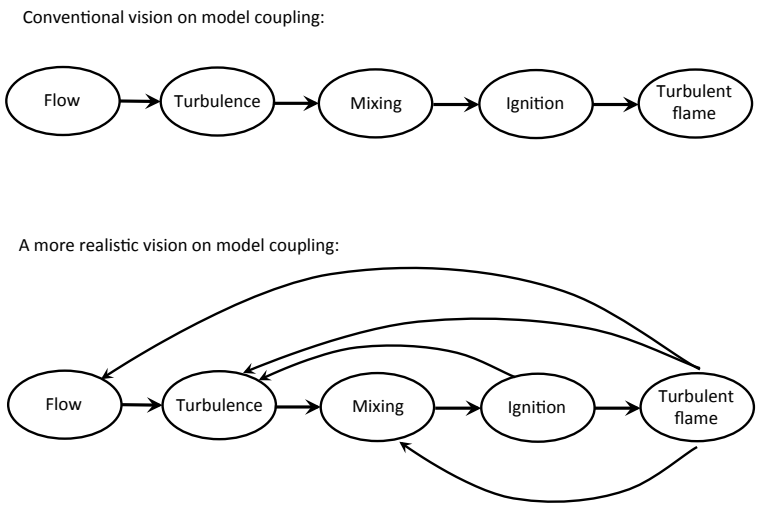

This page intentionally left blank.

Chapter 2

Quality metrics

Grid spacing is one of the most important parameter in LES as it has a direct impact on the accuracy of the models and numerics. The question we want to answer in this section is how to evaluate the required grid spacing in a high-fidelity LES simulation and what metrics to use to quantify the accuracy. Two types of metrics have been considered. The first one is based on statistically converged turbulent moments (namely mean and rms) of flow quantities (scalars and velocities). The second one is the power density spectra of the fluctuation energy of flow quantities. The advantage of the first type is that a direct comparison with experimental measurements is possible. The second however contains more information concerning the local turbulent mechanisms and can be used to detect abnormal behavior of the flow due to contamination from the numerical framework. For this study a sequence of cases have been considered with increasing geometrical complexity. First a simple two-dimensional mixing layer has been analyzed with a particular focus on grid refinement. Then a full three-dimensional jet in a cross-flow has been studied to test and improve the established set of metrics.

Turbulent mixing and combustion at high-pressure occurs in many high-performance propulsion and power systems such as Liquid Rocket Engines (LREs), diesel engines, and modern gas turbines. These systems are characterized by large Reynolds numbers, large density ratios between the propellants, and high operating pressures. Chamber pressures often exceed the thermodynamic critical pressure of the injected fluids, which involves significant phenomenological changes in the dynamics of both non-reacting and reacting shear flows. At subcritical pressure, mixing is dominated by atomization and evaporation of droplets whereas at supercritical pressures, mixing is mainly governed by turbulent mixing and diffusion. A comprehensive description of available experimental work is presented in the reviews of Oschwald et al. [27] and Chehroudi [28]. The configurations that are generally studied are dense liquid jets injected in a chamber of quiescent gaseous mixture and assisted by a coaxial stream. For the present non-reacting conditions, the data available includes: 1) mean longitudinal profiles of a scalar (temperature, density or mass fraction) along the jet axis [29], 2) radial profiles of a scalar downstream of the jet exit [30, 31, 32, 33], and 3) measurements of the 'dense core' (also called 'dark-core') length [34, 33, 35, 36] and jet angle [32, 37]. A problem at these conditions, however, is that the time and space resolution of the measurements are limited by beam-steering and line-of-sight spatial averaging. This prevents quantification of the intermediate and small scales of turbulence, which in turn prevents thorough validation of Computational Fluid Dynamics (CFD) calculations.

In addition to the lack of validation data, many ambiguities remain to be solved in numerical

tools. At a physical level, the treatment of high-pressure thermodynamics requires sophisticated methods to account for the non-linearities occurring near the pseudo-evaporation line. At the numerical level, advanced schemes and stabilization methods must be employed to limit errors and preserve accuracy. Benchmark data such as that provided here offers missing information required to assess these methods.

To address these challenges, various Direct Numerical Simulations (DNS) have been carried out at reduced Reynolds numbers and low density ratios [38, 39, 40, 41, 42, 43, 44]. These investigations have shown the impact of high-pressure non-idealities on mixing in three-dimensional temporal mixing layers. DNS at actual conditions is still out of reach, even with the best supercomputers available today. DNS at conditions typically found in rocket combustors or diesel engines (with a characteristic Reynolds number of 10^5 and density ratio of 100) would require a three-dimensional grid that is more than ten-million times larger that the largest grids used today on the fastest supercomputers. Considering the current rate at which computational capabilities evolve, DNS of actual devices will not be possible even ten years from now.

The next best approach to treat this type of flows is the Large-Eddy Simulation (LES) technique. LES has been employed to predict high-Reynolds number flows at elevated pressures [25, 45, 22, 23, 46, 47, 48, 49, 50, 51, 52, 53]. In these studies extreme gradients are created by the coupling of very large density ratios and strong turbulent strain rates inside complex shear layers. As the resolution of all scales is not possible, various methods have been tested to avoid spurious numerical oscillations. In [25, 46, 22], upwinding of the convective fluxes is used to transport stiff scalar gradients. In [50], artificial viscosity is added to the species transport equations, coupled with a pressure correction term in the energy equation. Similar artificial stabilization approaches have been developed in [54, 53] considering different tradeoffs between errors and energy conservation. Despite the high level of sophistication of these methods, the absence of detailed data for validation significantly limits the development of predictive approaches at relevant conditions.

The objective of the present work is to provide detailed data in a configuration containing the essential features of real devices (geometry, thermodynamics and dynamics) while being simple enough to make it accessible to other research groups using different type of numerical approaches (structured, unstructured, LES and RANS).

To improve confidence in the results, two state-of-the-art solvers have been used to generate the database. Despite the very distinct numerical formalisms, results are very comparable, which demonstrates the robustness of the findings. The second novelty of the present work is the grid convergence study, which has never been conducted in such a configuration, and which quantifies the required spatial resolution. The results presented are currently the most detailed at these conditions.

In the following we first describe the benchmark configuration along with a concise description of the codes. We then focus on the procedure and details on the collection of statistics are provided before presenting the core of the analysis based on a grid convergence study.

Benchmark configuration

Description of the case

The goal of the present benchmark is to provide a platform for solver validation in the context of highly turbulent flows presenting large density ratios. The configuration has been selected based on the following constraints:

- Relevant conditions for real devices such as rocket combustors and diesel engines (large Reynolds number, typical characteristic size, detailed real-fluid thermodynamics and transport)
- Representative geometrical features (including injector lip)
- Perfect control of boundary conditions to facilitate accessibility by different solvers
- Computationally affordable.

We chose the mixing layer generated behind the lip of an injector in a cryogenic rocket engine as it complies to all the listed requirements. This configuration has been studied by several teams [25, 45, 22, 23, 47, 48] without being fully validated. We consider a two−dimensional mixing layer with an injector lip that separates liquid-oxygen (LOX) and gaseous-hydrogen (GH_2) streams at supercritical pressure (with respect to oxygen). A sketch of the computational domain

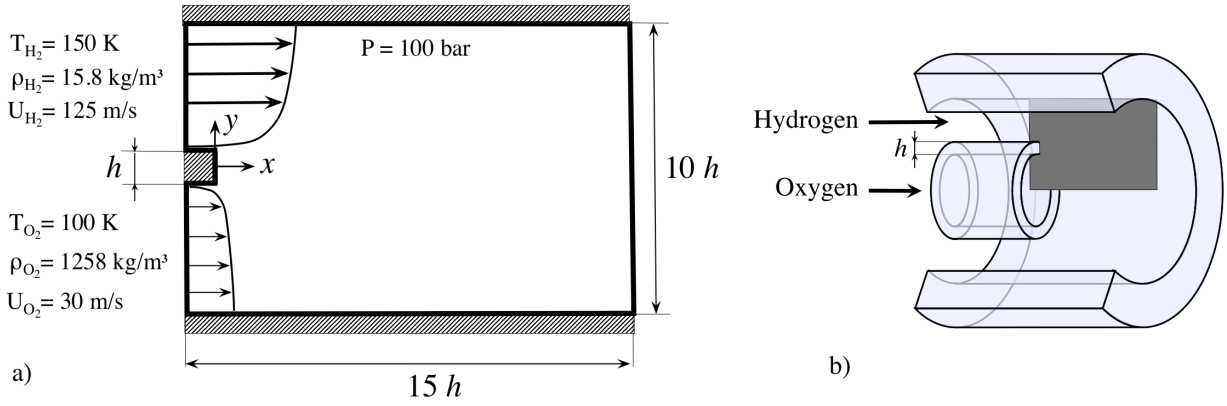

Figure 2.1. a) Boundary conditions for the 2D computational domain ($h = 0.5$ mm). b) Typical coaxial injector of a LRE (the grey frame represents the two−dimensional simulation domain).

is displayed in Fig. 2.1a while Fig. 2.1b highlights its similarity to coaxial injectors in LREs. A

central dense oxygen jet is sheared by a high-speed coaxial hydrogen stream. This configuration allows a good control of mixing and flame stabilization in real engines. The geometrical simplicity of the computational domain allows the use of the same mesh in structured and unstructured solvers, which removes ambiguities linked to the mesh type. Even though a 2D simulation has potential limitations in terms of the turbulent mixing characteristics, a 3D simulation has serious limitations as a benchmark configuration due to the computational cost at the inherently high Reynolds numbers. From this perspective, the 2D domain used here provides a good compromise. Furthermore, Chehroudi [55] compared favorably the opening angle of cryogenic round jets to plane mixing-layers, which tends to indicate that eddies are mainly two−dimensional at early stages, close to the injector lip. Thus, although the flow is not strictly two−dimensional, the fundamental mechanisms of turbulent mixing are present.

Boundary Conditions

In the present configuration, a lip height of $h = 0.5$ mm separates the two streams, which is also a representative value for LREs. The ambient pressure is $P = 10$ MPa, about twice as much as the critical point of O_2 (5.04 MPa). The inner dense oxygen jet has a velocity of U^{inj}=30 m/s and the Mach number is $\mathrm{Ma}^{inj} = 0.04$. The outer light hydrogen jet has a velocity of $U^{inj} = 125$ m/s and Mach number of $\mathrm{Ma}^{inj} = 0.12$. The large shear induced by the velocity difference between the jets triggers turbulent mixing. The density ratio between the oxygen stream and the hydrogen stream is equal to 80, with $\rho_{O_2} = 1258$ kg/m^3 and $\rho_{H_2} = 15.8$ kg/m^3. Using the lip height as the reference length, the Reynolds number in each stream is defined as:

$$Re = \rho h U^{inj} / \mu \tag{2.1}$$

with $\mu_{H2} = 5\ 10^{-6}$ Pa.s and $\mu_{O2} = 4\ 10^{-4}$ Pa.s, we find $Re_{H_2} = 2\ 10^5$ and $Re_{O_2} = 5\ 10^4$. The boundary conditions are illustrated in Fig. 2.1a. A $1/7^{th}$ power law for the inlet velocities in both streams is used to mimic the mean velocity profile in a turbulent pipe flow:

$$u(y) = U^{inj} \left((y - y_{\mathrm{wall}}) / \delta_\omega \right)^{1/7}, \tag{2.2}$$

where U^{inj} is the injection velocity and $y - y_{\mathrm{wall}}$ is the distance to the injector wall. The Reynolds number is thus sufficiently large in each stream for the flow to naturally transition to turbulence in the wake of the lip, and no velocity perturbations is added to the inflow. The thickness of the vorticity profile at the inlet, as well as the height of the injector lip, determines the characteristics (wavelength and frequency) of the coherent structures developing in the turbulent mixing layer downstream of the injector [56]. A value of $\delta_\omega = 4.5h$ is used, which gives a momentum thickness at the inlets that is comparable to the lip height. The upper and lower boundaries are slipping walls while the lip is an adiabatic no-slip wall. The outlet pressure is 10 MPa.

Initial Conditions

To initialize the simulation, the inlet boundary conditions are swept through the whole domain. A hyperbolic tangent profile $\theta(y)$ for the O_2 mass fraction and the temperature is used behind the lip ($-0.5h < y < 0.5h$) associated with a zero velocity zone, as shown in Fig. 2.2. The profile is:

$$\theta(y) = \tanh((y - y_{\text{wall},O_2})/\delta_i), \tag{2.3}$$

where $y_{\text{wall},O_2} = 4.5h$ and $\delta_i = h/4$. The temperature and mass fraction profiles are then set equal to:

$$T(y) = T_{O_2} + (T_{H_2} - T_{O_2})\,\theta(y) \tag{2.4}$$

$$Y_{H_2}(y) = \theta(y). \tag{2.5}$$

The thickness of the initial hyperbolic tangent profile is chosen so that the oxygen and temperature gradient thicknesses are initially resolved on more than 5 grid points with the coarsest mesh spacing, which has 30 points within the lip height (the grid and spatial resolution are described latter). Note that the initial profiles do not have any impact on the final results as transients are flushed

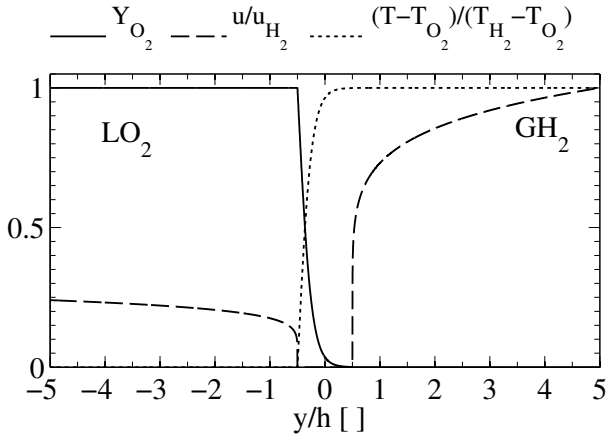

Figure 2.2. Transverse cut through the initial solution downstream the lip ($T_{H_2} = 150$ K, $T_{O_2} = 100$ K, $u_{H_2} = 125$ m/s and $h = 0.5$ mm).

during the initialization phase, before recording any statistics. The procedure to obtain statistics independent of initial conditions is presented in Section 2.

Geometry and Grid

The dimensions of the configuration are presented in Fig. 2.1a. The unit distance is the thickness of the lip $h = 0.5$ mm. The lip is $1h$ long. The computational domain is $10h$ wide in the y-direction and $15h$ long in the x-direction. The region of interest expends from 0 to $10h$ in the x-direction. A sponge layer is placed before the exit to prevent spurious acoustic wave generation due to outgoing hydrodynamic structures. To avoid any undesirable effect of stretching, the grid spacing is constant in the x and y-directions in the region where eddies develop: $3h$ in the y-direction (centered on the lip) and $10h$ in the x-direction. To save computational time, a small stretching is applied outside this region where no eddies are present and follows an amplification factor of 1% in the y-direction only.

Description of the solvers

To establish quantitative Benchmark data that is independent of the solver used, we have performed back-to-back comparisons of the results using two different solvers. Each has distinct state-of-the-art numerical frameworks. The initialization, boundary conditions, and physical models are synchronized as much as possible. This facilitates analysis of the sensitivity of the detailed validation data on numerical methods. When agreement is observed, numerical predictions are accurate and not influenced by numerical characteristics. When deviations are observed, one can investigate their origin. Following is a concise description of each of the solvers used.

The AVBP solver is a massively parallel CFD solver co-developed by CERFACS and IFP Energies Nouvelles. AVBP has been used in many different industrial applications ranging from gas turbines [57, 58, 59] and piston engines [60, 61] to scramjets [62]. An overview of the solver properties and recent applications are presented in [63, 64]. In the context of supercritical studies, AVBP has been used to study non-reacting supercritical nitrogen round jets in [50] and [52] and in reacting studies of coaxial jets [51].

RAPTOR has been described in the introduction and will then not be detailed here.

Simulation procedure and impact of grid spacing

Simulation sequence and temporal average procedure

Before analyzing the results, two points have to be clarified. 1) How long does it take to flush the initial solution and reach steady state? 2) How long the simulation should be run to get temporal convergence and meaningful statistics? To define these two periods a characteristic time of the configuration must be identified. Based on the convective velocity of coherent structures in the mixing layer, a flow-through-time is derived. The convective velocity is evaluated using the

expression given in [65, 66]:

$$U_{conv} = \frac{U_{O_2}^{inj} + \left(\frac{\rho_{H_2}}{\rho_{O_2}}\right)^{1/2} U_{H_2}^{inj}}{1 + \left(\frac{\rho_{H_2}}{\rho_{O_2}}\right)^{1/2}} \tag{2.6}$$

Here $U_{conv} = 39.6$ m/s which is in good agreement with the evaluation provided in [67] for the current case. The flow-through-time in the present configuration is then defined using the length of the zone of interest ($10h$):

$$T_{ft} = \frac{10h}{U_{conv}} = 0.125 \text{ ms}. \tag{2.7}$$

The temporal evolutions of the main quantities (T, P, U, V, Y_{O_2}) recorded of various locations in the mixing layer showed that steady state is reached after 20 T_{ft} starting from the initial solution. From $t = 10\ T_{ft}$, three different time-averaging period have been compared: 10 T_{ft}, 15 T_{ft} and 20 T_{ft}. For the comparison, the transverse 1D profiles at $x = 5h$ (middle of the mixing-layer) have been used (not shown). For the mean quantities, 10 T_{ft} is sufficient to obtain well-converged profiles. For the RMS velocities, the increase in time-averaging duration from 15 T_{ft} to 20 T_{ft} has a minor impact (less than 5% relative error) on the convergence. Subsequently, the simulation follows the sequence: 1) access to steady state by running the computation for 10 $T_{ft} = 1.25$ ms from the initial conditions presented in Section 2 and 2) convergence of the statistics over a period of 15 $T_{ft} = 1.825$ ms.

Validation of the results

The confidence on the present results has been established by two different procedures and the details of this validation is not presented here as it is not the scope of the report. First, converged results from both solvers have been compared and agree well. Second, simulation results also match some global quantities extracted from key-experiments. The details of those comparisons can found in [68].

Effect of grid resolution and convergence

The objective of this section is to determine the spatial resolution required to obtain grid-independent turbulent statistics for the present benchmark. The grid is progressively refined until the mean and RMS of the transported quantities becomes insensitive to spatial refinement. A set of simulations using increasingly refined meshes have been conducted. The number of cells within the lip height h is set to 5, 10, 30, 100, 250 and 500. In the following, the meshes are called 'hn', where n is the number of cells within the lip. To identify coherent structures in the flow field,

we use the second invariant of the velocity gradient tensor q, defined as [69] $q = \left(|\Omega|^2 - |S|^2\right)/2$, with Ω defined as the the spin tensor and S the strain rate tensor. Fluid particles with a positive q value have more vorticity than strain, which enables one to locate coherent structures in the flow. Figure 2.3 shows instantaneous snapshots of the density field superimposed with a large positive q-isocontour ($q = 10^{12}$ s^{-1}). Similarities can be observed between grid resolutions. The Kelvin-Helmholtz mechanism that sheds eddies at the top corner of the lip is captured even with the coarsest mesh. Large-scale disturbances in the density field can be observed. However, it is clear that the increase in resolution impacts turbulence at the smallest scales. This is coupled with an increase of the multiscale wrinkling of the dense interface. One can observe that grid spacing

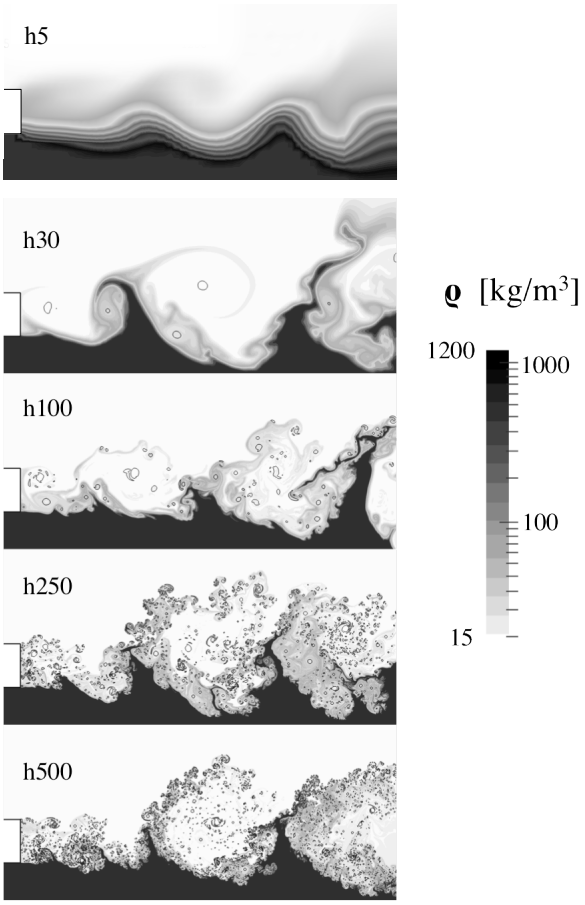

Figure 2.3. Instantaneous snapshots of the density field (log scale) superimposed with a large positive q-isocontour (black isocontour, $q = 10^{12}$ s^{-1}) for increasing mesh resolutions.

has a profound impact on the dynamic of the flow. In the present case, the behavior of the flow in the *h*5 simulation can be characterized as unstable but not turbulent whereas for resolutions finer

than $h30$, the flow is transitioning and turbulent. This shows that grid resolution can modify the physics of the flow. This feature is important and interesting as it cannot necessarily be capture by classical quality criteria such as the Pope criterion. The main mechanism that explain this change in physical behavior is the subsequent numerical filtering. By coarsening the grid, the Reynolds number of the flow is artificially decreased. For a given velocity difference ΔU (imposed for example by the difference in velocities between the two inlet flows in the present case), we can define a maximum resolved velocity gradient as: $\nabla U \approx \Delta U/\Delta x$, Δx being the grid spacing. The main production term in the vorticity equation is proportional to the local velocity gradient. When the grid is coarsen (Δx is increased), this gradient is diminished resulting in a decrease in vorticity production and a delay in the laminar to turbulence transition. In the case of the $h5$ simulation, the grid is so coarse that the flow is no longer turbulent.

One set of metric that can be used to assess grid convergence and the overall quality of the simulation is the convergence of first and second order moments (mean and RMS) of quantities of interest in the flow. For sake of brevity, only the profiles of temperature, axial and transverse velocities located at $x/h = 5$ are presented in Figure 2.4. Very similar trends have been observed

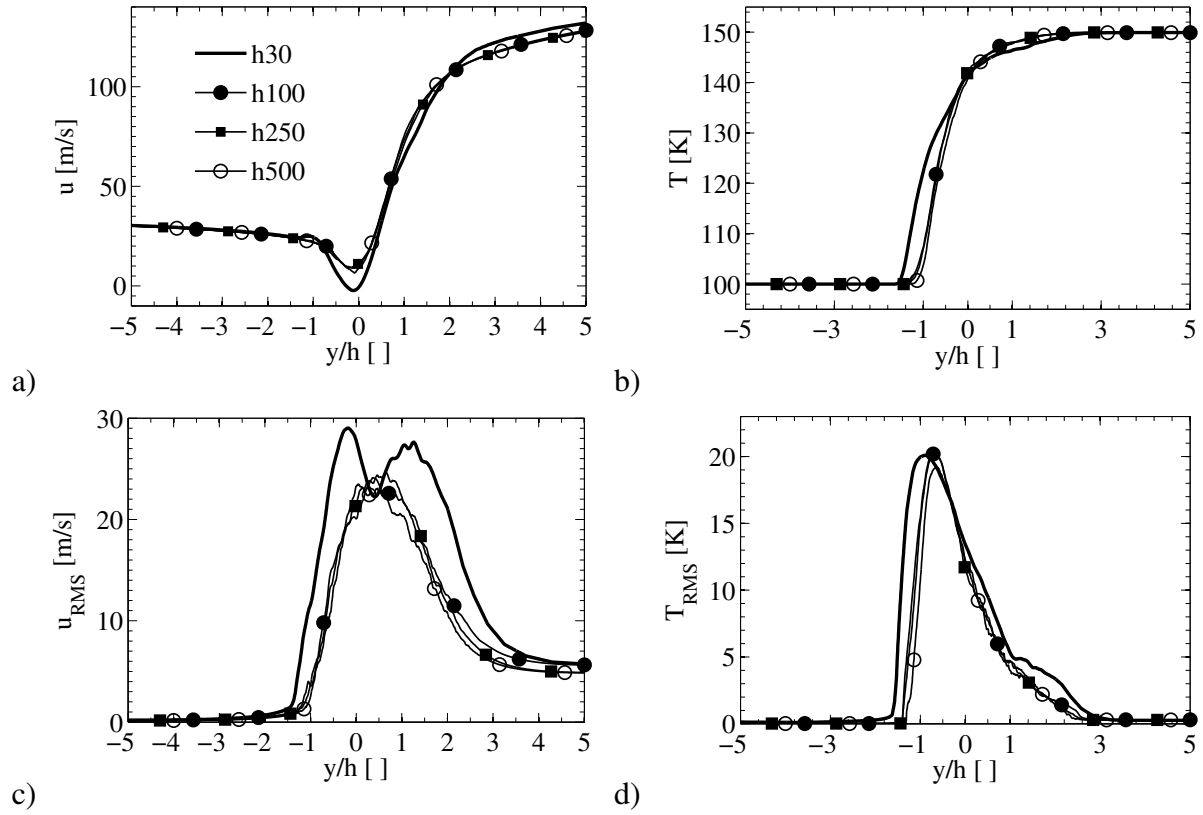

Figure 2.4. Mean and RMS profiles at x/h = 5 and for increasing mesh resolutions. a) mean axial velocity, b) mean temperature, c) RMS axial velocity, d) RMS temperature.

at other locations. While there is a significant impact of mesh resolution between h30 and h100, the time-averaged results are fairly insensitive to mesh resolution beyond h100. One interesting aspect to note is that fluctuations of the axial velocity are stronger in the h30 case than in other more refined cases. The explanation is that as this case is not fully resolved, less small structures are formed which diminishes the turbulence energy dissipation. Hence a coarse simulation can produce more fluctuation than a resolved one as less dissipation is present in the flow.

Another metrics that can be used to assess the quality of a LES simulation is the spectral analysis of certain quantities of interest. Figure 2.5 presents for example the temporal evolution of the vertical component of the velocity (v) and the power density spectra of v^2 at a probe located at ($x/h = 7$ and $y/h = 0$) and for different resolutions. PSD (Power Spectrum Density) analysis

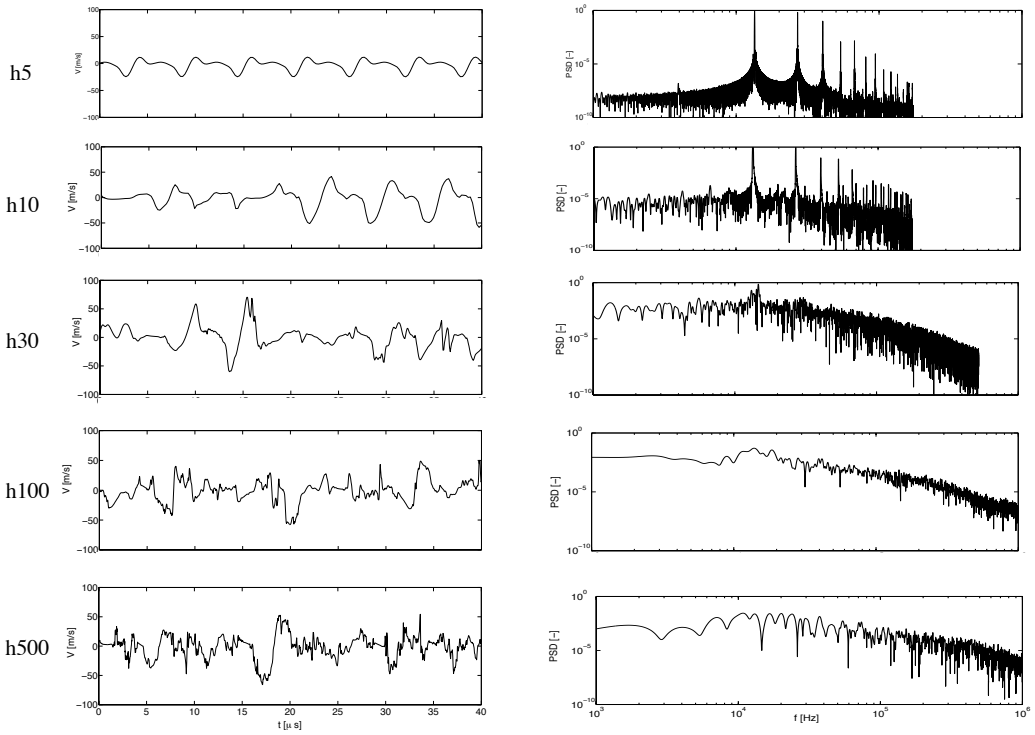

Figure 2.5. Temporal evolution and power spectrum density of the y-component of velocity at a probe located at ($x/h = 7$ and $y/h = 0$)for the different resolutions.

allows to understand more in details the turbulent energy distribution across the resolved scales of the flow. This information is critical to understand how energy transfers from one set of scales to another and detect if certain region of the flow is under-resolved. As previously observed, the coarsest resolution $h5$ posses a deterministic behavior. The flow oscillates without transitioning to

turbulence. A clear mode can be detected in the spectrum at a frequency of about $15kHz$. As the grid is refined, the deterministic behavior of the flow is lost and the stochasticity of turbulence is observed.

If we now collapse all spectra in the same Figure 2.6, some interesting features of the energy transfer can be identify. In the present case, the spectra have two main regions, one with a $-5/3$

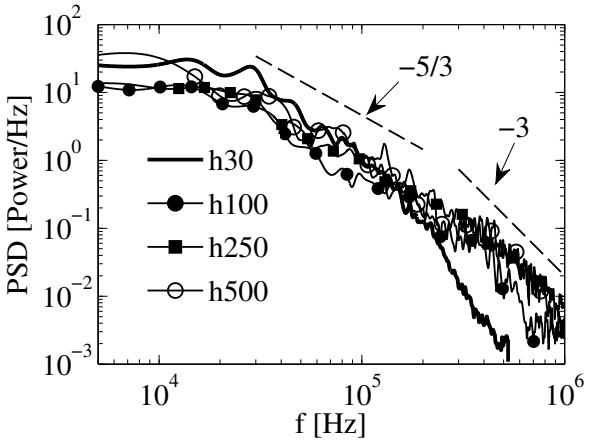

Figure 2.6. Power Spectrum Density of the square of transverse velocity at $(x,y) = (7h,0)$ for increasing mesh resolutions.

slope and one with a -3 slope, as indicated in Fig. 2.6. In 2D turbulence, the $-5/3$ slope indicates a reverse-energy cascade, that transfers energy from the small scales to the large-scales through almalgamation of vortices. The -3 slope indicates a forward-enstrophy cascade, which transfers energy to the dissipative scales of the flow. These two regions have been predicted by theoretical work [70, 71] and observed experimentally [72] for homogeneous 2D turbulent flows. The presence of these two slopes in the Turbulent Kinetic Energy (TKE) spectrum is an indication that 2D turbulence is accurately predicted in the present simulation for resolutions finer than $h30$. However, it also indicates the limitations of the 2D assumption used in the present work because the transfer of turbulent kinetic energy in a 3D turbulent flow is dominated by a different energy cascade: the classical forward-energy cascade with a $-5/3$ slope. The forward-enstrophy cascade is present in the h100, h250 and h500 calculations in the high frequency range ($f > 10^5 Hz$). The h30 mesh is too coarse to capture this range of scales, which implies that dissipation at small scales does not occur. This has been observed in fig 2.4. The reverse-energy cascade thus transfers more energy to the large scales, which explains why the peak and width of the velocity fluctuations presented in Fig. 2.4 are too large. The h100 case is a limit case, where the forward enstrophy cascade starts to appear but the dissipation of energy artificially occurs at scales larger than the physical dissipative scales, due to numerical stabilization. This is consistent with the limited amount of small scale structures observed in Fig. 2.3. Because only a small part of the turbulent kinetic energy is contained in the small scales, the mean and RMS of velocities and scalars are still in good agreement with the h250 and h500 cases, as observed in Fig. 2.4.

A last metric type has been tested for this case. One method used to ensure that local statistic are correct for the "good" reasons is to perform a spatial analysis of the turbulent spectra and measure the impact of grid resolution on this spatial distribution. The idea is to study the development of turbulence along the mixing layer and potentially detect changes in this transition due to grid resolution. In other words we want to make sure we obtain the right statistic for the right reasons. This analysis is based on an line of probes placed in the mixing layer. The line starts at the corner of the splitter plate on the hydrogen side and extends to the outlet (along the path of the center of coherent structures at $y/h = 0.5$) as presented in Fig. 2. A frequency characterization of the most

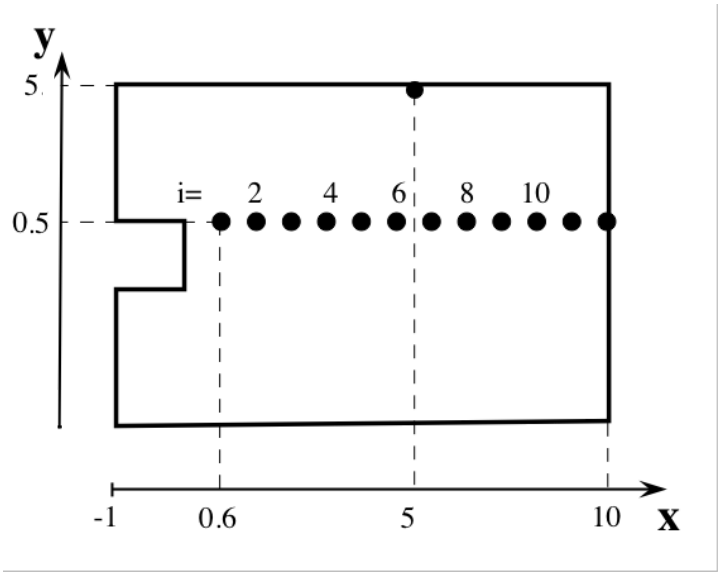

Figure 2.7. Schematic of probe locations for the frequency analysis.

energetic coherent structures in the mixing layer has been performed along the probe line. The spatial evolution of the v^2 power spectrum density is presented in 2.8. One can see in 2.8 that the frequency of the most energetic coherent structures is constant in the current configuration, at a frequency located around $f_1 = 15$ kHz. This value is consistent with experimental observations of air assisted liquid atomization, where the frequency of the passage of a perturbation at the surface of a sheared liquid is shown to be [73, 74]:

$$f \approx U_{conv}/\delta\sqrt{\rho_{H_2}/\rho_{O_2}} \tag{2.8}$$

Where δ is the thickness of the gaseous boundary layer at the inlet. Here, with $\delta \approx h$, we obtain $f \approx 10^4$ Hz. In the present numerical study, the convection velocity has been measured using cross correlation of the vertical velocity signal between adjacent probes of the array presented in 2. Knowing the distance between probes and the time-lag given by the cross correlation method (between two y-velocity signals), a convection velocity has been estimated locally and varies between 20m/s and 40m/s. The footprint of a subharmonic at $f_2 = 30$ kHz is observed around i=6 in

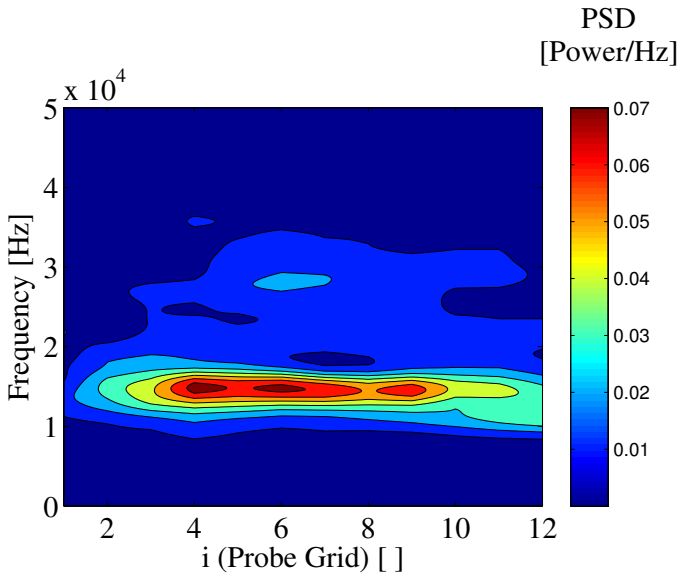

Figure 2.8. Spatial evolution of v^2 power spectrum density (PSD), along the line of probe downstream of the splitter ($y/h = 0.5$ and $0.6 < x/h < 10$ (8 Welch spectrum averaging windows have been used).

2.8. Using the convection speed from Eq. 2.6, the two dominant frequencies f_1 and f_2 corresponds to the wavelengths $\lambda_1 = 5\ h$ and $\lambda_2 = 2.5\ h$. The main wavelength λ_1 corresponds to the distance between two finger-like structures (ejections of LOx into the hydrogen stream), to the distance between two consecutive large-scale negative-vorticity structures and also to the distance between two consecutive intermediate-scale positive-vorticity structure that are shed from the oxygen corner and help the rise of fingers into the hydrogen stream. The secondary wavelength $\lambda_2 = 2.5\ h$ might correspond to the staggering existing between the passage of fingers and the passage of vortical structures, which could generate a subharmonics in the velocity signal. In addition to rotational effects, potential effects might play an important role in creating fluctuations of the vertical velocity, because of the deviation of the hydrogen flow induced by the rise of the LOx finger.

The present section has shown that a systematic analysis of grid convergence using temporal and spectral metrics can lead to a deep understanding of quality requirements in a LES simulation. In particular they can be used to decouple numerical and model errors in an efficient manner as they clearly indicate when grid convergence is reached. In the following, the metrics and methods will be tested on a more complex configuration of a fully three-dimensional jet in a cross flow and the approach will be refined.

This page intentionally left blank.

Chapter 3

Test of the Metrics in a jet-in-cross-flow configuration

Introduction

In the following, the previous set of metrics are tested in a three-dimensional jet in cross-flow experimentally investigated by Su and Mungal. A detailed understanding of turbulent mixing in a Jet-In-Cross-Flow (JICF) is valuable in many practical situations. Applications include plume dispersion, gas turbine combustor cooling, and fuel injection. See Margason et al. [75] for a review. Taking the example of gas turbines, the challenge in their design is to achieve the highest possible performance and reliability in shortening development cycle times. Computational Fluid Dynamics (CFD) calculations help meet this challenge by predicting crucial design parameters in virtual designs. This can allow an early identification of promising options prior to bench testing.

Reynolds-Averaged Navier-Stokes (RANS) has now been used for decades in development cycles because of its moderate computational cost. However, RANS predictions have shown limitations, especially in the "separated-flow" region, in the near-field of the jet nozzle [75]. Recent Direct Numerical Simulation (DNS) calculations [76, 77] have provided insights into the origin of the RANS failure in the near-field. In this region, turbulence production is larger than turbulent dissipation [76]. They have also shown that isotropy and gradient hypotheses used in RANS turbulent closures are not valid [77]. The latter conclusion is also drawn by Ling et al. [78], which was shown by minimizing the error between a RANS computation and a mean experimental scalar field.

Beyond RANS, application of the Large Eddy Simulation (LES) technique provides the formal ability to treat the full range of multidimensional time and length scales in turbulent reacting flows in a computationally feasible manner. The large energetic-scales are resolved directly. The small subgrid-scales are modeled. This allows simulation of the complex multiple-time multiple-length scale coupling between processes in a time-accurate manner. LES is commonly viewed as an engineering tool of the future with the potential to provide useful predictions of combustion at practical conditions and in complex geometries. High-fidelity LES can also serve as a powerful tool for fundamental inquiry into the structure and dynamics of turbulent combustion processes that are dominated by high Reynolds number, geometrically complex flows.

LES has been applied to the JICF configuration by a number of researchers. Most have been

aimed at predicting film-cooling in gas turbines [79, 80, 81, 82, 83, 84]. These studies, as well as the DNS studies mentioned above [76, 77], have improved our understanding of turbulent mixing processes associated with a JICF. Reviews on this topic are available in Karagozian [85] and Mahesh [86].

In general, good qualitative agreement between LES results and time-averaged experimental data can be obtained. Currently, however, no clear methodology is available to distribute grid spacing locally so as to make calculations both affordable and accurate. This "postdictive" nature limits the utility of LES for design. In this paper, we aim at providing a map of turbulent scales so that one can distribute the LES filter width following the spatial evolution of large turbulent scales. We believe the latter strategy will lead to optimal LES meshes, balancing cost and precision.

We consider passive scalar mixing in a single JICF with a angle of 90 degree. In this configuration, detailed measurements of both concentration and velocity are available for validation. The study of Smith and Mungal [87] provides instantaneous scalar fields for a range of velocity ratios. The study of Shan and Dimotakis [88] provides scalar concentration fields in the symmetry and transverse planes for both varying velocity ratios and injection Reynolds number. The study of Su and Mungal [89] provides both instantaneous velocity and concentration measurements in a large number of reference planes and lines. Mean and RMS of scalar concentration and velocities are thus available for validation, as well as Reynolds stresses and turbulent scalar fluxes. These results have been used most recently to validate DNS simulations [76, 77]. Here, we propose to use the extensive experimental database to determine what homogeneous grid spacing enables the LES results to accurately predict experimental results. Then, the validated LES simulation results are used to study the spatial evolution of turbulent scales.

The paper is organized as follows. The target JICF configuration is first described in along with respective operating and boundary conditions. Then, choices in computational domain size and grid resolution are explained. This is followed by an extensive comparison of the LES results with available experimental data is conducted. The main goal of this section is to demonstrate that turbulence is well resolved by the present high-fidelity LES, before analyzing in more details its characteristics. Vortex identification is used to describe qualitatively the structural characteristics of resolved turbulence. We finally concentrate on the analysis of turbulent scales and provide spatial maps that are useful for designing an optimal LES mesh in a JICF.

Description of the geometry, operating, and boundary conditions

Figure 3.1 shows the geometry and the orientation axes of the present JICF configuration. The diameter of the fuel jet is: $d = 4.53$ mm. The grid spacing is constant everywhere in the chamber and in the nozzle. Although computationally expensive, a constant mesh spacing allows a clear understanding of the effect of grid resolution and removes ambiguity related to the distribution of local grid spacing and stretching. In Sec. 3, we provide information that is useful to determine how grid points can be distributed for an optimal LES that balances cost and precision. The spatial extent of the computational domain in the xy plane is chosen to allow comparisons of the LES results to available experimental data. The z spatial extent has been determined through trial-and-

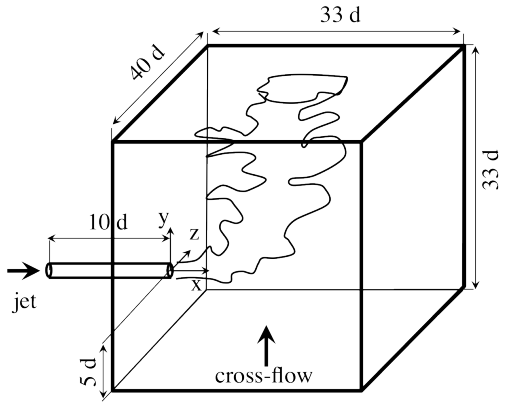

Figure 3.1. Schematic of geometry and orientation axes of the JICF configuration.

error to prevent confinement of the jet and allow the development of the counter-rotating vortex pair (CVP), which drives far-field mixing and jet penetration.

In the fuel nozzle, the bulk velocity u_j is equal to 16.9 m/s. A fully-developed turbulence velocity profile is injected at the nozzle inlet, located $10d$ upstream of the chamber plane. We use the experimental data of a turbulent round jet at $Re = 7\,000$ from Eggels et al. [90]. This turbulent flow profile has already been shown to provide an accurate representation of the turbulence at the exit of the nozzle in the DNS study of Muppidi and Mahesh [76]. At the nozzle inlet, a smooth ramp in time is used with a characteristic non-dimensional time equal to 1 to inject a gas mixture of 10% acetone and 90% nitrogen in volume into air. We use the same gas composition for the jet fluid as in the experiment, which induces a small density ratio of 1.1 between the jet and the cross-flow [89]. In the DNS of Muppidi and Mahesh [76] a passive scalar is transported and the density is identical in the jet and cross-flow. Jet trajectories were rescaled by an effective momentum-flux ratio to compensate for this discrepancy in injection density. Here, the density ratio effects are captured and we do not need to add a correction factor in the results.

At the channel inlet, we use an analytic approximation of the Blasius profile [91] for the v-velocity (aligned with the y axis) and we set the u-velocity to zero (neglecting the wall-normal velocity). This is due to the $u = 0$ boundary condition used at $x/d = 33$ that imposes a relaxation of the u-velocity from a constant non-zero value in the free-stream (according to the solution of the Blasius equations) to a zero value at the wall. This is not a strong assumption since the magnitude of the u-velocity is very small in comparison to the v-velocity ($u_\infty = 6\ 10^{-3} v_\infty$) and the actual

u-velocity profile establishes itself in the channel before reaching the jet nozzle.

$$
\begin{aligned}
v &= v_\infty \tanh(78\eta/19 - (219/5)\operatorname{atan}(8\eta/93)) \text{ where} \\
&\quad \eta = 5x/\delta_c \\
&\quad \delta_c = 1.025\, d \\
&\quad v_\infty = u_j/5.7
\end{aligned}
\tag{3.1}
$$

The thickness of the laminar boundary layer δ_c is determined from the PIV measurements of Su and Mungal [89].

For the outflow boundary conditions, pressure is set to $P = 1.013\ 10^5$ Pa, and velocity and scalars are extrapolated. Immediately upstream of the outlet boundary condition, a sponge-layer starts at $y = 28d$, with a transition thickness of $0.5\ d$. The transport coefficients are multiplied by a factor of 10 in this sponge-layer, which damps hydrodynamic structures before they cross the outlet boundary condition, which prevents backflow and contamination of the upstream flow field.

Determination of domain size and grid resolution

In this section, the method to determine the domain size and grid resolution is described. First, the filter size that ensures grid-independent statistics in the near-field is determined. A small domain limited to the near-field ($x < 15d$, $y \leq 5d$) is used and a parametric study on the filter width size has been conducted. The mesh spacing has been progressively refined with an increasing number of cells 'n' in the reference length scale d (jet diameter). Four different levels of resolution have been considered: $n = 5$, $n = 10$, $n = 15$, $n = 20$, which corresponds to grids containing 0.6-million, 3-million, 8.5-million and 18-million cells, respectively. Times steps have been adjusted to the spatial resolution so that a unity convective CFL number is maintained. This ensures accurate temporal discretization for all simulations. The jet nozzle is included in the simulation using the immersed boundary technique which allows the use of the same spatial resolution as in the chamber and removes meshing difficulties.

All computations have been initialized using the same initial solution. The jet nozzle flow is initially at rest, and the inlet velocity profile of the cross-flow air is extruded in the channel. Acetone mass fraction and jet velocity are slowly ramped-up and the jet enters the cross-flow. After this transient, the turbulent statistics have been converged.

Figure 3.2 shows the mean and RMS fields of concentration in a transverse cut at y/d=2.5 (near-field region, after the jet turbulent breakdown). This plane is used to monitor mesh convergence, since it contains the finger-print of resolved coherent structures and developing turbulence. Farther downstream, turbulence structures grow and the deviations between mesh resolutions diminish. For the two highest resolutions (d15 and d20), a classical kidney-shape structures is observed on the mean and RMS of the concentration field. At lower resolution, the mean and RMS of concentration at impacted by grid resolution and this resolution is too coarse to predict correctly turbulent mixing in the near-field. The other statistical results (mean and RMS of velocity and turbulent fluxes) also

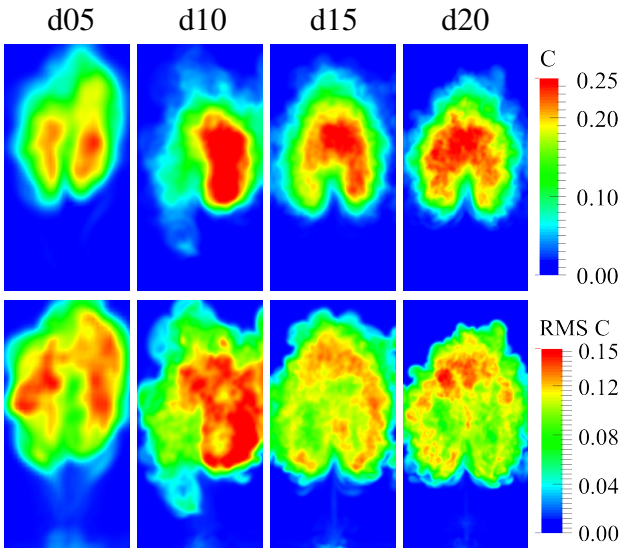

Figure 3.2. Mean and RMS concentration in the transverse plane y/d=2.5 for increasing mesh resolution.

indicated the same trend (not shown). The statistical results are not significantly different between $dx = d/15$ and $dx = d/20$, which proves mesh convergence for LES filter width of $dx \leq d/15$.

One important aspect also observed in the previous Chapter is the nonlinear impact of grid resolution on fluid dynamics. This is illustrated in Fig. 3.3. The artificial filtering of the velocity gradients at low at low resolution (d05) results in a decrease of the effective Reynolds number. This yields the generation of two strong vortices with rotational axis aligned with the jet. Those structures have a major impact on the overall dynamics of the jet which exhibits a asymmetric behavior. The asymmetry results from the interaction between one of the counter-rotating vortex with a span-wise vortex developing close to the wall. This provides a hint on the non-symmetrical aspect of the concentration field for the d10 case in Figure 3.2.

Then, it is necessary to ensure that the JICF is free from the influence of the walls of the computational domain. A coarse simulation has first been conducted with a mesh spacing $dx = d/5$ in an extended domain D_{large}. The dimensions of this domain are $(\Delta x/d, \Delta y/d, \Delta z/d) = (60, 46, 40)$. Statistics have been converged up to $y/d = 25$ which is approximately 10 diameters downstream of the end of the interrogation window in Su and Mungal [89]. The extent of the domain has then been decreased using a visual margin of $3d$ around the large CVP at $y/d = 25$, as shown on Fig. 3.4a).

This new domain D have the following dimensions: $(\Delta x/d, \Delta y/d, \Delta z/d) = (33, 33, 40)$. The solution from the extended domain D_{large} has been interpolated to the smaller domain D and the statistics have been compared. Figure 3.4b) shows the mean concentration in a 1D transverse cut through the jet. The cut is located between $z/d = -10$ and $z/d = 10$ at $x/d = 10$ and $y/d = 25$. The

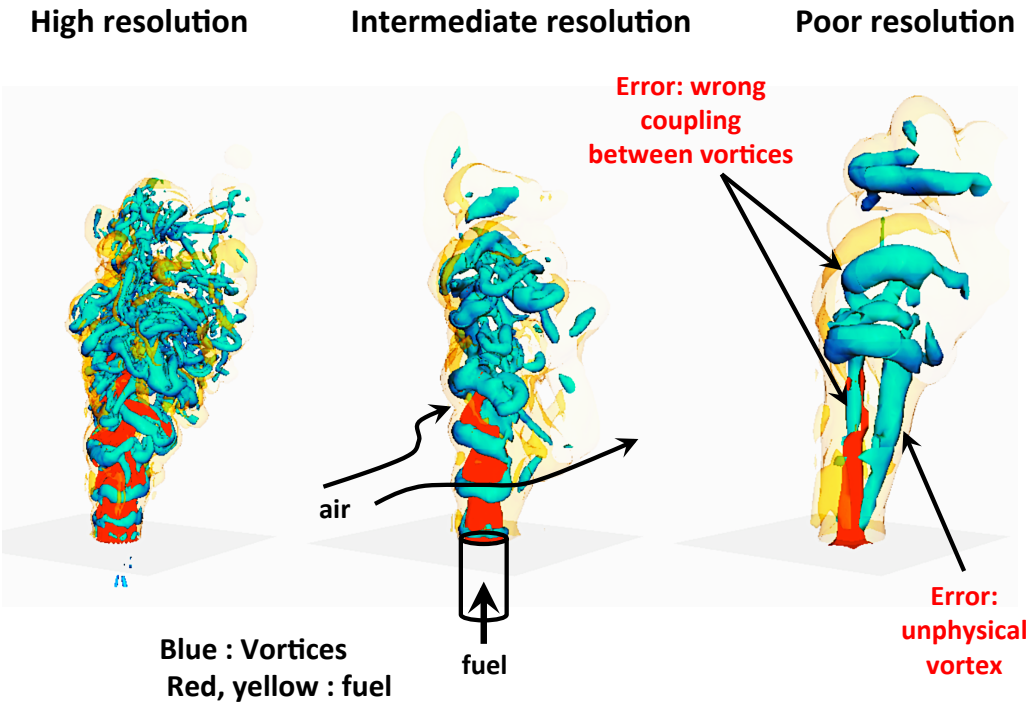

Figure 3.3. Nonlinear effect of gird resolution on the jet dynamics.

time-averaging period is equal to 300 d/u_j for both cases. Before recording statistics in the domain D, a flushing period of 130 d/u_j has been used. The mean concentration field is qualitatively similar in both cases and the minor deviations are only due to the finite averaging time used to estimate the mean of a turbulent signal. This shows that even in the far-field, the jet is not confined by the walls of the computational domain.

In summary, it has been determined that turbulent statistics (mean and RMS of velocities and scalars) are independent of the LES filter width with a constant grid spacing $dx \leq d/15$ and that a domain size of $(\Delta x, \Delta y, \Delta z) >= (33, 33, 40)$ do not induce confinement of the jet in the region upstream of $y/d = 25$. In the following, a domain size of $(\Delta x, \Delta y, \Delta z) = (33, 33, 40)$ and a grid resolution of $dx = d/15$ is used, which enables to obtain grid-independent results and well-converged statistics at an acceptable computational cost.

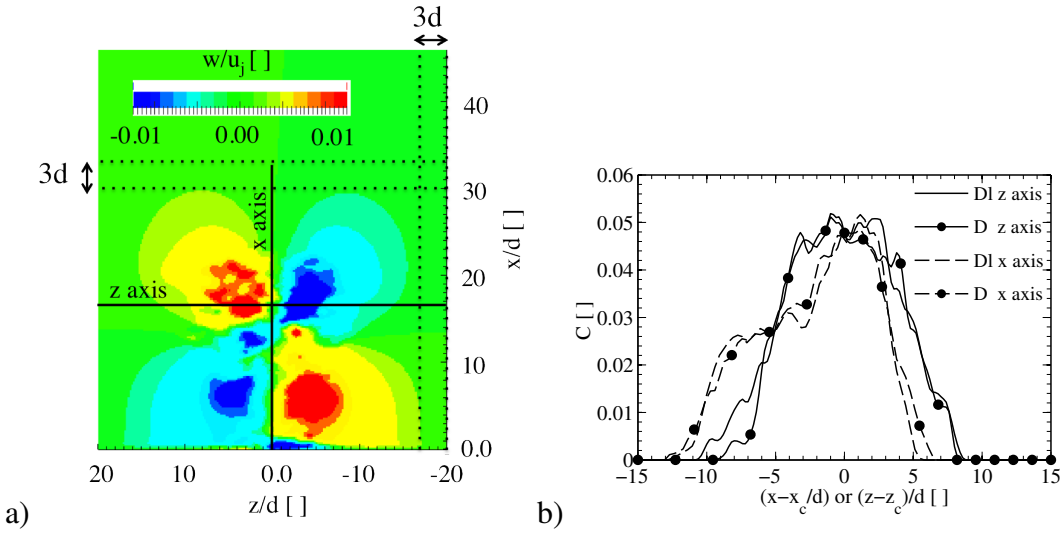

Figure 3.4. a) Mean spanwise velocity field at $y/d = 25$ for a large domain Dl using a coarse LES filter width of $dx = d/5$. b) Mean concentration along 1D cuts through the jet. The cut locations are indicated in a).

Validation with experimental results

In this section, an extensive comparison of the LES results with available experimental data is conducted. The main goal of this section is to demonstrate that turbulence is well resolved by the present high-fidelity LES, before analyzing in more details its characteristics in the next sections.

2D planes

Figure 3.5 shows a comparison between instantaneous concentration fields obtained in the LES and in the experiment. In Fig. 3.5a) the flow field is observed in the jet centerplane ($z/d = 0$). In Fig. 3.5b)-d) the flow field is observed in multiple off-center planes: (b) $z = 1.25$ d, (c) $z = 2.56$ d and (d) $z = 3.82$ d. Figure 3.5a), shows that in the first few diameters near the jet nozzle exit, disturbances in the jet shear-layer are observed in both the experiments and the LES. These initial disturbances are spanwise rollers [79] developing due to the Kelvin-Helmholtz instability induced by the velocity gradient between the jet and the cross-flow. A more detailed description of these structures is given in Sec. 3. In the immediate wake of the jet, pockets of jet fluids are separated from the jet core. This is closely related to the nascent CVP in the wake of the jet, which transports jet fluid from the edges of the jet back into the centerplane. More details on this phenomenon is given in Sec. 3. Further downstream, the jet bends due to pressure forces created by the impact of the cross-flow on the jet. Disturbances at larger scales are visible on the outer edge of the jet in

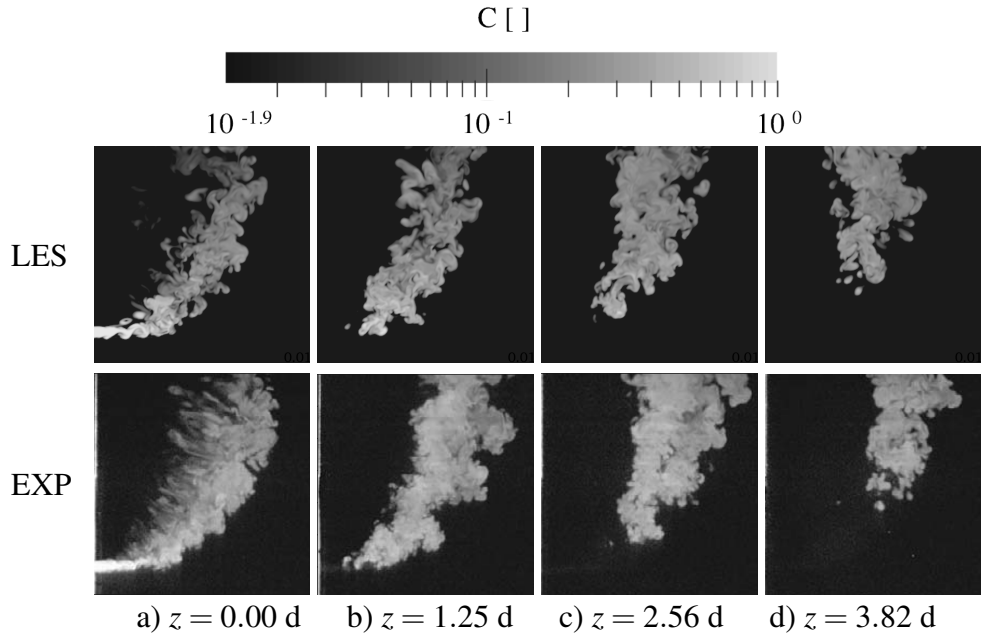

Figure 3.5. Instantaneous scalar fields for increasing distance from the centerplane.

both the LES and the experiment. This is related to the engulfment of air into the jet, and is one of the mechanisms which enhance entrainment in a JICF, when compared to a regular turbulent round jet [79, 85]. At the inner edge of the jet (closer to the wall), threads of jet fluid are observed. These elongated structures have been observed in previous numerical studies [77], but their origin has not been described. The physical mechanism by which they form is explained in Sec. 3.

In the planes further away from the centerplane shown in Figs. 3.5b)-d), the formation of isolated pockets is more frequent. These pockets contain well-mixed fluid, which is qualitatively similar to what is described as 'cliff' and 'plateau' in Shan and Dimotakis [88]. The transport of the jet fluid in the spanwise direction appears well predicted in the LES, as the bottom location where jet fluid appears first in the offcenter planes is similar to the experimental measurements.

In summary, the essential qualitative features of the JICF appears well predicted in the LES results. In Sec. 3, we validate our LES results using statistical results representing turbulent mixing.

1D cuts

In this section, a quantitative comparison of the LES and experimental results for first order statistics (mean of C and V) and second order statistics (RMS of concentration and velocity, Reynolds stress tensor, and turbulent fluxes ($u_i'C'$)) is conducted. The location of the 1D cuts is

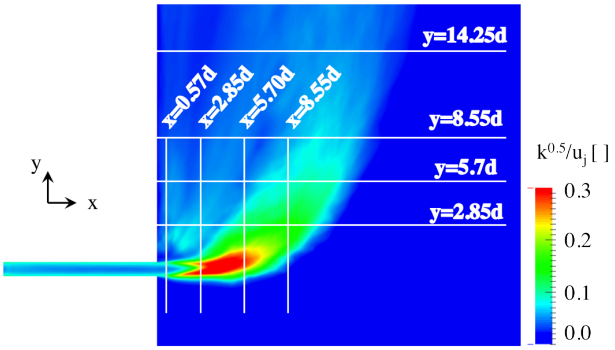

Figure 3.6. Location of the 1D cuts used for validation of LES with experimental results. The centerplane (z/d=0) is colored by the square root of the turbulent kinetic energy $k^{0.5}$.

shown in Fig. 3.6. This figure shows the square root of Turbulent Kinetic Energy (TKE) $k^{0.5}$ field (characteristic turbulent velocity) in the centerplane (z=0). The TKE k is defined as:

$$k = \overline{(u'^2 + v'^2 + w'^2)}/2 \tag{3.2}$$

with primes denoting fluctuations of resolved quantities with respect to the mean, and the over line denotes a long-time average. The first four cuts between $x = 0.57\ d$ and $x = 8.55\ d$ are located near the jet nozzle exit, and allows for monitoring of the evolution of turbulent mixing statistics as the jet bends into the cross-flow. The top four cuts between $y = 2.85\ d$ and $y = 14.25\ d$ probe the flow downstream of the turbulent breakdown, as the 1D lines are located downstream of the region of maximum velocity fluctuations. These latter cuts allows for monitoring of how turbulent mixing statistics evolve towards a pure wake flow in the far-field. Muppidi and Mahesh [76] have validated their DNS with the cuts located in the near-field of the jet, limiting the comparison to the first three cuts at $x = 0.57\ d$, $x = 2.85\ d$ and $x = 5.7\ d$. Note that they focused their effort on the near-field region, using only 11 million cells, whereas 190 million cells are equally distributed in the whole domain in the present high-fidelity LES. In the present study, the numerical results are also validated against experimental data in the the far-field, which is important for assessing the prediction accuracy of turbulent mixing in the wake of the jet.

To ensure sufficient statistical convergence of the results, ensemble averages are performed over 20 flow-through times T_{ft}, sampling the flow every iteration. The flow-through time is estimated using a length scale of $L = 20\ d$ and the fuel bulk velocity $U = u_j$. Thus, a flow-through time is equal to $T_{ft} = L/U = 20d/u_j$. Time-averaging is thus conducted over more than 400 non-dimensional time units ($= d/u_j$), which corresponds to a physical time of 100 ms. Because of the large number of cells (190 million) and the long time-integration period, the computational cost associated with the present simulation results is consequent and 2 million CPU hours were required on a machine composed of AMD Opteron Processors (2.2 GHz).

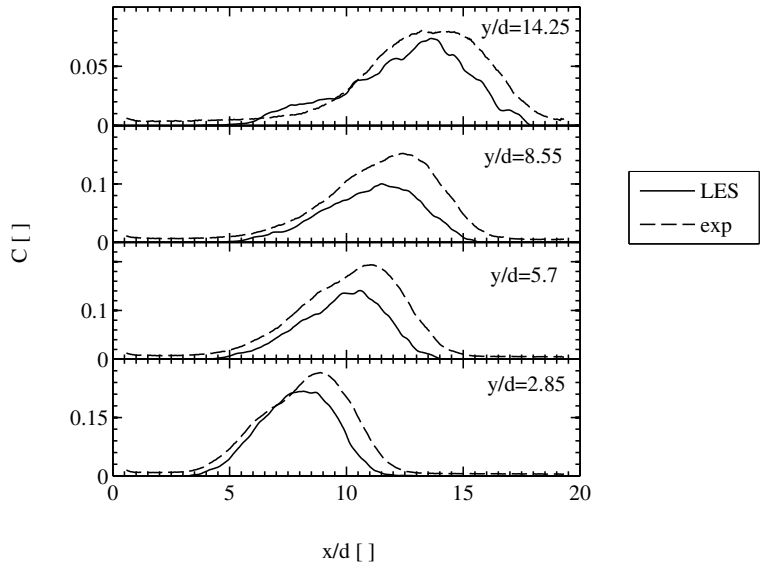

(a)

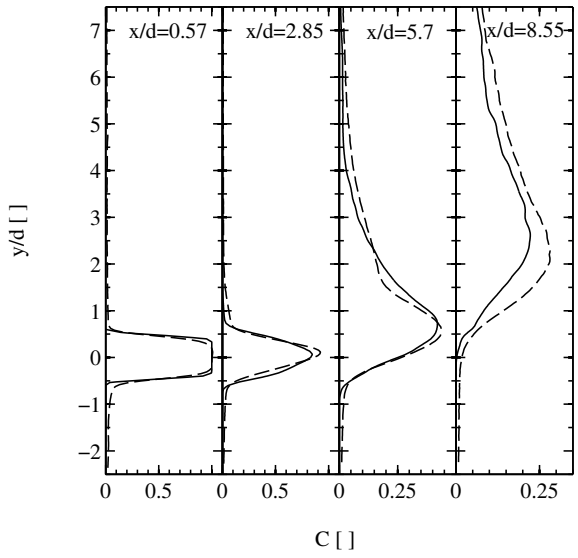

(b)

Figure 3.7. Averaged scalar profiles in the jet centerplane for the simulation and the experiment. (a) The profiles for $y = 2.85\ d$, $5.7d$, $8.55\ d$ and $14.25\ d$, and (b) the profiles for $x = 0.57\ d$, $2.85\ d$, $5.7\ d$.

Figure 3.7 shows the time-averaged concentration profiles in the jet center-plane. At $x = 0.57\ d$, the jet potential core is still present and a flat profile of concentration is observed. At $x = 2.85\ d$, which corresponds to the end of the jet core (see Fig. 3.6), the concentration profile starts to spread and the maximum concentration decreases. It is equal to $C = 0.83$ in the LES and $C = 0.92$ in the experiments (10% relative deviation), while the location of the peak concentration is similar ($y = 0.11\ d$). A tail is also observed on this profile, although it is not as strong in the LES as in the experiment. At $x = 5.7\ d$, which is located near the end of turbulent breakdown, a good agreement is obtained between LES and experiment, with a maximum concentration equal to $C \approx 0.4$ (with a 5% relative error between LES and exp), located at $y \approx 0.7\ d$. At $x = 8.55\ d$, downstream of the turbulent breakdown region, even though the maximum concentration in the LES simulation is comparable to the one from the experiment ($C \approx 0.25$, with a relative deviation of 15%), it appears that the jet is more deviated by the cross-flow in the LES than in the experiment, as the concentration profiles in the LES are shifted upward. The same observation can be made with the far-field cuts presented in Fig. 3.7a). Even though the shape of the concentration profiles is comparable between LES and experiment, as well as their maximum concentration value, in the LES, the jet penetrates less into the cross-flow than in the experiment. The reason for this discrepancy is not clear. It might come from experimental uncertainties associated with the acetone concentration of the jet fluid. Although it is mentioned in Su and Mungal [89] that the jet fluid contains 10 % acetone is volume, a small change in acetone content could have deep consequences on the actual penetration of the jet, by changing the momentum-flux ratio. Because of the large cost of the present high-fidelity LES, it was not possible to make a parametric study on the acetone concentration, and we preferred to maintain the same level of acetone concentration as indicated in Su and Mungal [89]. The LES subgrid-scale model might also be responsible for some of the deviations between LES and experiments, although in the far-field, SGS modeling is negligible in front of molecular viscosity ($\mu_t \leq \mu_l/10$ for $s \geq 17\ d$ along the jet center streamline), which shows that the high-fidelity simulation results presented herein do not heavily rely on the SGS model. Also note that in Su and Mungal [89], the raw data is actually filtered using approximately 10 neighbouring pixels (probably to filter experimental noise), which corresponds to a filter width of approximately 0.15 d. Some more filtering effects come from the finite-thickness of the laser sheet used in the experiments, which can reach 0.11 d [89]. This might also explain some of the discrepancies observed when comparing the simulation results with experiments.

Figure 3.8 shows the time-averaged velocity profiles in the jet center-plane. Figure 3.8b) shows that the average velocity field is very well predicted in the first two cuts at $x = 0.55\ d$ and $x = 2.85\ d$. At $x = 0.55\ d$, the velocity profile is very similar to the injection profile in the nozzle and the influence of the cross-flow is not observable, except that a tail is present in the wake of the jet. This corresponds to the perturbed boundary layer in the wake of the jet. At $x = 2.85\ d$, the profile is specific to the JICF configuration. A mean velocity peak is located near the jet axis ($y \approx 0\ d$) and a tail is observed on the positive-y side of the profile [89]. This tail is the finger-print of the wake downstream of the jet, which is thus accurately predicted by the LES. Further downstream, at $x = 5.7\ d$ and $x = 8.55\ d$, some deviations can be observed but overall a good agreement is still observed. Note that similarly to the concentration profiles, the velocity profiles show a jet that penetrate less deeply into the cross-flow in the LES. In the far-field, Fig. 3.8a) shows that even though larger deviations are observed between LES and experiments, the essential flow features are well predicted by the LES. A double-peak structure is observed on the mean velocity field

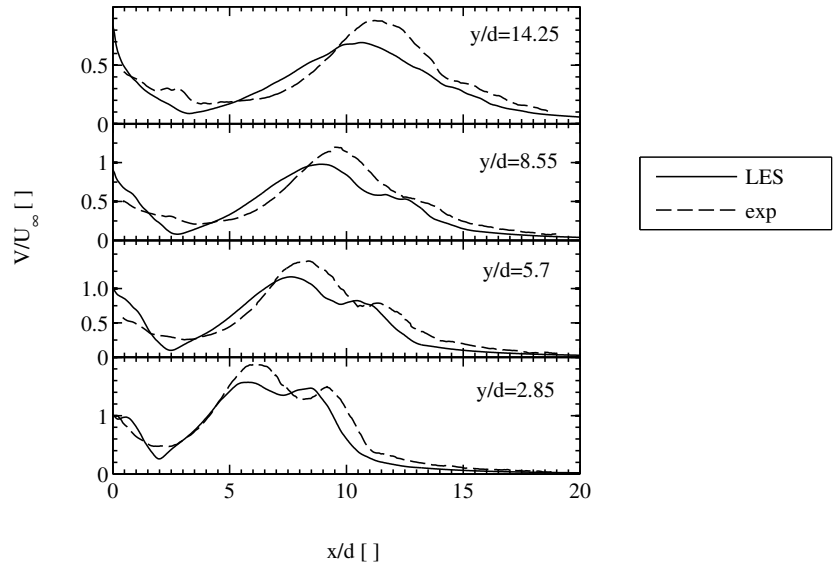

(a)

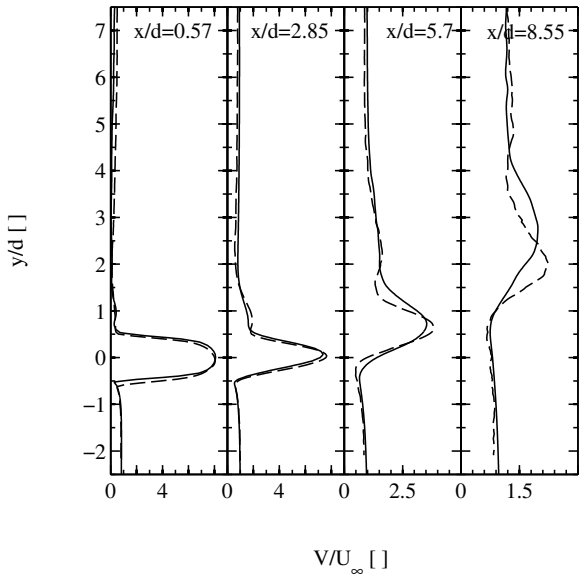

(b)

Figure 3.8. Averaged velocity magnitude profiles in the jet centerplane for the simulation and the experiment. (a) The profiles for $y = 2.85\ d$, $5.7d$, $8.55\ d$ and $14.25\ d$, and (b) the profiles for $x = 0.57\ d$, $2.85\ d$, $5.7\ d$.

and the peak which is located the farthest away from the jet nozzle slowly disappears as the jet disintegrate. The amplitude of this secondary peak is well predicted by the LES, in spite of a lesser penetration in the cross-flow. The magnitude of the main velocity peak appears underpredicted in the LES (relative error inferior to 20% in all far-field cuts), and the profiles spread more. This main peak of velocity correspond to the velocity induced by the counter-rotating vortex pair in the wake of the jet.

Although the agreement between LES and experimental results is not perfect at all locations, the time-averaged fields appear overall well predicted by the LES, and important trends as well as correct levels of concentration and velocity are captured. Higher-order statistics are now analyzed.

Figure 3.9b) shows the scalar variance profiles. At $x = 0.57\ d$, the scalar fluctuation levels are much more important in the LES than in the experiment. In the DNS of Muppidi and Mahesh [77], the simulation results also show much higher fluctuation levels than in the experiment. The maximum value of scalar fluctuation predicted by the latter simulation is $C'C' = 0.1$, which has the same order of magnitude as in our LES results. Further downstream, the deviations decrease although they are still present. In Muppidi and Mahesh [77], they investigate whether the spatial filtering induced by the finite-thickness of the laser sheet and the spatial resolution of the camera used in Su and Mungal [89] can impact measured fluctuation levels. Although fluctuation levels are shown to diminish with increasing filtering, the levels obtained in the experiments are still much lower than the filtered DNS results and no definitive explanation is available for this discrepancy. Because our simulation results shows similar fluctuation levels as in the DNS of Muppidi and Mahesh [77], experimental resolution in the near-field might not be high enough to provide the right levels of scalar variance. In the far-field cuts shown in Fig. 3.9a), a qualitatively similar trend is observed. A double-peak structure of scalar fluctuation is observed between the LES and the experiment. The peak of fluctuation at the outer edge of the jet is stronger than the one located at the inner edge. The scalar variance at the inner edge corresponds to fluctuations occuring within the counter-rotating vortex pair in the wake of the jet, while the scalar variance at the outer edge correspond to the interface between the jet and the cross-flow of air.

Figure 3.10 shows the time-averaged horizontal turbulent flux of concentration $u'C'$. Clear peaks of positive correlation between concentration and horizontal velocity is present at the jet edges. The turbulent structures developing in the shear-layer induce convective transport of concentration. Similarly to the scalar variance profiles shown in Fig. 3.9, experimental measurements in the near-field show much lower values of fluctuations than in the LES results. When comparing with the simulation of Muppidi and Mahesh [76], a qualitatively similar result is obtained, although fluctuation levels are larger in our case than in the DNS (approximately a factor of 2). In the very near-field, it seems that the LES result is not resolved enough to really capture the small scale-turbulence developing within the shear-layers of the jet. However, further downstream, when shear layers have merged and larger-scale turbulence develops, a good agreement is observed between LES, DNS and experiments. The agreement between LES and experimental profiles at $x/d = 8.55$ is excellent. The far-field cuts shown in Fig. 3.10a) shows a very good agreement between LES and experiment, in terms of maximum values of correlation, and shapes of the profiles. Note that largest turbulent fluxes of concentration are located at the outer edge of the jet, as indicated by the large peaks of $u'C'$, which is related to engulfment observed in Fig. 3.5a).

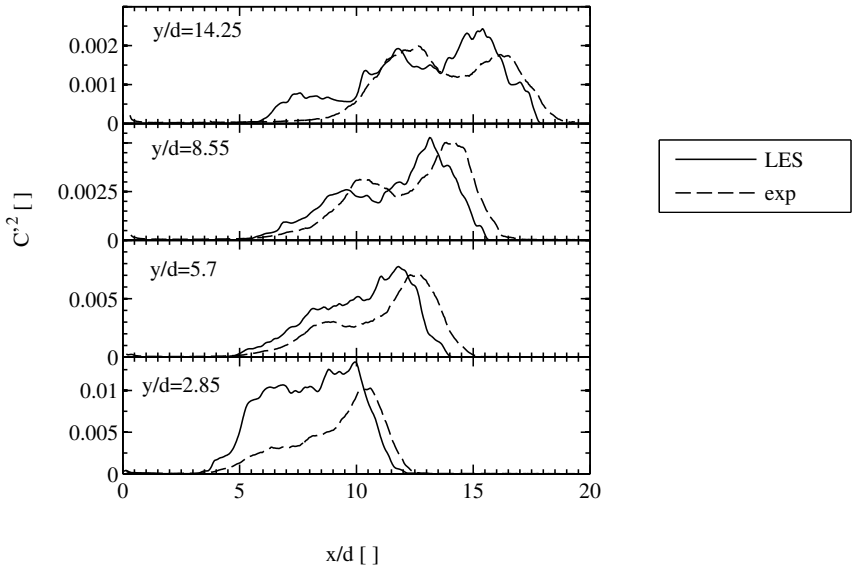

(a)

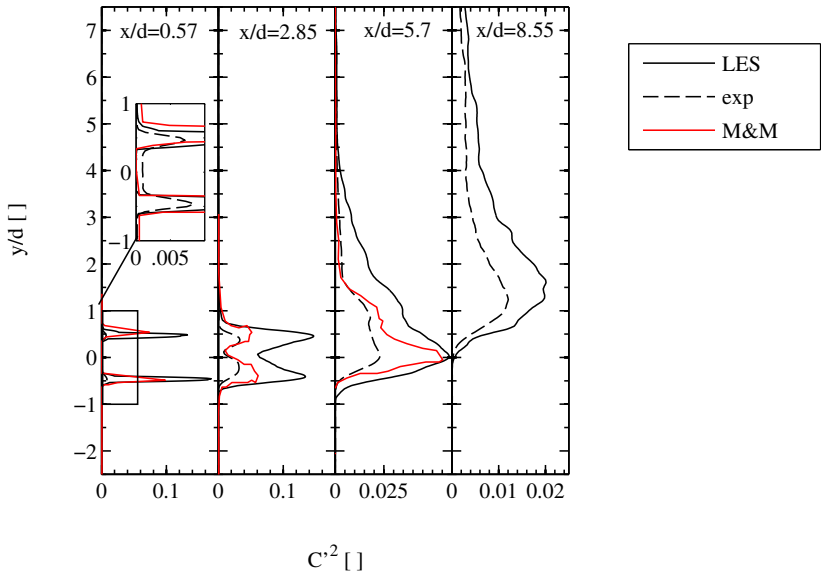

(b)

Figure 3.9. Scalar variance profiles in the jet centerplane for the simulation and the experiment. (a) The profiles for $y = 2.85\ d$, $5.7d$, $8.55\ d$ and $14.25\ d$, and (b) the profiles for $x = 0.57\ d$, $2.85\ d$, $5.7\ d$.

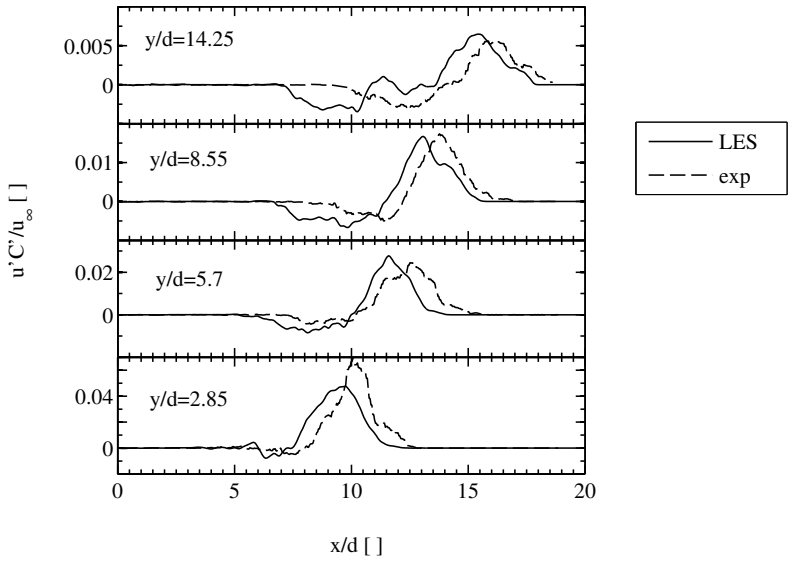

(a)

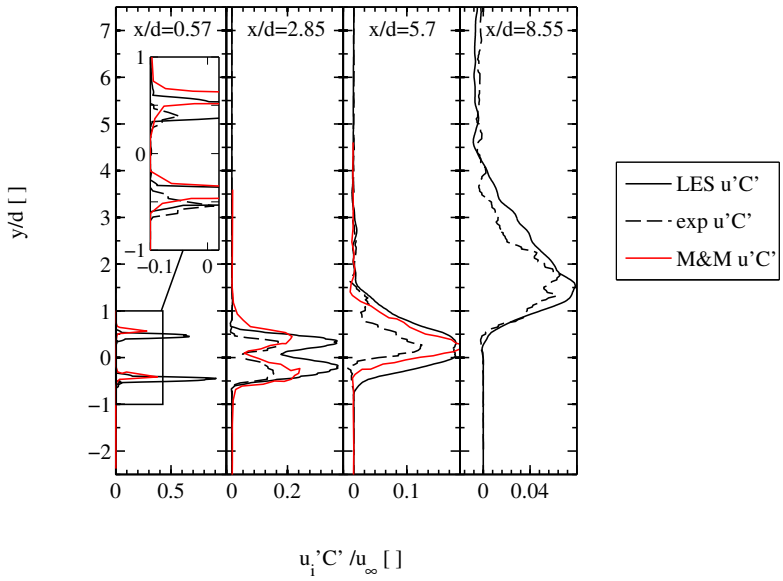

(b)

Figure 3.10. Turbulent scalar flux profiles $u'C'$ in the jet centerplane for the simulation and the experiment. (a) The profiles for $y = 2.85\ d$, $5.7d$, $8.55\ d$ and $14.25\ d$, and (b) the profiles for $x = 0.57\ d$, $2.85\ d$, $5.7\ d$.

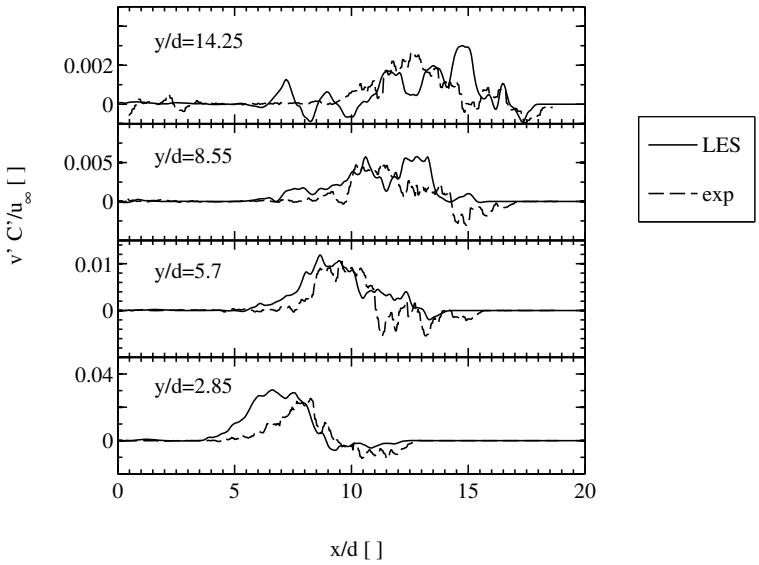

(a)

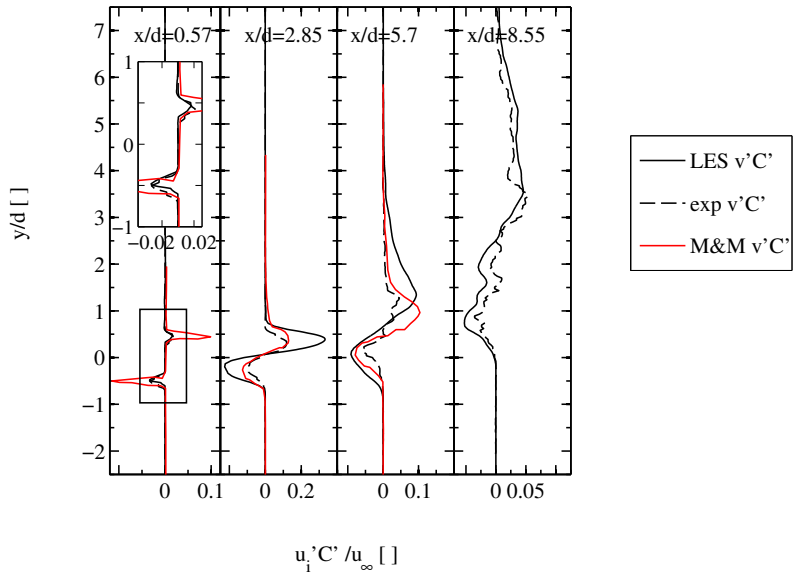

(b)

Figure 3.11. Turbulent scalar flux profiles $v'C'$ in the jet centerplane for the simulation and the experiment. (a) The profiles for $y = 2.85\ d$, $5.7d$, $8.55\ d$ and $14.25\ d$, and (b) the profiles for $x = 0.57\ d$, $2.85\ d$, $5.7\ d$.

Figure 3.11b) shows the time-averaged vertical turbulent flux of concentration $v'C'$. At $x = 0.57\ d$, good agreement is observed between LES and experiment. However, this quantitative agreement appears fortunate since it is the combination of smaller $v'v'$ and greater $C'C'$ in the simulation. The qualitative growth in magnitude and spatial extent of the vertical turbulent flux of concentration are well predicted between $x = 2.85\ d$ and $x = 8.55\ d$. At $x = 5.7\ d$, similar fluctuation levels are observed in both DNS and LES. The profiles of Fig. 3.11a) show that a good agreement between LES and experiment is obtained in the far-field.

Figure 3.12 shows the time-averaged Reynolds stress tensor in the jet center-plane. At $x = 0.57\ d$, the fluctuations profile is very similar to the injection profile in the nozzle and the influence of the cross-flow is not observable. Two peaks of RMS velocity are observed in the jet shear-layer where turbulent structures form. Cross-correlations of velocity alternate in sign, as classically observed in turbulent pipe flows. At $x = 2.85\ d$, horizontal velocity fluctuations are enhanced on the wind-side of the jet whereas the fluctuations on the lee-side of the jet are similar to $x = 0.57\ d$. This clearly indicates mixing enhancement due to the presence of the cross-flow. It is shown later (see Sec. 3) that on the wind-side of the jet, "V-shape" vortices form and interact with ring-vortices, which enhances turbulent mixing. At $x = 5.7\ d$, velocity fluctuations are accurately predicted near the end of the turbulent breakdown.

Overall, good predictions are also obtained for the high order moments of turbulent statistics. This indicates that both mean and RMS quantities are accurately predicted by the present high-fidelity LES. This validated simulation can now provide information which is complementary to the experimental database.

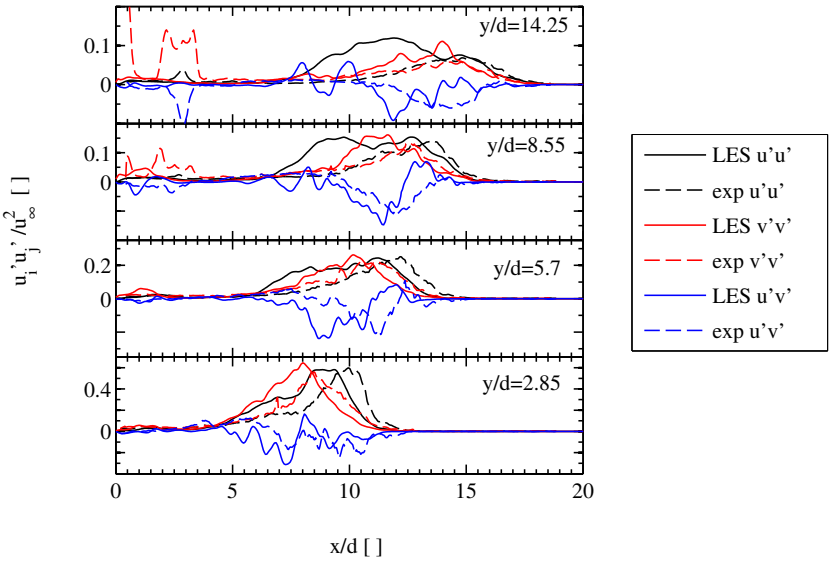

(a)

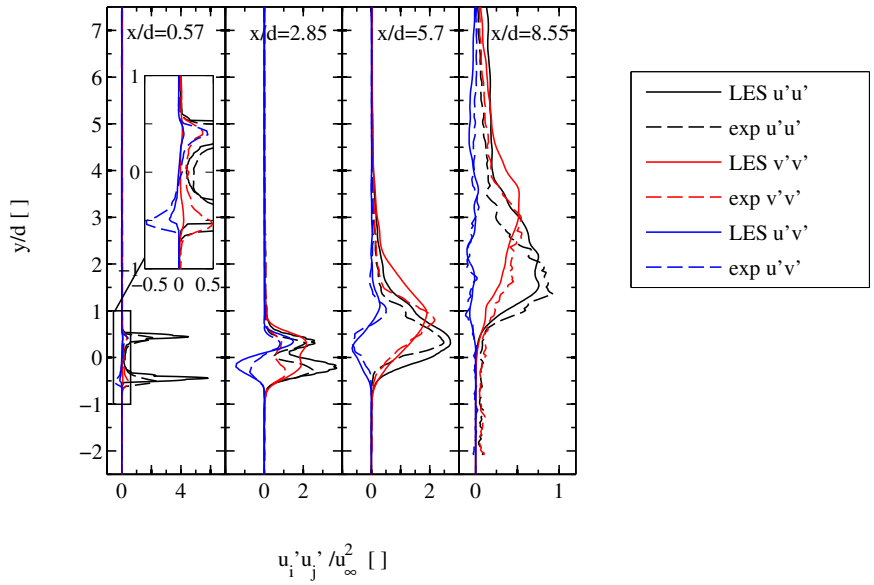

(b)

Figure 3.12. Turbulent stress profiles in the jet centerplane for the simulation and the experiment. (a) The profiles for $y = 2.85\ d$, $5.7d$, $8.55\ d$ and $14.25\ d$, and (b) the profiles for $x = 0.57\ d$, $2.85\ d$, $5.7\ d$.

Qualitative observations of coherent structures

The LES results have been extensively validated against experimental results in Sec. 3. These validated results are now used to propose a detailed description of the main classes of coherent structures in the flow. This enables a better understanding of the complex instantaneous 3D flow dynamics.

Experimental and numerical studies have enabled the observation of vortical structures in a JICF, see [92, 93, 94], amongst many others. Depending on the characteristic non-dimensional numbers of a particular JICF (Reynolds number, velocity ratio, density ratio), certain classes of turbulent structures dominate others. Thus the main turbulent structures in the present configuration needs to be identified. The 'Q-criterion' vortex identification technique [69] is applied to the LES instantaneous flow fields. Q is the second invariant of the velocity gradient tensor Q. Neglecting the velocity divergence in the present low-Mach number flow, it reads:

$$Q = -1/2 \left(\left(\frac{\partial u}{\partial x}\right)^2 + \left(\frac{\partial v}{\partial y}\right)^2 + \left(\frac{\partial w}{\partial z}\right)^2 + 2\frac{\partial u}{\partial y}\frac{\partial v}{\partial x} + 2\frac{\partial u}{\partial z}\frac{\partial w}{\partial x} + 2\frac{\partial v}{\partial z}\frac{\partial w}{\partial y} \right) / (u_j^2/d^2) \quad (3.3)$$

By taking a positive isosurface of Q, one identifies flow region containing more vorticity than strain, which is characteristic of coherent structures. Figure 3.13a) shows an instantaneous 3D visualizations of the flow field using the Q-criterion technique. The $Q = 0.02$ isocontour is represented in blue, and two isocontours of concentration ($C = 0.25$ in red and $C = 0.01$ in yellow) locates the jet. A wide range of turbulent scales is captured by the present high-fidelity simulation, especially along the jet trajectory. At the wall, coherent structure also develop in the boundary layer downstream of the jet nozzle. This shows that even though the boundary layer is initially laminar upstream of the jet, vortical structures develop in the disturbed boundary layer downstream of the jet. Fig. 3.13b) shows the same isocontours of concentration ($C = 0.25$ in red and $C = 0.01$ in yellow) with cutting planes at $y/d = 20$ and at $x/d = 7$ (with an inclination angle of 5 degree) colored by the gradient of concentration. This visualization shows the regions of molecular and subgrid-scale mixing. Strong gradients are observed in the near-field, especially at the interface between the jet and cross-flow, which shows a convoluted shape. In the wake region, the footprint of the Counter-rotating Vortex Pair (CVP) is observed with two distinct alleys in the $x/d = 7$ plane (the two lobes of the kidney shape crosses this plane). In the $y/d = 20$ plane, broadband mixing is present, with stronger gradients at the outer envelope of the jet than inside it, where turbulent mixing homogenize the mixture of jet fluid and air.

We now focus on the near-field, where coherent structures form and transition to turbulence. There are three main classes of vortices in the present configuration, (1) the ring-vortices, (2) the counter-rotating vortex pair, and (3) the V-shape vortices. Other vortex classes are wake vortices, horse-shoe vortex and vortices composing the far field turbulence.

Ring vortices (also called "shear-layer vortices" or "span-wise rollers") appear in the near-field of the jet shear layer. Figure 3.14a) shows a 3D visualization of the flow field, with a $C = 0.5$ isocontour in red, a $C = 0.01$ isocontour in yellow and a $Q = 1$ isocontour in blue. Ring vortices

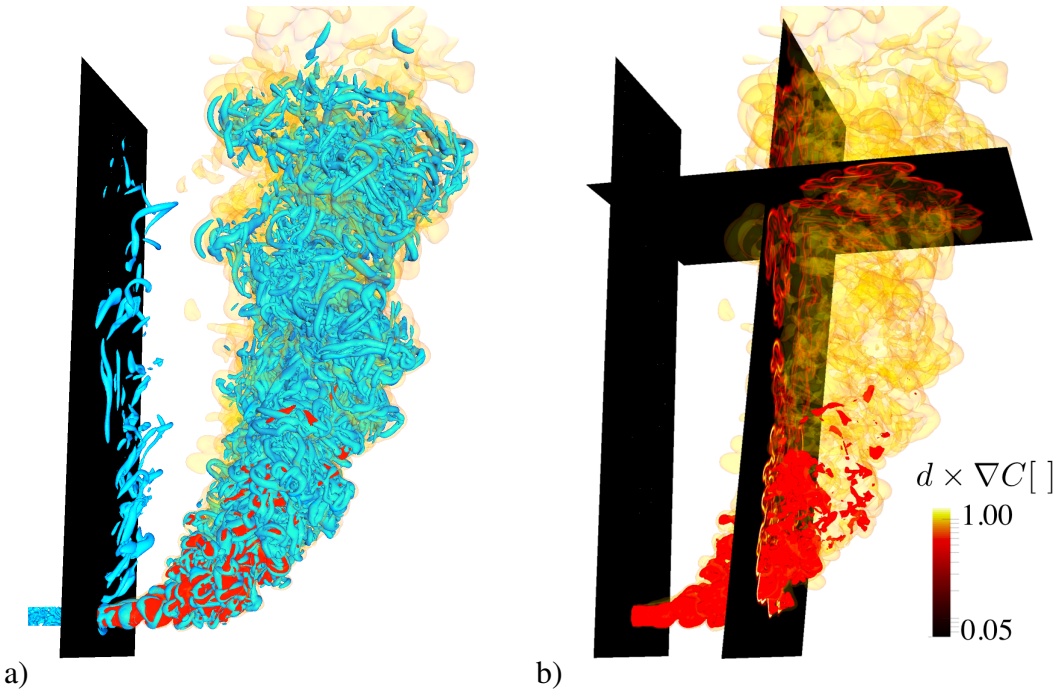

Figure 3.13. Instantaneous 3D visualizations of the flow field. a): the blue iso-contour is $Q = 0.02$, the red iso-contour is $C = 0.25$ and the yellow iso-contour is $C = 0.01$. b): cutting planes colored by ∇C. Red and yellow iso-contours: same as a).

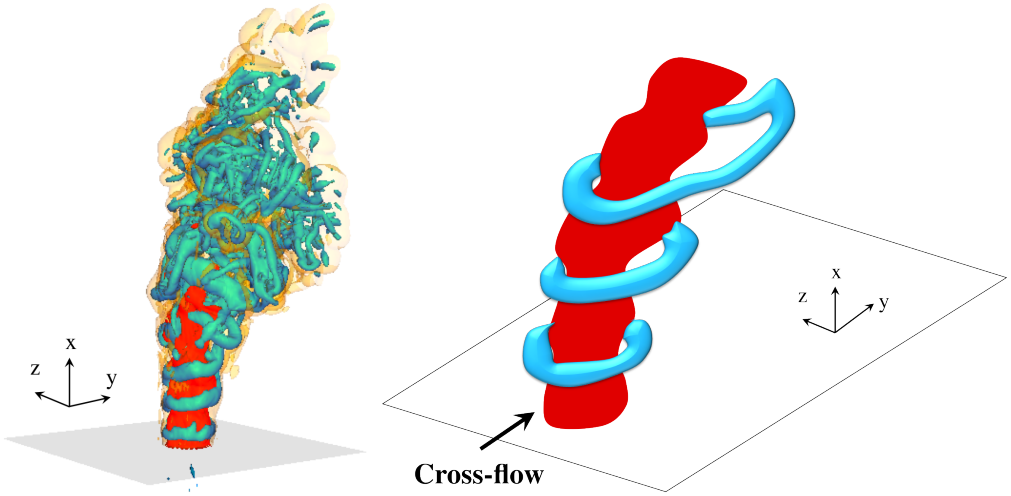

Figure 3.14. Vortex rings in a JICF. a) 3D visualization with red: $C = 0.5$, yellow: $C = 0.01$, blue: Q=1 and b) schematic representation

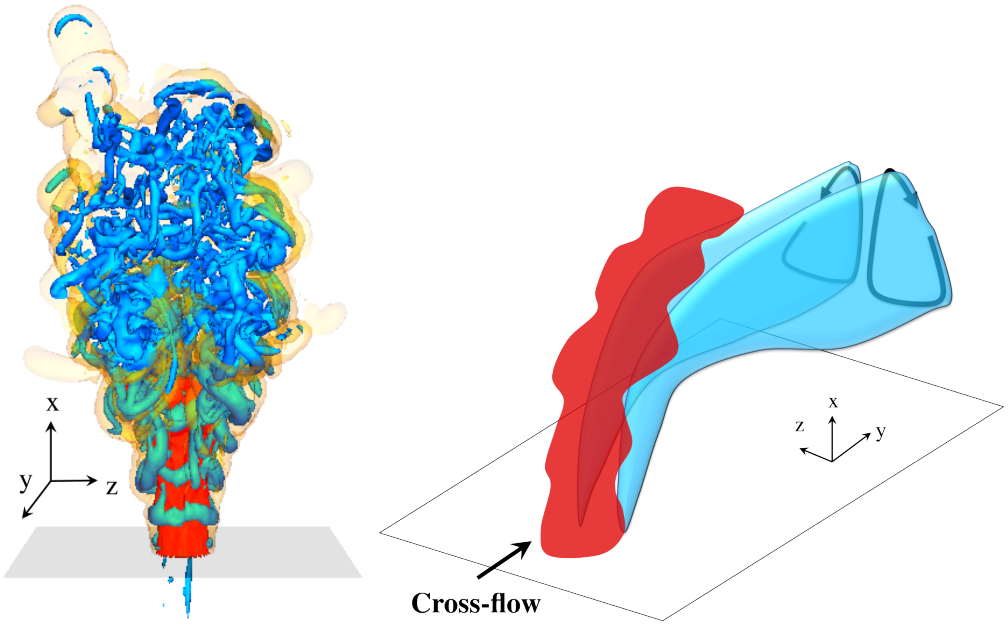

Figure 3.15. Counter-rotating vortex pair in a JICF. a) 3D visualization with red: $C = 0.5$, yellow: $C = 0.01$, blue: Q=1 and b) schematic representation.

result from a Kelvin-Helmholtz (KH) instability of the shear layer that surrounds the jet as shown schematically in Fig. 3.14b). This class of vortex has been observed in many experimental studies and their creation is well understood theoretically [92, 93, 94].

The second class of eddies is the large counter-rotating vortex pair (CVP) due to the "obstacle effect" created by the jet in the cross-flow. The pair forms on each side of the jet, in the shear layer between the low speed zone behind the jet and the faster cross-flow. The two counter-rotating vortices are bent by the cross-flow. Far downstream, this makes their rotational axis almost parallel to the cross-flow. Figure 3.15a) shows that in this region, the so-called 'vortex pair' is actually a large collection of small vortical structures rotating in opposite direction.

Another important class of vortices is generated by the growth of an azimuthal instability of the ring vortices. We call these secondary instabilities 'V-shape vortices' here. These instabilities produce couples of small counter-rotating vortex pair with rotational axis parallel to the jet axis, as shown in Fig. 3.16. Similar vortices have been experimentally observed by Broze and Hussain [95] and numerically by Silva and Metais [96], in the context of turbulent round jets. In those studies, these streamwise structures are called 'varicoses' and constitute the first step of the dislocation process of the organized ring structures. In Yuan *et al.* [97], evidence of the presence of these vortices in a JICF is given, as their fingerprint is observed on some vorticity components. The great resolution of the current computation enables to clearly understand the spatial structure of these vortices. These vortices are responsible for "ejection" of jet fluid in the upstream cross-flow.

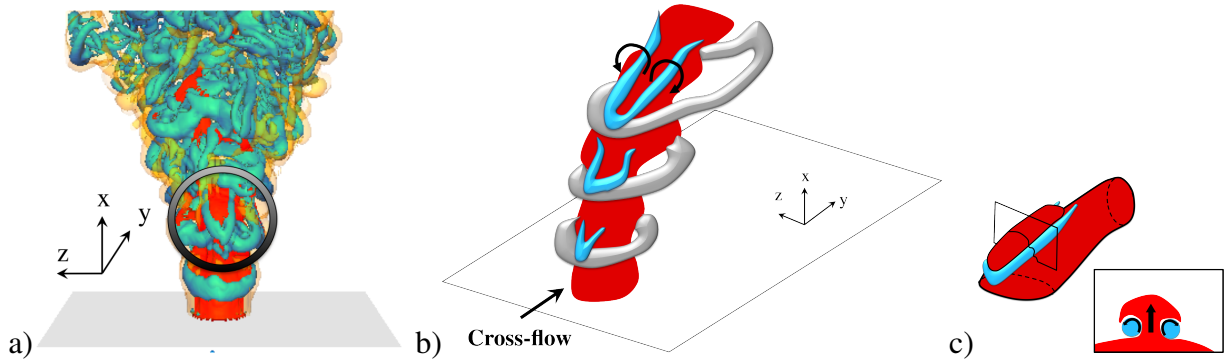

Figure 3.16. V-shape vortex in a JICF. a) 3D visualization with red: $C = 0.5$, yellow: $C = 0.01$, blue: Q=1 and b) schematic representation. c) schematic view of the fluid ejection mechanism by a V-shape vortex

This phenomenon is described in Fig. 3.16c) and explains the convoluted interface observed in Fig. 3.13b), at the bottom location in the $x/d = 7$ plane.

The horse-shoe vortex is mentioned here, as it is a known coherent structures in this type of flow. This vortex is very stable, and settles upstream of the base of the jet close to the wall. This vortex is a consequence of the adverse-pressure gradient generated by the varying stagnation pressure of the cross flow on the jet surface [94]. Compared to other vortices, however, its circulation is weak. Its role in turbulent mixing is marginal at the present conditions and will not be discussed further in the following. Wake vortices are sometimes observed in the present JICF but they are not dominant in mixing jet fluid and air at the present velocity ratio. This is due to the low Reynolds number associated with the cross-flow of air, which limits vortex shedding. Finally, broadband turbulence forms in the far-field region, downstream of the turbulent breakdown of the jet tip. These structures appear when the previous types of eddies have lost their regular arrangement and lead to chaotic motions. They are observable far-downstream of the injection in Fig. 3.13a).

Quantitative assessment of turbulent scales

Using imaging, the scales of turbulence have been described qualitatively in Sec. 3. A quantitative evaluation of turbulent scales in the present JICF is now provided, using various complementary techniques. The ensemble of results provided here is useful for designing optimized LES meshes, which balance cost and precision.

Integral scale

Using dimensional analysis in fully-developed turbulence, one can construct a turbulent length scale based on turbulent kinetic energy k and its dissipation ε. This scale is called the integral length scale and reads:

$$l_t = k^{3/2}/\varepsilon \tag{3.4}$$

with $k = \overline{u'^2 + v'^2 + w'^2}/2$, $u'_i = \tilde{u}_i - \overline{\tilde{u}_i}$, for i =1,2,3, and $\varepsilon = \overline{(\mu + \mu_t) S_{ij} S_{ij}}$, $S_{ij} = \left(\partial \tilde{u}_i/\partial x_j + \partial \tilde{u}_j/\partial x_i\right)/2$.

Figure 3.17 shows 2D maps of l_t in a) the jet centerplane and b) the transverse plane at $y/d = 17$. Figure 3.17a) shows a global increase of the integral length scale with increasing distance from the jet nozzle exit, following the jet trajectory. Distinct regions can be observed: 1) the boundary layer perturbed by the jet, 2) the wake region which contains structures with large time and length scales 3) the CVP region, which contains the large CVP structure as well as broadband turbulent mixing (which do not appear on the integral scale map, dominated by the largest scales of the flow).

With this map, we can also quantify how the integral scale actually growth with increasing distance from injection. In Fig. 3.17, solid lines indicate the center streamline as well as two additional curves following the jet trajectory on the wind-side and lee-side of the jet, defined as:

$$\frac{x}{rd} = A\left(\frac{y - y_0}{r}\right)^{0.3} \tag{3.5}$$

with :

$$\text{lee side: } A = 1.6, y_0 = 0.5 \tag{3.6}$$

$$\text{wind side: } A = 2.2, y_0 = -0.5 \tag{3.7}$$

with $r = 5.7$, the velocity ratio. In Fig. 3.18 the integral scale is plotted vs the curvilinear-abscissa defined on these curves. In the near-field, the integral scales grow near-linearly before the jet turbulent breakdown. The latter is defined as the location where the maximum value of k is observed along the jet center streamline, and is located at $s/d = 4$ here. After $s/d = 4$, the growth rate of the integral scale is smaller and appears to grow at a rate of $(s/d)^{1/3}$, on the center streamline and on the wind-side of the jet. This is consistent with the growth rate of the axisymmetric wake flows measured experimentally [98]. This $1/3$ scaling is also observed in the far-field measurements of concentration in JICFs [87, 89]. On the lee-side of the jet, the integral scale grows at a higher rate than $(s/d)^{1/3}$ and scales are much bigger than on the jet center-streamline or on the wind-side of the jet. At $s/d = 17$, the integral scales is approximately equal to $1.5d$, $2d$ and $3d$ on the wind-side, the center and the lee-side of the jet, respectively, which shows the strong inhomogeneity of turbulence in a JICF. Figure 3.17b) shows the map of integral scale in the transverse plane at $s/d = 17$, and enables one to understand the 3D distribution of integral scales in a JICF. On the outer-edge of the jet, at the interface with the cross-flow, small turbulent scales are generated. At the center of the jet, large-scale turbulence are observed and below that, two lobes of large integral scales are present in the CVP lobes. A column of small scales turbulence is also present between the jet and the wall, which is due to growing boundary layer vortices downstream the jet, as shown in Fig. 3.13a).

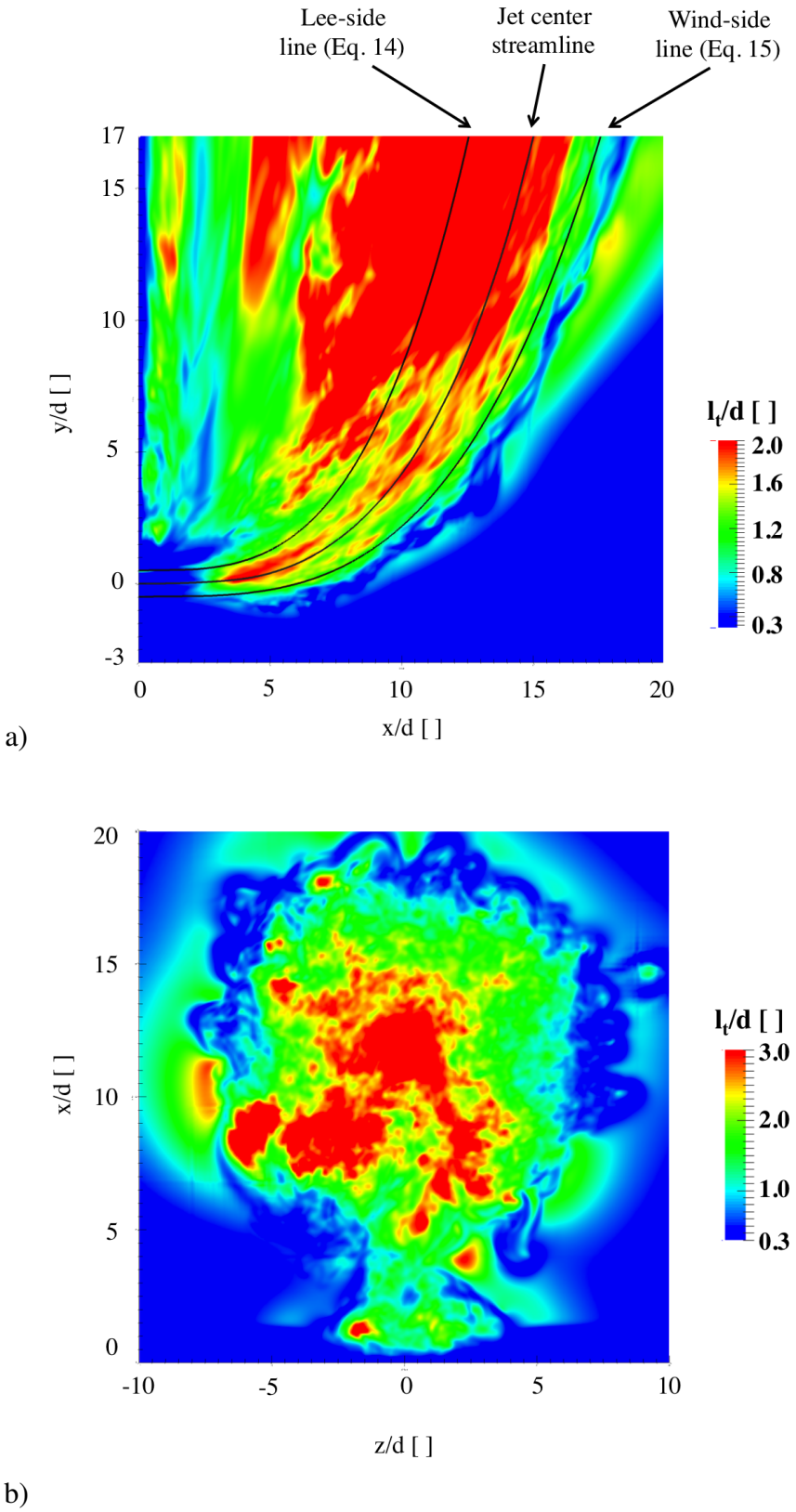

Figure 3.17. Map of integral scale in a) the jet centerplane (z/d=0) and b) a transverse plane at $y/d = 17$. Note that the legend range is different in a) and b).

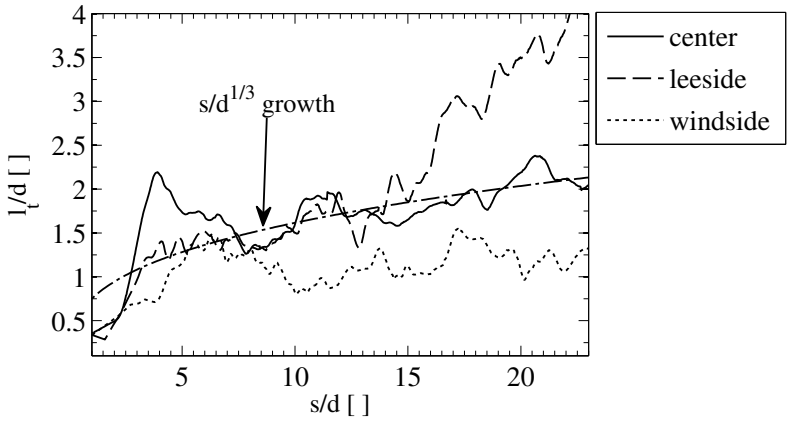

Figure 3.18. Integral scale versus curvilinear-abscissa on the jet center streamline, the windside and leeside lines depicted in Fig. 3.17a).

Note that the map of integral scale is a ratio of two ensemble averaged quantities and it requires a long integration period for a full statistical convergence. Even though the map presented in Fig. 3.17a) still has some fluctuations due to the limited time-averaging period (=20 flow through times), the present information can still be considered as quantitative and reliable. Indeed, the integral scale map obtained with only half of the present integration period gives similar results.

Although the integral scales computed from dimensional analysis enables a quantification of the growth of turbulent structures in the region with developed turbulence, it cannot identify the size of developing coherent structures in the near-field. The following sections are aimed at providing a better description of the latter structures.

Taylor Micro-scale

The Taylor micro-scale is often used in studies of turbulence. In a Homogeneous Isotropic Turbulence (HIT) this scale is proportional to the amount of TKE dissipation, although it is much bigger than the Kolmogorov scale, at which dissipation occur. This is why we can estimate this scale using high-fidelity LES, without resolving all the dissipative scales of turbulence. The Taylor micro-scale is defined from the correlation of a local fluctuating signal with neighbouring signals. The spatial correlation reads:

$$C_i(\boldsymbol{x},r) = \frac{\overline{\phi'(\boldsymbol{x},t)\phi'(\boldsymbol{x}+r\boldsymbol{e_i},t)}}{\overline{\phi'^2(\boldsymbol{x},t)}} \tag{3.8}$$

where the overline denotes a long-time average, $\phi' = \phi - \overline{\phi}$ is a scalar fluctuation, here we take $\phi = (u'^2 + v'^2 + w'^2)/2$, $\boldsymbol{e_i}$ is the unit vector in the i^{th} direction.

This gives a correlation profile for all points of the domain. In a HIT flow, in the vicinity of $r = 0$, the spatial correlation has a parabolic shape. The Taylor micro-scale is defined as the location where this parabola crosses the horizontal axis:

$$\lambda_i = \sqrt{-2/\left(\partial^2 C_i/\partial r^2\right)_{r=0}} \tag{3.9}$$

Even though the present flow is strongly inhomogeneous (as shown for instance with Fig. 3.17a)), the spatial correlation profiles appear to have a parabolic shape in the vicinity of $r = 0$ in a large part of the computational domain. Thus, useful information can be extracted from the Taylor micro-scale.

Because the current flow is non-isotropic, the Taylor micro-scale has different values in all three directions. In order to show a map of turbulent scales, we consider the average of the Taylor micro-scales obtained in all three directions:

$$\lambda = 0.5\sqrt{\lambda_1^2 + \lambda_2^2 + \lambda_3^2} \tag{3.10}$$

Figure 3.19 shows 2D maps of λ in a) the jet centerplane and b) the transverse plane at $y/d = 17$. Small-scale structures are observed within the shear-layer near the jet exit, with a size approximately equal to $0.2\ d$. These small-scale structures persist until turbulent breakdown occur, once the two shear-layers meet and interact. Then turbulent-structures grow with increasing distance from the jet nozzle, following the jet trajectory. Small-scale structures are formed on the outer-edge of the jet, because of a large velocity gradient between the bending jet and the accelerating cross-flow. On the inner-edge of the jet, in the wake of the jet nozzle, turbulent structures are much larger than in the rest of the domain, with a characteristic length scale greater than $0.5\ d$. Near the wall, at the beginning of the boundary layer in the wake of the jet, a region with small-scale structures is observed. In this region, vortices are formed as a result of flow separation events, which is a well known phenomenon for wake vortices generation [94].

In Fig. 3.20 the Taylor micro scale is plotted vs the curvilinear-abscissa defined on the jet centerline, the wind-side curve and the lee-side curve (see Eq. 3.5). Overall, the Taylor micro-scale appears to grow as $(s/d)^{1/3}$ throughout the computational domain, and the turbulent scales are smaller on the wind-side of the jet than on the jet centerline or the lee-side of the jet. Far downstream, scales on the center-streamline and the wind-side of the jet are comparable, whereas they are much larger on the lee-side of the jet. In the far-field the $1/3$ scaling agrees with the one obtained from the integral scale analysis presented in Sec. 3. In the near-field however, the Taylor-microscale indicates that the growth of turbulent structures is smaller than a linear increase. The Taylor micro-scale is a more accurate representation of the size of the coherent structures in the near-field than a dimensional analysis. Thus, an optimal LES mesh would preferably use a $(s/d)^{1/3}$ scaling for the local cell sizes in the computational domain. One could also use the curve trajectories defined in Eq. 3.5 to guide the distribution of grid points.

Figure 3.19b) shows the map of Taylor micro-scale in the transverse plane at $s/d = 17$, and enables one to understand the 3D distribution of turbulent scales in a JICF. On the outer-edge of the jet, at the interface with the cross-flow, small turbulent scales are generated, with a characteristic size as small as $0.2d$. The region at the center of the jet and below it contains turbulence with

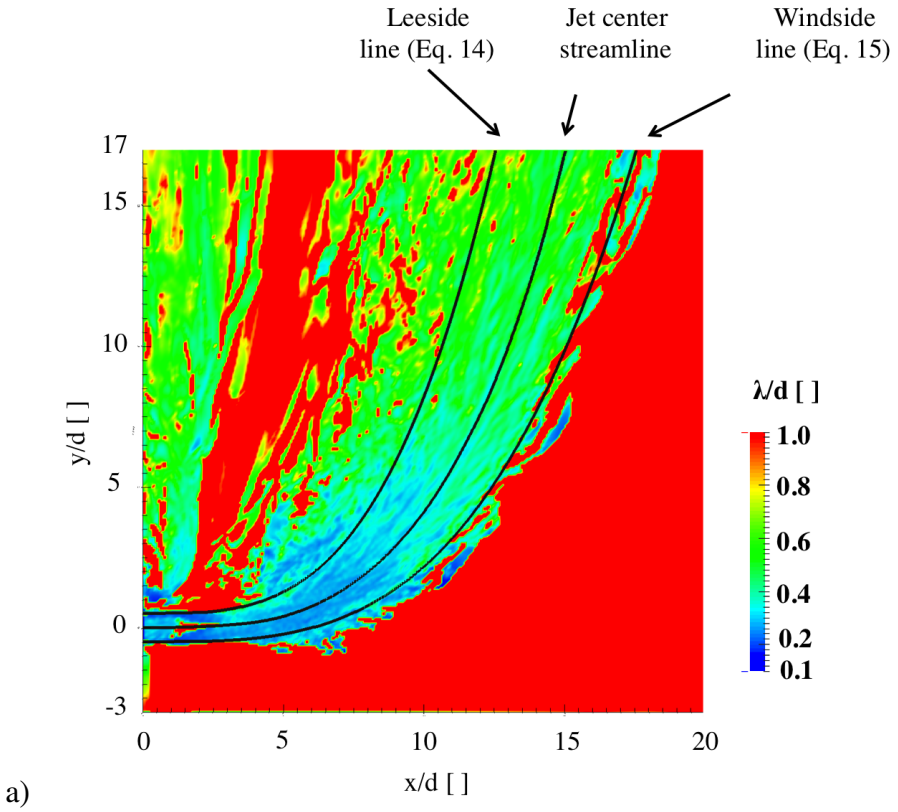

a)

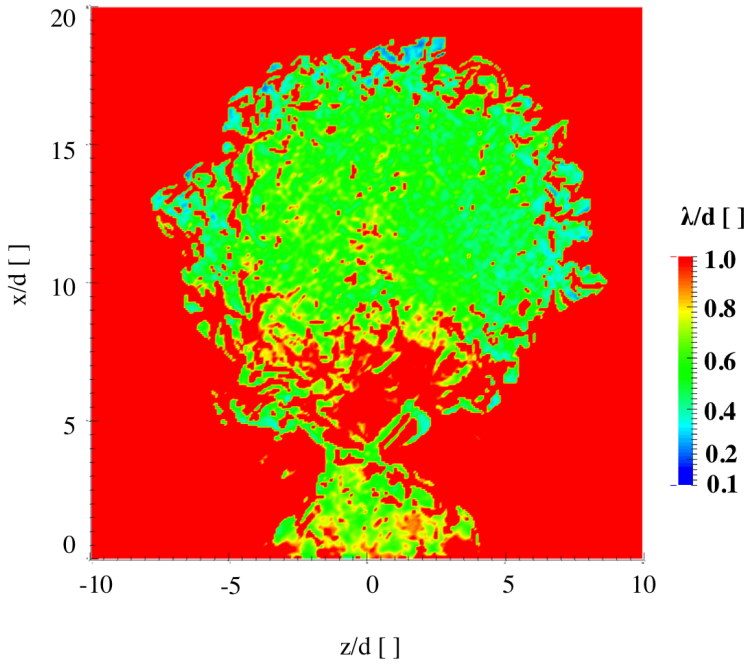

b)

Figure 3.19. Map of Taylor microscale λ (Eq. 3.10) in a) the jet centerplane (z/d=0) and b) a transverse plane at $y/d = 17$.

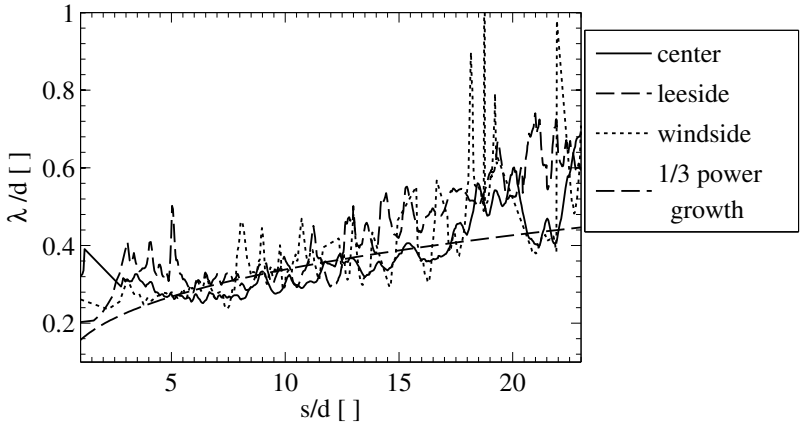

Figure 3.20. Taylor micro-scale λ (Eq. 3.10) versus curvilinear-abscissa on the jet center streamline, the windside and leeside lines depicted in Fig. 3.17a).

bigger scales, which are in the $0.4d - 0.7d$ range. The wall turbulence shows larger characteristic sizes, in the $0.6d$-$0.9d$ range. This information can be used to design an optimized LES mesh for the present configuration.

Although the map provided in Fig. 3.19 appears 'noisy' and not well converged, it has been obtained using a very large number of time-resolved snapshots (= 800), corresponding to a large time-period (20 flow-through times). The 'noise' comes from the fact that the correlation profile sometimes do not follow a parabola in the vicinity of $r = 0$, which can give negative values of $\left(\partial^2 C_i/\partial r^2\right)_{r=0}$. To prevent an ill-defined value for the Taylor micro-scale (see Eq. 3.9), such values are thresholded and this is what induces the visual 'noise' in Fig. 3.19. Obtaining a smoother map of Taylor micro-scale would require a lot more computational time, which does not seem necessary in the light of the information already given by the present map.

Turbulent spectra

In this section, 200 time-resolved probes are analyzed. The latter are placed along each of the wind-side and lee-side curves defined by Eq. 3.5, as well as along the jet center streamline. Signal processing techniques are used to study turbulent spectra as a function of curvilinear distance from injection. The spectrum averaging procedure of Welch [99] is used here to enable a deterministic Power Spectrum Density (PSD) estimate from a chaotic turbulent signal with finite length (20 Hamming windows). Local values of TKE are actually extracted from many 3D snapshots (= 800) acquired at a non-dimensional frequency (Strouhal number) of $St = f\ d/U_j = 2.3$ (snapshots are stored every 8 time-steps, with $dt\ U_j/d = 0.053$), which enables a spectrum analysis up to the Shannon frequency of $St = 1.15$. Extracting local values from snapshots requires considerable

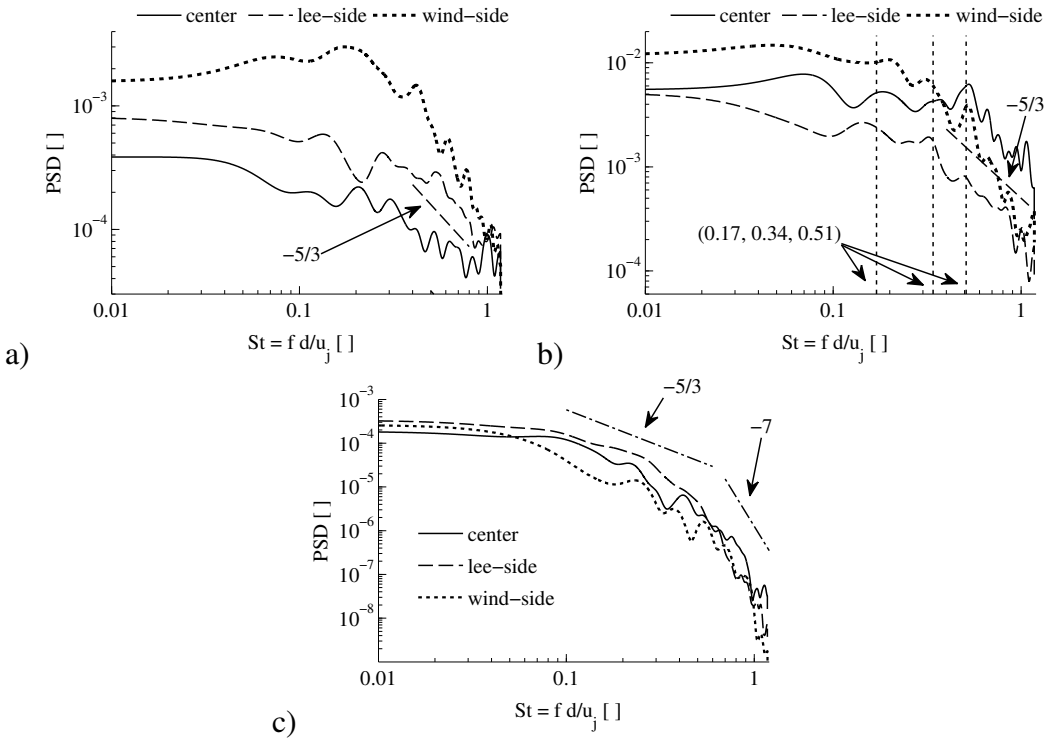

Figure 3.21. Turbulent Kinetic Energy spectrum vs non-dim frequency along the curves defined by Eq. 3.5 and along the jet center streamline, at a) $s/d = 2$, b) $s/d = 4$ and c) $s/d = 17$. Note that the range of PSD is adapted to each case to maximize visibility.

storage (5 TB of data) but allows to precisely position the probes along the predicted jet trajectory.

Figure 3.21 shows the TKE spectrum as a function of non-dimensional frequency at two stations in the near-field: a) $s/d = 2$, b) $s/d = 4$, and one station in the far-field: c) $s/d = 17$. Figure 3.21a) shows that at the jet center, the TKE spectrum corresponds to developed turbulence exiting the pipe, as a '$-5/3$' slope is observed. In the absence of mean velocity gradient at the jet center, coherent structures do not develop at this location as no peak is present in the PSD. The integral of the PSD (the power of TKE) is smaller at the jet center than on the lee-side and the wind-side of the jet. On the wind-side of the jet, a strong increase of TKE is observed in comparison with the jet center-streamline. This is due to strong KH instabilities developing at the interface between the jet and the cross-flow. The dominant non-dimensional frequency on the wind-side of the jet at $s/d = 2$ is $St \approx 0.2$. Subharmonics at $St \approx 0.4$, 0.6 and 0.8 are also observed. Visual observation of time-resolved evolution of coherent structures in the near-injector region (using scenes similar to Fig. 3.14) shows that regular ring-vortices correspond to the subharmonics at $St = 0.4$, 0.6 and 0.8 and the large PSD peak at $St = 0.2$ correspond to less frequent almalgamation events, where several coherent structures gather and provoke a strong velocity fluctuation when crossing the probe on the wind-side. An example of such an event is shown in Fig. 3.22. Figure 3.22a) shows an

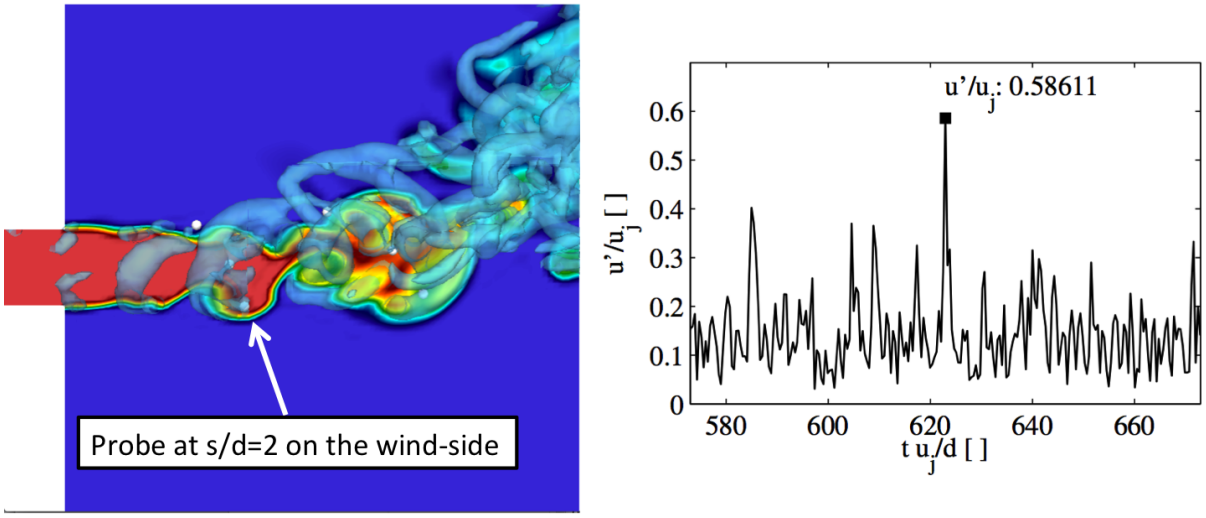

a) b)

Figure 3.22. a) Instantaneous view of the jet when a very energetic vortex crosses the probe on the wind-side at $s/d = 2$. b) Square root of the TKE signal on the wind-side of the jet at $s/d = 2$ versus time, in the vicinity of the event shown in a).

instantaneous view of the jet when a very energetic vortex crosses the probe on the wind-side at $s/d = 2$ and Fig. 3.22b) shows the square root of the TKE signal recorded by the probe. At this instant, the velocity fluctuation is very large and is equal to $0.6\,u_j$, as indicated in Fig. 3.22b). On the lee-side of the jet, the dominant Strouhal number is smaller than on the wind-side and is equal to $St \approx 0.15$. Similarly to the wind-side of the jet, subharmonics are observed at $St \approx 0.3$, and 0.6. On both sides of the jet, TKE accumulates in the low-frequency range (large spatial scales) and the transfer to high-frequency range (small spatial scales) is not as effective as in fully-developed turbulence as the absolute value of the slope is larger than $5/3$. At $s/d = 2$, the spectra thus correspond to a superimposition of the developed turbulence exiting from the pipe and the nascent coherent structures in the shear-layers.

At $s/d = 4$, Fig. 3.21b) shows a qualitatively similar spectrum on the wind-side of the jet, with strong modes at $St = 0.2$, 0.3, 0.5, and a small transfer rate to high-frequencies. On the jet center-streamline, strong modes are observed at $St = 0.2$, 0.35, 0.5, as well as a transfer rate to high-frequencies close to $-5/3$, even though peaks are observed instead of fully-broad band mixing. The peak at $St = 0.5$ is particularly strong on the jet center streamline. Visual observation of the jet indicates that this is due to the staggered arrangement of the coherent structures in the range of $St = 0.2 - 0.3$ on the wind-side and lee-side of the jet, which induces this higher frequency mode on the jet center streamline: twice as much coherent structures cross the probe location, alternatively originating from the wind-side or the lee-side of the jet. On the lee-side of the jet, although modes are observed at $St = 0.15$, 0.3, 0.5, these modes are weak and TKE is overall weaker (the integral is smaller) and shows a transfer of energy to high-frequencies representative of developed turbulence. This is due to the recirculation zone existing in the wake of the jet (induced by the nascent CVP), which recycles downstream turbulence back into the lee-side of the jet. This is also due to the coherent structures that formed on the wind-side of the jet, which are transported downstream and broken down during this convective transport (large-residence time). Thus, at $s/d = 4$, which corresponds to the turbulent breakdown region, both coherent structures and broadband turbulence are present. The modes observed in Fourier space corresponds to the ring vortices, CVP and V-shape vortices (described in Sec. 3) in the physical space.

Figure 3.21c) shows that far downstream, at $s/d = 17$, both an inertial range ($-5/3$ slope) and a dissipation range (-7 slope) is resolved by the present high-fidelity LES. On the center streamline and on the wind-side of the jet, modes can still be observed in the inertial range, which indicates that small-scale structures forms at the outer shear-layer between the jet and the cross-flow, even in the far-field region. This is consistent with the maps of turbulent scale provided in Figs. 3.17 and 3.19.

Figure 3.23 shows a map of turbulent kinetic energy spectrum as a function of non-dimensional frequency and curvilinear distance defined along the a) wind-side curve, b) center streamline, and c) lee-side curve (see Eq. 3.5). For $s/d \leq 2$, TKE develops on the wind-side and lee-side of the jet whereas it is very small on the jet centerline. This corresponds to the development of coherent structures in the shear-layers, as explained previously with Fig. 3.21a). The maximum of TKE is located in the vicinity of $s/d = 4$ for the wind-side of the jet and for the jet center-streamline. This corresponds to the turbulent breakdown of coherent structures. On the lee-side of the jet, turbulent breakdown is slightly delayed and is located at $s/d \approx 5$. After this turbulent breakdown,

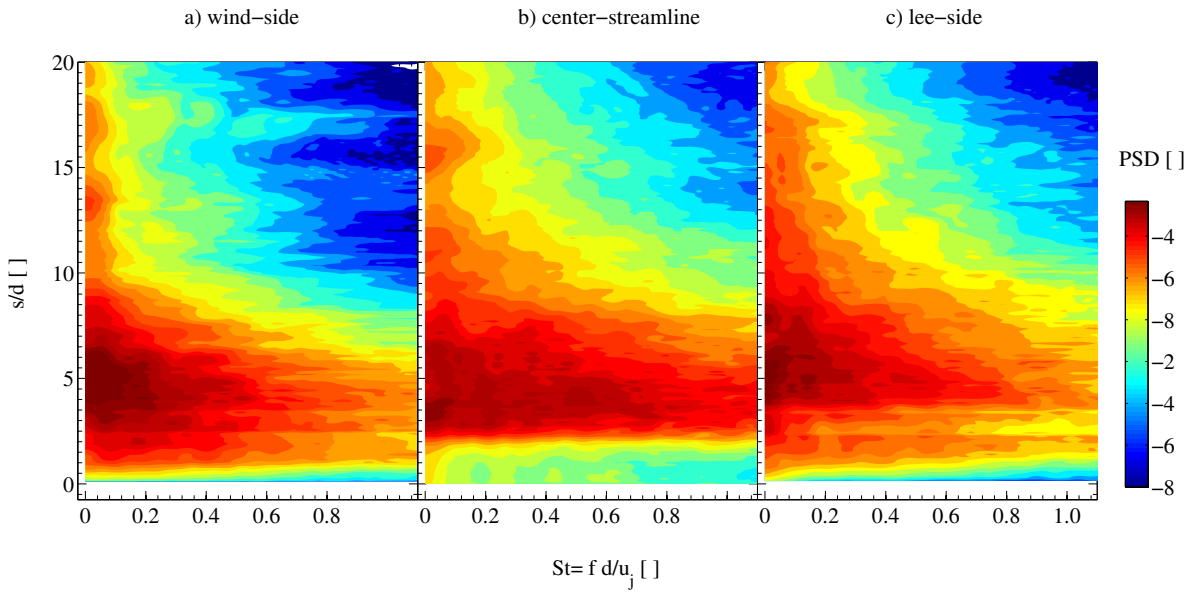

Figure 3.23. Turbulent Kinetic Energy spectrum as a function of non-dimensional frequency and curvilinear distance defined along a) wind-side curve, b) center streamline, and c) lee-side curve (see Eq. 3.5)

a classical energy cascade is present for both sides of the jet, as well as for the jet center-streamline. Further downstream ($s/d >= 7$), one can observe how the developed TKE spectra evolve with the jet trajectory. TKE progressively decreases with the distance from injection. Characteristic times of turbulence increase, and spatial scales grow as the spectra shift towards smaller frequencies. This is due to amalgamation at large spatial scales and dissipation at small spatial scales. On the wind-side of the jet, spatial scales do not grow as much and deterministic modes in the TKE spectrum are observed in the high-frequency range (small spatial scales). This is consistent with the observation of integral scale in Fig. 3.17 and Taylor-microscale in Fig. 3.19, and is related to the generation of small-scale turbulent structures in the outer shear-layer between the jet and the cross-flow. On the lee-side of the jet, more TKE is present in the large spatial scales than on the jet center-streamline and wind-side of the jet, consistently with the maps of turbulent scales provided in Figs 3.17 and 3.19.

Scalar gradient thicknesses

In this section, we characterize how scalar gradients evolve with downstream distance from injection. Although it has been shown in Sects. 3-3 how turbulent scales evolve in the 3D field, it is not straightforward to determine how resolved scalar gradient thickness are linked with turbulent scales. Indeed, on the outer edge of the jet, persisting large concentration gradients are present between the jet and the cross-flow of air. Inside the jet, scalar gradients are smaller because jet fluid and engulfed air have been mixed by turbulence and diffusion.

In order to determine the gradient thickness, we use the following post-processing procedure. First, we define a line length $l = 3d$. Then, we define a 3D sub-domain V3D with a size: (20d, 1d+l, l), centered on y. The 3D gradient of concentration is computed within this 3D sub-domain. Then, we define a 2D sub-domain V(y) embedded within V3D, with a size: (20d, 1d), centered on y and $z/d = 0$. In this domain, we identify the value for the maximum concentration gradient magnitude $|\nabla C|_{\max}$. Then, we pick a threshold $\alpha = 0.1$ and conduct multiple 1D cuts of length l ($n_{\text{cuts}} = 200$) along the 3D gradient direction, in regions where the concentration gradient magnitude is higher than $\alpha \times |\nabla C|_{\max}$. These cuts are further analyzed to identify the gradient thickness. Within each cut, the maximum concentration gradient magnitude is identified, and the minimum distance $d_{\min}$ separating the location of this maximum value to location where half of this value is reached is determined. We finally define the gradient thickness as:

$$\delta_{|\nabla C|} = 2d_{\min} \tag{3.11}$$

Figure 3.24a) shows the mean value of $\delta_{|\nabla C|}$ in V(y) as a function of y. Near the injector exit, in the vicinity of $y/d = 0$, the gradient thickness is approximately equal to three LES filter width ($\delta_{|\nabla C|} = 0.18$). This is due to stiff concentration gradients that are not fully-resolved but handled numerically by the upwind convective scheme. Then, a linear increase is observed until $y = 2.5d$, as turbulent mixing starts to diffuse the concentration gradient. For $y > 2.5\ d$, the gradient thickness increases very slowly. The mean gradient thickness at $y = 15.5d$ is equal to $0.3\ d$, which is only 10% greater than the mean gradient thickness at y=2.5d, which is equal to $0.28d$. As air is

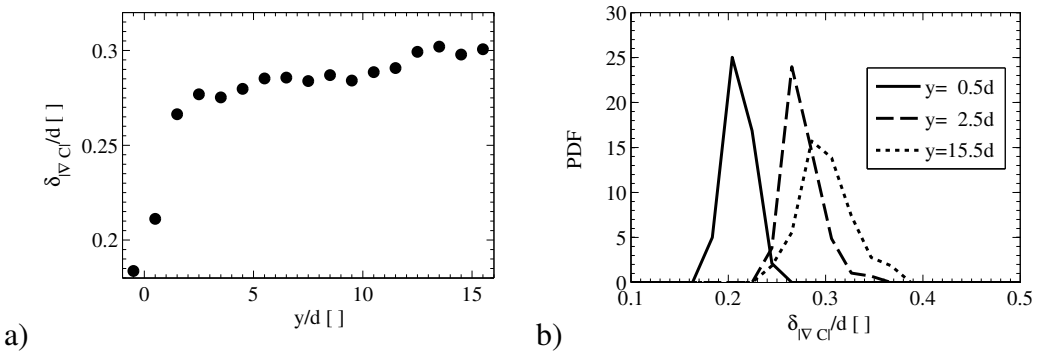

Figure 3.24. a) Mean gradient thickness in V(y). V(y) is an interrogation volume which is 1 d high and 20 d long, centered on y. b) PDF of gradient thickness within V(y), for 3 increasing values of y.

regularly engulfed into the wake of the jet, scalar gradients are still strong at the outer edge of the jet, as shown previously in Fig. 3.13b).

The Probability Density Function (PDF) of gradient thicknesses within V(y) is shown for three increasing values of y/d in Fig. 3.24b). Although the mean value of the gradient thickness do not significantly increase after turbulent breakdown, the PDF shows that the distribution of gradient thicknesses gets wider with increasing distance from injection. This is representative of the broadband turbulent mixing that occur in the wake of the jet.

This shows that in spite of the growth of turbulent scales, the maximum scalar gradients thickness stays approximately constant in the wake of the jet. This has important consequences in an engineering LES calculation. Indeed, if one stretches the mesh with a $1/3$ rate to approximately follow growth of turbulent scales in the wake of the jet (see Sects. 3-3), this would probably only be sufficient to accurately resolve turbulence without concentration gradients. If a scalar is transported by the flow, scalar gradients would be more and more filtered and high-order statistics such as scalar fluctuations or scalar dissipation rate, would be less accurately predicted. Since in a reacting flow case, combustion occur far downstream of the injection point, where scalar dissipation rate is on average smaller, the present work tends to indicate that mesh spacing should stay constant in the wake of the jet to accurately predict scalar gradients and thus flame stabilization. This would require more computational resources than what is ordinary used in such flow computations. This might be an imperative constraint for calculation accuracy, and this point will be the focus of further studies.

Conclusion

In this section two types of metrics have been tested to assess the quality of grid spacing in a transitioning mixing layer at device conditions and a three-dimensional jet in cross-flow:

- Temporally converged first and second moments of turbulent quantities (mean and rms) at all key locations in a flow.
- Local and spatial power spectra density (PSD) of the fluctuation energy of quantities of interest.

Temporally converged moments are good indicators of grid spacing convergence and are necessary for direct comparison with reference data from experiments. Local PSDs can be used to assess when grid is converged but also provide additional informations. They in particular give insights on energy transfer mechanisms between turbulent scales and can detect unphysical behavior such as the one presented in Fig. 2.6. Spatial PSDs bring key information on the development of turbulence in particular in transitioning flows. This last metrics is very insightful when coupled with an analysis of the different scales of turbulence.

These metrics have been tested in a high-fidelity Large-Eddy Simulation of turbulent mixing in the Jet-In-Cross-Flow configuration studied experimentally by Su and Mungal [89]. A good quantitative agreement is obtained between LES and detailed experimental measurements of mean velocity, mean concentration, Reynold stress tensor and turbulent flux of scalar. To the author's knowledge, such an extended validation of LES results in a JICF has never been conducted before and confirms that high-fidelity LES is a good instrument for predicting complex 3D turbulent flows.

Using this validated simulation results, we presented in details the turbulent mixing phenomenology for the present configuration and how turbulent scales spatially evolve in a JICF. Various quantities are mapped (integral scales, Taylor-micro scales, turbulent spectra) and a similar spatial evolution is observed: scales grow near-linearly before turbulent breakdown of the jet, then a '1/3' power law is observed, consistently with a wake scaling. This shows that a linear stretching of the mesh from injection point to the far-field is too strong and might impact the far-field predictions of turbulent mixing by filtering out key turbulent structures present in the wake of the jet. In the far-field, neglecting the curved trajectory of the jet and assuming the trajectory of the jet is parallel to the wall, we recommend keeping a stretch rate smaller than $y/d^{1/3}$ to follow the growth rate of the integral scale along the jet centerline and in its wake. smaller cells should however be placed at the outer edge of the jet (with $dx = O(d/3)$), to capture the interaction between the jet and the cross-flow, which give rise to small vortical structures which inject energy in the turbulent kinetic energy spectrum.

This page intentionally left blank.

Chapter 4

Model error analysis with Uncertainty Quantification

Introduction

After studying the impact of grid spacing on accuracy of LES in the previous two Chapters, we concentrate here on model errors. As presented in the introduction of the report, many strategies have been previously tested to assess errors in models. One approach that seems promising is to couple LES with formal Uncertainty Quantification methods (UQ) in a non-intrusive way. Fortunately, such methods are developed at Sandia under the direction of H. Najm and B. Debusschere. The present EC-LDRD has been the opportunity to initiate a collaboration between our LES group and the UQ group. The collaboration is currently growing with the work of one postdoc (Layal Hakim) developing chemical kinetics for LES using Bayesian Inference method. This work will also be summarized in the following as being an important piece of the LDRD.

To investigate model errors, a numerical platform based on an actual burner has been established following guidances from the International Workshop on Turbulent Non-premixed Flames (TNF). This experiment is the bluff-body burner operated at Sydney University. It has been selected for the large and detailed available database that is required for the UQ analysis and also for its relevant complexity and similarity with actual industrial devices.

Within a "classical" simulation using the Raptor solver, the number of uncertain parameters is on the order of 100 to 150. This number depends on five main domains of the computation: the boundary conditions, the grid,the geometry, the models and the numerics. Depending on the different modeling strategies, this number can increase or decrease significantly. A list of the uncertain parameters for Raptor is shown in Tab. 4.1 for a specific scramjet simulation. In the present analysis only three parameters are assumed uncertain and all other are kept fixed. The three parameters are the Smagorinsky constant of the turbulent closure, and the turbulent Schmidt and Prandtl numbers. When models such as the well-known Smagorinsky model [100] are employed, significant uncertainties exist due to the use of an adaptable model parameter. The correct selection of the model parameter C_s is essential for accurate results. In early literature, C_s was often hypothesized to be a universal constant related to the model. Different values over the range $0.065 < C_s < 0.346$ have been used based on both empirical fits and theoretical estimates [101, 102]. Discretization of the LES equations adds further complications due to the fact that modeling and discretization errors strongly interact and are difficult to separate [103, 104, 4, 6]. Thus, a good selection of the

Type of model	Number of parameters	Comments
		Boundary conditions: 46 parameters
Air Inflow	8 param	Three mean velocities and three RMS, composition and temperature (+ pressure if supersonic)
Wall	8 param (2 per section) Sections are: isolator, cavity, combustor and , downstream nozzle	Wall function (1 param), Tre
Fuel injection	30 (10 per injector array)	Model: drop model. Drop size distribution (2 param: mean and variance) Velocity distribution (2 param / velo = 6 total) mass flow rate and temperature
		Models: 29 if Flamelet or $(ns+5\times nr+7)$ if finite rate chem
Turbulent/mixing closure	1 or $(ns+2)$ param	If dynamic Smagorinsky (kernel size for filtering), or Static Smogorinsky: Pr_t, ν_t, $Sc_{t,k}$ k being the number of species in the computation and ns the total number of species
Spray model	3 param	Taylor Analogy Breakup (secondary atomization) Note: no param for mass and heat transfer as models rely on thermo equilibrium
Chemistry	$3\times(2+4)$ param	If Flamelet approach is used (3 eqs for Z1, Z2, Z3) one for each injector location 3 diffusion coefs for progress var (C1, C2, C3) 3 diffusion coefs for mix frac (Z1, Z2, Z3) Arrhenius term (4 param) for each progress var.
	or $5\times nr$ param (nr: number of reac)	If finite rate chemistry is used pre-exp factor, activation energy, temperature exp exponents on concentrations
Combustion closure	1 param 2 param 0 param	For Flamelet approach For thickened flame approach (thickening and efficiency) For stockastic model
Equation of State	1 param	Ideal, or Cubic (SRK or PR)
		Grid: 33 parameters
Grid spacing	16 param in x	For each section, tanh variation of the grid spacing 4 param per section (isolator, cavity, combustor and nozzle): Δ_{x1}, Δ_{x2},x_{trans}, thick
	16 param in y	Same thing as above
	1 param in z	Constant spacing in the z dir (Δ_z)
		Geometry: 8 parameters
Walls	5 param	3 lengths and 2 angles can be ajusted (cavity length, depth, length inlet, angle cavity and angle combustor).
Injectors	3 param	locations of injector can be varied for optimization
		Numerics: 4 parameters
Stabilization	3 param	Choice of the method: QUICK, MUSCL or 1stO, sensor type and sensitivity
Time integration	1 param	Dual time steping or explicit rk4

Table 4.1. Uncertain parameters in Raptor for a representative calculation.

Smagorinsky coefficient is important, but difficult in practice. This is compounded by the fact that the dynamic procedure does not guarantee an optimal setting of the Smagorinsky model [105, 5]. These difficulties, errors, and uncertainties are further amplified in computations of turbulent reacting flow given the strong nonlinearity of chemical models, the large range of active chemical time and length scales, and the introduction of yet another level of modeling of chemical reaction processes. To the authors' best knowledge, only one investigation of uncertainty quantification (UQ) in LES for reactive flows has thus far been reported in which the uncertainty in the density field is propagated through the LES governing equations [106]. In the context of LES of non-reactive flows, Lucor *et al.* [107] have investigated the effect of uncertainty of the Smagorinsky coefficient on the turbulent kinetic energy.In the greater context of laminar flames, Warnatz [108] examined the effect of uncertainty in reaction rate coefficients on model outputs through sensitivity analysis. Smooke *et al.* [109] showed that axial and radial profiles of the sensitivities of model responses with respect to rate coefficients of chemical reactions exhibit similarity in laminar flames. Duchaine *et al.* [110] recently examined the sensitivity of the flame transfer function for laminar premixed methane/air flames to acoustic forcing using direct numerical simulation (DNS).

Focusing for the present on uncertainties in C_s and other LES model parameters, it is of interest to explore the associated uncertainties in computations of turbulent reacting flow. Although nominal values of these parameters are typically known, with perhaps some estimation of meaningful uncertainty ranges, based on available experience, a proper characterization of their uncertainty is lacking. Placing ourselves in a probabilistic context, where we represent uncertain quantities as random variables/fields, a joint probability density function (PDF) on the uncertain input parameters is required for complete characterization of input uncertainty. This joint PDF can be established employing Bayesian inference techniques with available experimental measurements of model output observables. However, the computational cost of each LES flow solution is prohibitively high, excluding the direct use of the LES computation as the forward model for inference purposes. A very common solution is to employ a *surrogate* model that (a) adequately represents forward model observables and their dependence on input parameters, and (b) is sufficiently efficient from a computational perspective to allow its use in the Bayesian inference procedure.

As Marzouk *et al.* [16] have shown, such model surrogates can be effectively built employing forward uncertainty quantification (UQ) methods with a presumed uniform density on the parameters of interest spanning their expected ranges. Forward UQ aims at providing a characterization of uncertainty in the output of a mathematical model given the uncertainty in its inputs. While Monte Carlo (MC) simulations are a convenient approach for this purpose, it is quite infeasible from a computational point of view for problems having complex models with computationally expensive forward runs, as is the case for LES. Stochastic spectral methods based on polynomial chaos (PC) expansions [18, 111, 112, 19, 113, 114] have proven to be effective alternatives to MC simulation for forward propagation of uncertainty in complex models. These methods involve the representation of uncertain/random model inputs and outputs using a functional basis in the form of a spectral expansion in terms of a set of independent and identically distributed (*i.i.d.*) standard random variables. Subsequently, the PC coefficients that completely characterize the output using such representation are obtained. The coefficients can be solved for using Galerkin or collocation approaches. Considering Galerkin methods in particular, there are both "intrusive" approaches where Galerkin projection is applied to the governing equations, and "non-intrusive"

methods where the projection integrals are evaluated numerically, *e.g.* using (sparse) quadrature approaches. Non-intrusive PC UQ methods can be easily implemented as they do not require any modification to the deterministic solver of the forward model.

In the present work, we aim to build PC surrogates for select quantities of interest (QoIs) in LES of turbulent combustion as functions of three parameters of interest, namely the Smagorinsky coefficient (C_s), and the turbulent Prandtl (Pr_t) and Schmidt (Sc_t) numbers. We focus on a turbulent non-premixed hydrocarbon flame stabilized on a bluff body. We build model surrogates using non-intrusive forward PC UQ methods with sparse-quadrature, given specified uniform parameter PDFs that cover the ranges of interest for these parameters. We examine the accuracy of the resulting surrogates at a set of randomly chosen points over the parametric space. Aside from the utility of the surrogates for subsequent statistical inference to establish posterior PDFs on these parameters, we also use them here to establish global sensitivity of different QoIs to the three parameters, and to examine correlations among the QoIs.

In the following, we present highlights of the LES and PC UQ methodologies, before proceeding to outline the problem setup, and presenting the results of the UQ investigation.

Polynomial Chaos based surrogate modeling

We adopt a probabilistic approach in order to quantify the uncertainty in the QoIs of the LES model. Within this framework, model parameters (C_s, Pr_t, Sc_t) and QoIs are modeled as random variables which are represented using PC expansions.

In particular, the PC representations of the QoIs are utilized as surrogate models, which, although slightly inaccurate, are orders of magnitude more computationally efficient in comparison to LES runs.

Polynomial Chaos

Under appropriate technical conditions [111, 112, 115], a random variable X can be represented as a spectral (Fourier-like) expansion in terms of orthogonal functions of a vector of standard random variables $\boldsymbol{\xi} = (\xi_1, \cdots, \xi_n)$. Truncated to a specific order, we denote the PC expansion (PCE) of X as

$$X(\xi) = \sum_{i=0}^{P} x_i \Psi_i(\xi) \tag{4.1}$$

where $\{x_i\}$ are deterministic coefficients and $\{\Psi_i\}$ are typically multivariate polynomials of $\boldsymbol{\xi}$. The polynomials Ψ_i form a complete orthogonal basis with respect to the measure on ξ. For order p, we have a total number of terms $P+1 = (n+p)!/n!p!$. Given the 3 uncertain parameters, we employ a 3-D input stochastic space ($n = 3$).

Given PCEs for uncertain model inputs, one can find the corresponding PCEs for model output

QoIs with methods that are frequently more efficient than random sampling. Aside from being a random number representation, the PCE for a QoI also serves as a surrogate model for its dependence on model parameters. We will estimate the PC coefficients for the QoIs using sparse quadrature evaluation of the PC projection integrals [116, 117, 118]. This involves evaluating the QoIs at each quadrature point, corresponding to a specific sample of the uncertain model parameters.

By construction, and for purposes of surrogate construction, we define the uncertain inputs to be independent and uniformly distributed over the ranges of interest. Further, we employ a uniform $\boldsymbol{\xi}$ with the corresponding Legendre polynomials for the $\Psi_i()$. For such a PC basis, a suitable quadrature formula is obtained by combining Smolyak's sparse tensorization method with the nested Clenshaw-Curtis quadrature formula [114]. This choice of nested quadrature is advantageous since points of a certain level quadrature are also used in higher-order quadrature.

The overall accuracy of the PCE surrogate models will be appraised using the normalized root mean squared error, NRMSE $= \|f(\boldsymbol{\xi}) - \tilde{f}(\boldsymbol{\xi})\|_2 / \|f(\boldsymbol{\xi})\|_2$, and normalized maximum absolute error, NMAE $= \|f(\boldsymbol{\xi}) - \tilde{f}(\boldsymbol{\xi})\|_\infty / \|f(\boldsymbol{\xi})\|_\infty$, where $f(\boldsymbol{\xi})$ is the LES-computed QoI and $\tilde{f}(\boldsymbol{\xi})$ is the PCE surrogate model. The norms are evaluated using m test points, which are chosen independently of the "training" points (*i.e.* quadrature points) used to obtain the surrogate models, in order to provide an unbiased estimate of the NRMSE and NMAE. We choose the test points randomly using Latin Hypercube Sampling (LHS) [119].

Test Case

The configuration selected for the present study is a turbulent bluff-body non-premixed flame for which detailed measurements of velocity and scalars are available [120, 121, 1]. The compactness, stability of the flow, and the accurately specified boundary conditions make it well-suited for error analysis.

The system is composed of a cylindrical bluff-body ($d_{bb} = 50$ mm in diameter) placed at the center of a large air flow duct ($d_{co} = 160$ mm). The fuel, a mixture of methane and hydrogen (50% in volume for each component) is injected at the center of the bluff-body through a $d_j = 3.6$ mm nozzle. The air of the external wind tunnel flows at $U_{co} = 35$ m/s when it reaches the combustor section (with a turbulent intensity of 2%) and the fuel is injected at a velocity of $U_j = 108$ m/s (assumed fully developed). The device is operated at atmospheric pressure and both fuel and oxidizer streams are injected at room temperature ($T_{co} = T_j = 298$ K). A flame is stabilized in the wake of the obstacle as shown in Fig. 4.1. The non-premixed flame is attached to the rim of the bluff-body, between the rich recirculation region downstream of the injection plate and the external air stream. The computational set-up is based on the same dimensions as in the experiment. The domain is a square-section parallelepiped ($160 \times 160 \times 200$ mm). The upstream injection section has been ignored in the computational domain. As the flame and velocity gradients are only present in the wake of the bluff-body ($r < 30$ mm, r being the radius from the fuel jet axis) the Cartesian grid spacing is constant and concentrated in this region ($\Delta_r = \Delta_x = 0.3\,mm$). The grid is smoothly stretched away from the zone of interest. The mesh is composed of 12 million hexahedral cells.

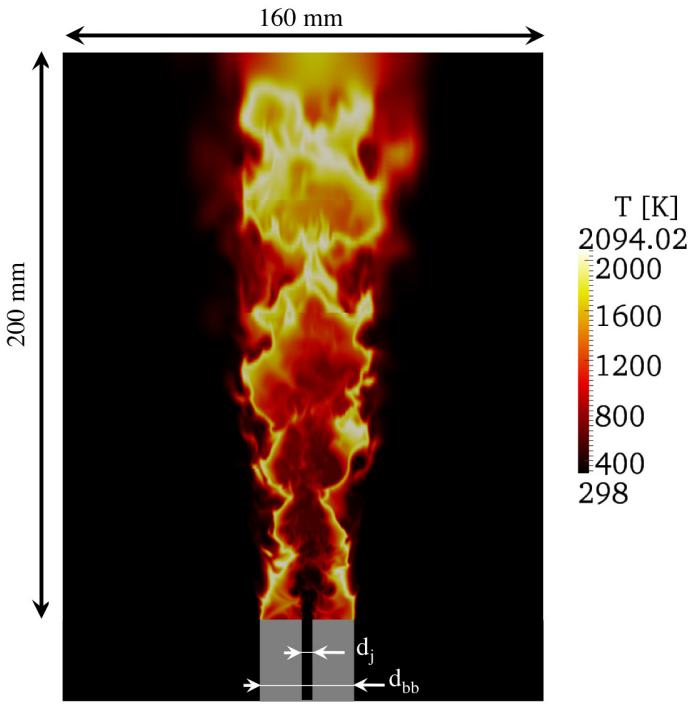

Figure 4.1. LES domain with a typical instantaneous field of temperature (median cut from LES). $d_j = 3.6\,mm$ and $d_{bb} = 50\,mm$.

At inlets, mean profiles are adjusted to match experimental measurements 1.3 mm downstream of the bluff-body. Turbulent fluctuations are added to the mean profiles using a synthetic correlated signal with the adequate intensity. Lateral surfaces are assigned far-field conditions and pressure is maintained in the domain via a relaxed outlet condition.

Generally, output uncertainties result from uncertainties in boundary conditions and initialization as well as errors resulting from discretization (both spatial and temporal) numerical integration methods. For this investigation, these aspects will not be examined as the focus is on parametric uncertainty. In the present analysis, the ranges of model parameters have been extracted from reference studies based on empirical and theoretical approaches. The Smagorinsky coefficient is varied over $0.065 < C_s < 0.346$ as suggested by Piomelli [122]. Similar ranges are considered for turbulent Prandtl and Schmidt numbers as recommended by Erlebacher *et al.* [123] and Reynolds [124]:

$0.5 < Pr_t < 1.7$ and $0.5 < Sc_t < 1.7$.

The same procedure was followed to obtain the initial LES solution for all parameter sets. The simulation is run for 0.4 s to attain steady state and flush artifacts caused by the initiation. Starting from this solution, each case is run for 30 ms to obtain converged statistics of relevance, which corresponds to a period 8 turn-over times of the recirculation zone.This duration has been found to be a good compromise between computational cost and temporal convergence of flow features. Each case is run on 1024 processors for 62 hours. Hence, the total computational requirement for generating the data for the UQ analysis (25 cases) is approximately 1.6×10^6 CPU hours.

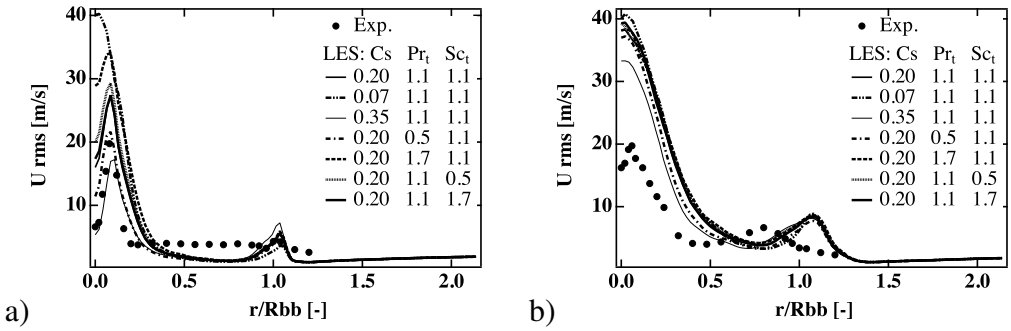

Figure 4.2. Comparison of rms of the axial velocity between LES results (lines) and experimental measurements [1] (symbols) at (a) $x = 10$ mm and (b) $x = 30$ mm downstream of the bluff-body ($R_{bb} = 25$ mm is the radius of the bluff-body).

For validation, LES results (means and fluctuations) have been compared to experimental measurements of velocities and scalars [121, 1]. A subset of profiles are presented in Fig. 4.2 showing the scatter between extreme cases of the test matrix. From Fig. 4.2 one can observe that the *rms* of the axial velocity strongly depends on the value of the Smagorinsky coefficient. This point will be confirmed and quantified in the following, along with other dependencies.

Results

We assign a joint uniform distribution to describe the uncertainty in the three parameters (C_s, Pr_t, Sc_t), with the marginal distributions being uniform over the ranges outlined earlier above. The output QoIs that will be pursued for UQ analysis are the mean and rms time-averaged temperature, axial velocity, and mixture fraction at $x = 30$ mm along the centerline downstream of the bluff-body. For this 3D stochastic problem, the quadrature method adopted, based on Smolyak's sparse tensorization method and nested Clenshaw-Curtis quadrature formula, requires 7 quadrature points for a first order PC expansion and 25 points for a second order expansion. Due to the nested nature of the quadrature method, the 7 quadrature (training) points needed for a first order representation are reused in obtaining the second order expansion.

Table 4.2. Uniform marginal probability density functions for the uncertain LES model parameters: $Cs :=$ Smagorinsky constant, $Pr_t :=$ turbulent Prandtl number, and $Sc_t :=$ turbulent Prandtl number

Parameter	Marginal distribution
Cs	$U(0.065, 0.346)$
Pr_t	$U(0.5, 1.7)$
Sc_t	$U(0.5, 1.7)$

With the available 25 training points (results from the 25 LES simulations), the coefficients of both first and second order PC surrogate models for the QoIs are obtained via Galerkin projection. 18 additional LES computations are performed to evaluate the accuracy of the surrogates. The error estimates (NRMSE and NMAE) associated with first and second-order models are listed in Table 4.3. For all 6 quantities of interest, the estimated NRMSE and NMAE are within approximately 10 and 20 percent, respectively. In principle, these can be improved by employing higher-order PC representations, with the requisite additional number of sparse-quadrature points. For some quantities, the (estimated) NRMSE is found to increase slightly when a second order model is used over a first order one. This can be attributed to the error in estimating the NRMSE and NMAE using such a small ensemble of random test points (only 18). Considering second order models only, the quantities that can be best modeled are the mean temperature and mixture fraction (with NRMSE estimates of less than 2%), while the corresponding rms quantities are least accurately modeled. The 2nd order models for the mean and rms axial velocities are of intermediate accuracy. For illustration, the response surfaces of the second order model for the mean axial velocity are shown in Fig. 4.3 along with the training (quadrature) points used and the errors associated with the surrogate model at these training points.

Table 4.3. Normalized error estimates (%) for 1st and 2nd order PCE surrogate models of quantities of interest at $x = 30$ mm centerline downstream of the bluff-body.

QoI	NRMSE (%) 1^{st}O	NMAE (%) 1^{st}O	NRMSE (%) 2^{nd}O	NMAE (%) 2^{nd}O
mean U	5.6	11	4.4	7.4
rms U	4.7	8.8	5.5	12.5
mean T	2.8	5.1	1.9	4.4
rms T	9.4	18	10.7	22.6
mean Z	1.8	3.2	1.3	2.8
rms Z	8.6	21	8.4	19.6

Using the the 2nd order PCE surrogate models, we can obtain some useful statistics for the QoIs. For example, the mean, standard deviation and coefficient of variation (the standard deviation normalized by the mean) for the six quantities examined in this investigation are obtained analytically using the available PCE coefficients and are provided in Table 4.4. The PC surrogate models also allow us to perform global sensitivity analysis analytically in order to quantify the un-

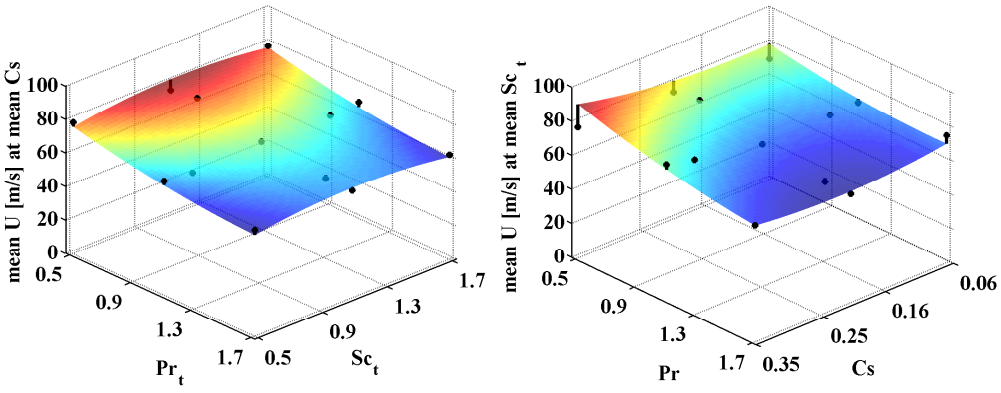

Figure 4.3. Response surfaces for mean axial velocity at $x = 30$ mm centerline downstream of the bluff-body: black dots represent the quadrature points and solid black lines highlight the errors between the surrogate model and true values from LES runs.

certainty in the QoIs due to each uncertain parameter [125]. Fig. 4.4 provides the first-order main-effect sensitivity indices, which quantify the contribution of each parameter to the total uncertainty (measured by variance) in the QoI, averaged over the other parameters. These sensitivity indices are standardized by the total variance in the QoI, and thus range between 0 and 1. Figure 4.4 shows that the fluctuation of axial velocity is strongly sensitive to the Smagorinsky coefficient. This result can be anticipated since the turbulent viscosity has a direct impact on the fluctuating flow-field contrary to the two other parameters that have indirect effects. Interestingly, the mean velocity on the centerline at $x = 30\,mm$ has a significant sensitivity to the turbulent Prandtl number. One possible explanation for this behavior is that dilatation effects, being mainly dependent on the Prandlt number, significantly impact the shape of the recirculation which in turn heavily influences the mean velocity. This coupling is still not fully understood and will require further investigation. Mean mixture fraction and temperature have similar sensitivity indices. This is a consequence of the presumed combustion model which heavily correlates mixture fraction with the energy source term. Variability in the mean mixture fraction has a stronger dependence on the variability in C_s. This may be due to the mixture fraction being predominantly affected by the "resolved" turbulent mixing that depends on resolved velocity fluctuations which are more sensitive to the Smagorinsky coefficient. Sensitivity indices for the fluctuations in temperature and mixture fraction are of comparable magnitudes for the three uncertain parameters. This indicates that the accuracy in the prediction of these quantities relies equally on accurate estimates of the three parameters. It is important to note that the present analysis is isolated to the flow response at a single physical point. The current work is not aimed at describing the global behavior of the QoIs. The focus is to demonstrate the ability of available UQ tools in providing valuable information pertaining to LES of turbulent reacting flow. A more thorough physical interpretation of these results is of importance and will be investigated in future work.

Assuming a jointly uniform density over the three uncertain parameters, the marginal and 2D

Table 4.4. Statistical moments of the quantities of interest at $x =$ 30 mm centerline downstream of the bluff-body using the second order PC surrogates.

QoI	Mean value	standard deviation	coefficient of variation (%)
mean U	70.9	5.27	7.43
rms U	38.6	3.70	9.59
mean T	479	54.8	11.4
rms T	90.3	12.2	13.5
mean Z	0.809	0.0620	7.66
rms Z	0.0980	0.0106	10.8

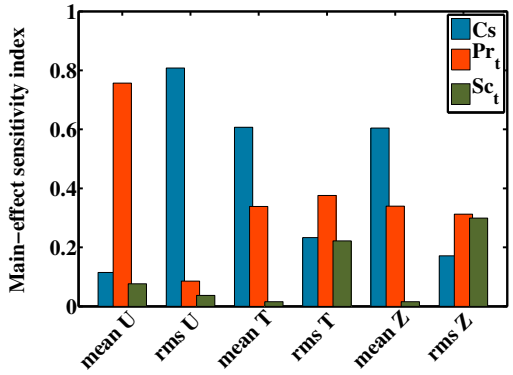

Figure 4.4. Main-effect sensitivity indices for mean and rms axial velocity (U), temperature (T), and mixture fraction (Z) at $x = 30$ mm centerline downstream of the bluff-body.

joint PDFs can be obtained by Monte Carlo sampling of the PC surrogate models. A total of 60×10^6 realizations of the QoIs are obtained from which normalized histograms are obtained as estimates of the 1D and 2D marginal PDFs as shown in Fig. 4.5 and Fig. 4.6, respectively. The 1D PDFs contain some dominant discontinuities in their derivatives. This is expected given a Legendre-Uniform PC surrogate model of relative low dimension and low order (weakly nonlinear response surface). The 2D marginal PDFs in Fig. 4.6 demonstrate some strong correlations and nonlinear relationships between the QoIs examined.

Fig. 4.6 presents some interesting coupled behavior between the QoIs. Mean temperature and velocity exhibit a strongly negative correlation for $U_{mean} < 80\,m/s$. At the probe location being examined, the axial velocity strongly depends on the velocity of the fuel jet, a quantity highly impacted by turbulent mixing. When the level of turbulent mixing is increased (due to changes in the uncertain parameters), the mean axial velocity decreases while the mean temperature increases, resulting in the observed negative correlation. This observation is supported by the 2D joint pdf of temperature fluctuation and mean axial velocity (Fig. 4.6b): for $T_{rms} > 60\,K$, the decrease of

the mean axial velocity is associated with an increase of turbulent mixing which is reflected by the increase of temperature fluctuation.

In Fig. 4.6a, the increase of mean temperature for $U_{mean} > 85\,m/s$ is a consequence of the presence of the flame. At those conditions, the flame gets closer to the centerline, inducing an acceleration of the flow and an increase of the mean temperature. This explains the positive correlation observed in Fig. 4.6a for $U_{mean} > 85\,m/s$. Similarly, one can observe a strong negative correlation between T_{rms} and U_{mean} in Fig. 4.6b. For $T_{rms} < 60\,K$, the flame is closer to the central axis leading to an increase in viscosity (due to higher temperatures) and an attenuation of temperature fluctuations. The strong positive correlation between mixture fraction and temperature fluctuations observed in Fig. 4.6c is a direct consequence of the modeling approach for the combustion closure.

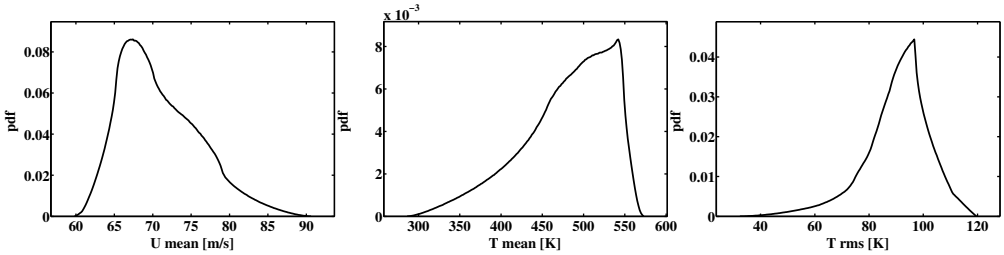

Figure 4.5. Selected 1D marginal pdfs of the QoIs at $x = 30$ mm centerline downstream of the bluff-body.

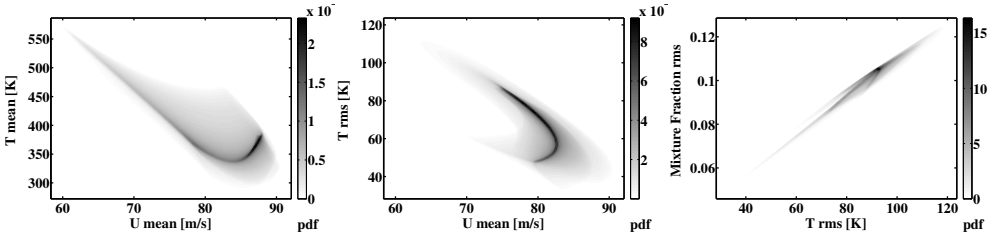

Figure 4.6. Selected 2D marginal pdfs of the QoIs at $x = 30$ mm centerline downstream of the bluff-body.

The observed sensitivity indices, and output correlations, clearly provide a significant amount of information on the dependence of each of the chosen QoIs on the model parameters, as well as the coupling among QoIs induced by the model. Thus, the present UQ results, aside from providing a surrogate for the dependence of the QoIs on model parameters, are quite informative on model structure and its dependence on the uncertain parameters chosen. These findings showcase the superior computational efficiency of polynomial chaos UQ methods in comparison to Monte Carlo UQ methods, with the later requiring a significantly larger number of costly LES runs to obtain such sensitivity indices and PDFs with similar accuracy. These results will be extended in future

work to provide further improvements in accuracy, and to examine other flow/flame observables of interest.

Conclusions on Advanced UQ methods for model error analysis

We presented uncertainty quantification results for large-eddy simulation of a turbulent non-premixed hydrocarbon flame stabilized on a bluff-body. More specifically, parametric uncertainty in the Smagorinsky coefficient and the turbulent Prandtl and Schmidt numbers was propagated through the LES computations in order to construct a polynomial chaos based surrogate model for the quantities of interest (QoIs) in terms of the uncertain parameters.Non-intrusive forward polynomial chaos methods based on Galerkin projection with sparse-quadrature are exploited in obtaining the polynomial chaos coefficients of the surrogate models. The accuracy of the surrogate models is examined using global error measures. The computationally inexpensive surrogate models are explored using random sampling to obtain marginal joint distributions of the quantities of interest. The surrogates are also used to perform a global sensitivity study between various quantities of interest and the three LES parameters. The resulting probability densities and sensitivity indices provide insight into the mechanics of the LES solver used herein. As a next step, these surrogate models will be used as computationally efficient alternatives to performing computationally-intensive LES for prediction of the chosen QoIs over the support of the parameter PDFs. This enables subsequent statistical inference to establish posterior probability densities on these parameters given experimental data.The surrogate models will provide both insights and quantitative way to calibrate and optimize the subgrid-scale closure.

Chapter 5

Advanced Uncertainty Quantification for model development

Introduction

In this Chapter we use the UQ methods presented earlier to develop optimized chemistry model to predict the complex ignition processes in Diesel engines. The objective is to design a simple chemistry mechanism of a few reactions (<10) and a few species (<10) to ensure affordability while providing accurate results in terms of auto-ignition in a well-known experiment of the engine community (namely the SprayA case from ECN). Fuel injection processes in internal-combustion engines largely determine fuel-air mixture formation, which governs the detailed evolution of chemical kinetics, combustion, and emissions. Lack of accurate models is a major barrier toward the design of optimized, clean, high-efficiency engines and there is a critical need for advanced development in this area [126]. Addressing this need involves a variety of challenges, which include all of the complications associated with turbulent combustion in gas phase systems, plus significant additional complications that arise due to the presence of multiple phases. Multi-scale coupling between processes occurs over a wide range of time and length scales, many being smaller than what can be resolved in a numerically feasible manner. Further complications arise when liquid phases are present due to the introduction of dynamically evolving interface boundaries and the complex exchange processes that occur as a consequence. At the device level, high-performance, dynamic stability, low pollutant emissions, and low soot formation must be achieved simultaneously in complex geometries that generate complex flow and acoustic patterns. Flow and combustion processes are highly turbulent; i.e., integral-scale Reynolds numbers of $\mathcal{O}(10^5)$ or greater, and the turbulence dynamics are inherently dominated by geometry or various operating transients. In modern systems, operating pressures now approach or exceed the thermodynamic critical pressures of the working fluids. This introduces significant thermodynamic non-idealities and transport anomalies in low-temperature regions. Elevated pressures also significantly increase the system Reynolds number(s), which inherently broadens the range of spatial and temporal scales that interactions occur over.

Recent works [127, 128, 129, 130, 131, 132] have focused on the complex thermodynamic behavior of the liquid-gas interface across a large range of conditions relevant for automotive applications. When operating pressures exceed the critical pressure of the injected fuel, the interfacial diffusion layers can develop due to thickening of the gas-liquid interfaces combined with a

significant reduction in the mean free molecular path and surface tension forces. These interfaces eventually enter the continuum length scale regime and disappear as interfacial fluid temperatures rise above the critical temperature of the local mixture. The lack of inter-molecular forces, coupled with broadening interfaces, promote diffusion dominated mixing processes prior to atomization. As a consequence, injected jets evolve in the presence of exceedingly large but continuous thermo-physical gradients in a manner markedly different from classical assumptions. Detailed LES simulations have been used to determine the state of the mixture that leads to ignition in the Spray-A configuration. This work was performed to identify the envelopes of pressure, temperature and equivalence ratio over which the reduced chemistry has to be accurate.

Based on those results, different chemical mechanisms have been designed using a Bayesian inference method. The main inference objective is to correctly capture the auto-ignition delay time which is curtail for emission and engine performances. The main difficulty is that for the present conditions and fuel, the ignition first goes through a cool-flame reaction period before running away. This aspect is well known in diesel combustion but represents a significant challenge in the development of affordable kinetics.

In the following, a summary of the non-reacting LES is first presented to establish the local flammability characteristics of the flow (Temperature, Pressure and mixture composition) just before autoignition. Then experimental results are used to define what are the most important chemical processes to capture with the kinetic mechanism. In a third section, the Bayesian inference method is presented along with a description of the different steps taken to design the reduce chemistry. Results are provided at the en showing the benefits of the approach.

Experiment and ranges of conditions extracted from non-reacting LES simulations

We use the experimental data of the "Spray-A" case (n-dodecane), provided by several groups from the Engine Combustion Network (see www.sandia.gov/ECN [133]). A photography of the rig is shown in Fig. 5.1. This experiment has been designed to investigate ignition sequences of diesel spray under very controlled conditions of pressure, temperature and mixture composition. Pressure and temperature conditions are established by a pre-brun phase during which the ambient (flammable) mixture is ignited to reproduce engine conditions. In the present case, liquid n-dodecane at 363 K is injected through a 0.09 mm diameter automotive injector nozzle into a gaseous mixture at 900 K and 60 bar. The peak injection velocity is 620 m/s. The conditions in the ambient gas are presented in Tab. 5.1.

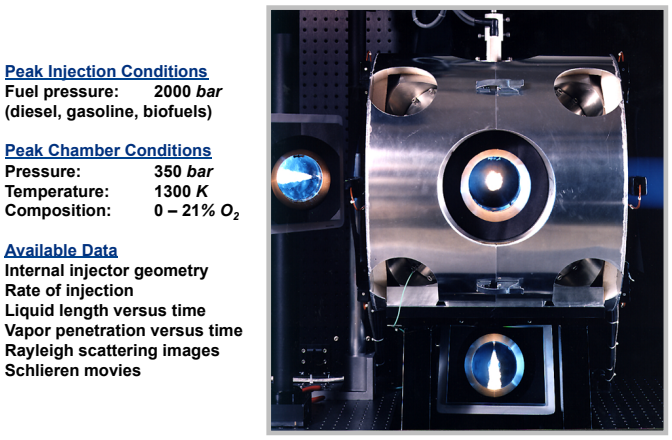

Figure 5.1. Photograph of the Sandia high-pressure combustion vessel.

T_0 [K]	900
p_0 [MPa]	6
X_{O_2} [%]	15.00
X_{N_2} [%]	75.15
X_{CO_2} [%]	6.23
X_{H_2O} [%]	3.62
T_i [K]	373

Table 5.1. Operating conditions in the Spray A case. X_i are the mole fractions in the ambient gas before injection, and p_0 and T_0 are the mean pressure and mean temperature, respectively. T_i is the injection temperature of the fuel.

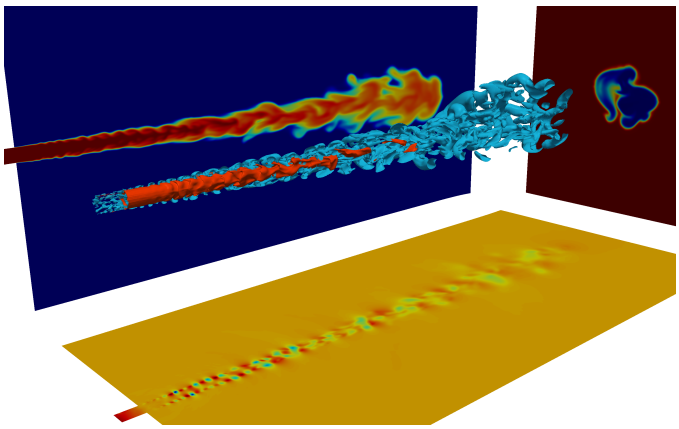

Figure 5.2. Three dimensional rendering of the fuel injection process at $t = 45\ \mu s$. The red iso-surface marks where $\rho = 200\ kg/m^3$, the blue iso-surface marks a Q-criterion threshold that localizes the most coherent turbulent structures, the bottom cutting plane shows the pressure across the jet, the back-right plane shows the temperature from 363 K in blue to 900 K in red, and the back-left plane shows the fuel mass fraction.

LES is performed using the real-fluid model described below. Results are then analyzed from the perspective of real-fluid thermodynamics with emphasis on the state of the transient mixing field prior to auto-ignition. In previous studies we focused exclusively on transient mixing of the Spray-A case just prior to autoignition through a series of highly resolved LES calculations [130, 131]. Detailed analysis revealed the instantaneous three-dimensional structure of the injected jet along with the instantaneous pressure and scalar dissipation fields. Also shown were the corresponding mixture fraction, temperature, density, Mach number, and speed of sound distributions. The "gas-like" behavior of the fuel jet was observed along with self-similar behavior, which is a feature of classical gaseous turbulent jets. Strong density variations resulted from the high-momentum flux ratio, which delayed the destabilization of the jet. Once the destabilization of the dense core occurred, parcels of dense fluid detached from the compressed liquid jet. The presence of these fast-moving dense structures enhanced local turbulence. Those processes have a profound impact on mixing.

In the following we only focus on data extracted from the detailed LES (see Fig. 5.2) that have an impact on auto-ignition which are not attainable by experimental diagnostics.

To investigate the mixture conditions relevant for auto-ignition, one can identify regions where the first flame kernel has the highest probability to occur. The approach, proposed by Lacaze et al. [131], maps the ignition delay time given by a set of Perfectly Stirred Reactor (PSR) calculations using the envelope of mixture states extracted from the LES. This provides the region in space where the probability of ignition is the highest. Using this analysis, the conditions relevant

for ignition have been quantified. These ranges are shown in Fig. 5.3, which presents contours of equivalence ratio, temperature, pressure, and compressibility factor in the regions where ignition is likely to occur. Within these regions, the equivalence ratio varies from 0.5 to 4.0 and temperature varies from 700 K to 900 K. Pressure varies the least and is therefore assumed to be constant (60 *bar*). In addition, Fig. 5.3 (d) shows that the mixture is very close to an ideal gas in the flammable region. Thus, real-fluid thermodynamics and transport can be ignored in the development and optimization of the simple chemical mechanism. It is however important to note that the instantaneous mixing field prior to these flammable regions is dominated by these real-fluid phenomena.

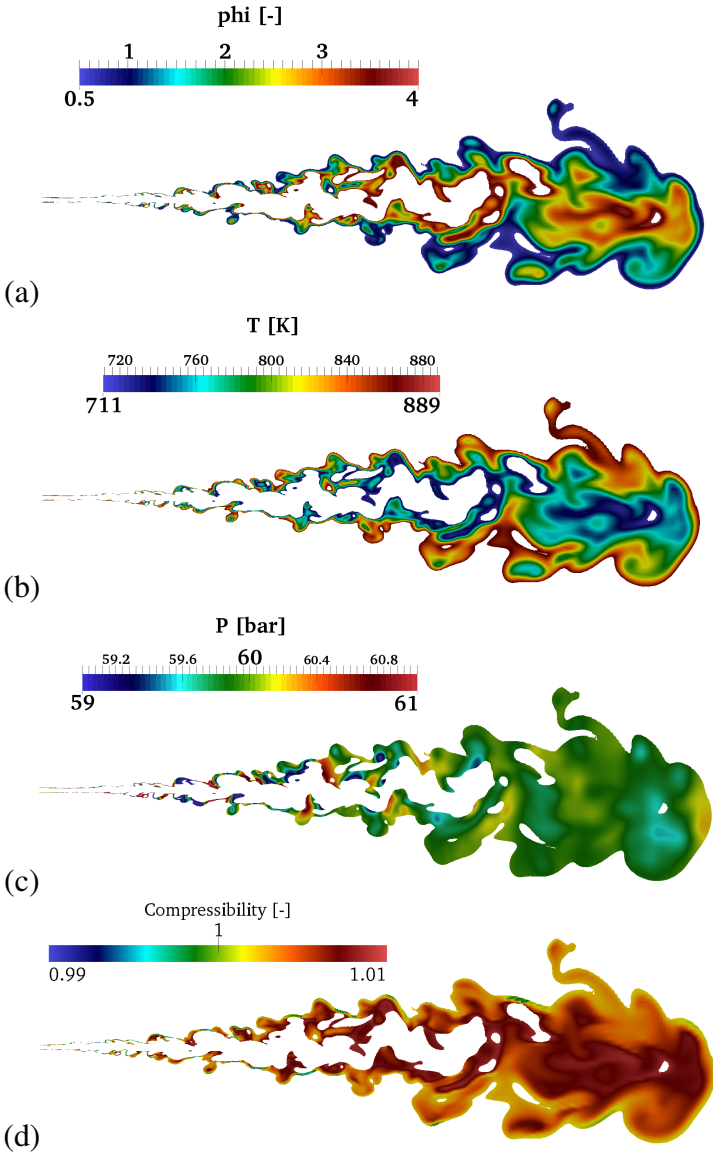

Figure 5.3. Scalar fields showing the ranges of relevant quantities in the most flammable region at $t = 260\ \mu s$ just before ignition.

Important chemical characteristic to capture

Experimental visualizations from Skeen et al. [2] have been used to identify the important chemical characteristics of the Spray-A case ignition. These characteristics are illustrated in Fig. 5.4 a), which shows a two stage ignition process under the present conditions. At $t = 260\ \mu s$, a well-mixed region is created at the tip of the fuel jet. At $t = 314\ \mu s$, first-stage (or cool-flame) ignition occurs, which annihilates the Schlieren effect initially caused by the cold fuel jet. Main ignition occurs 60 μs later and is detected on the Schlieren images as the temperature of the gas becomes much higher than the ambient. This behavior is also shown analytically in Fig. 5.4 b), where the temporal evolution of the temperature in a zero-dimensional ignition calculation is presented. This calculation is based on the chemical scheme by Luo et al. [3] at conditions relevant for Spray-A (i.e., a mixture of n-dodecane in air with $p = 60\ bar$, $\phi = 1$ and $T = 820\ K$). The chemical characteristics that need to be captured are then 1) the cool-flame behavior, 2) the main ignition delay time, 3) the flame speed associated with partially premixed combustion once the flame is generated, and 4) the correct burnt gas temperature for relevant ranges of mixture conditions.

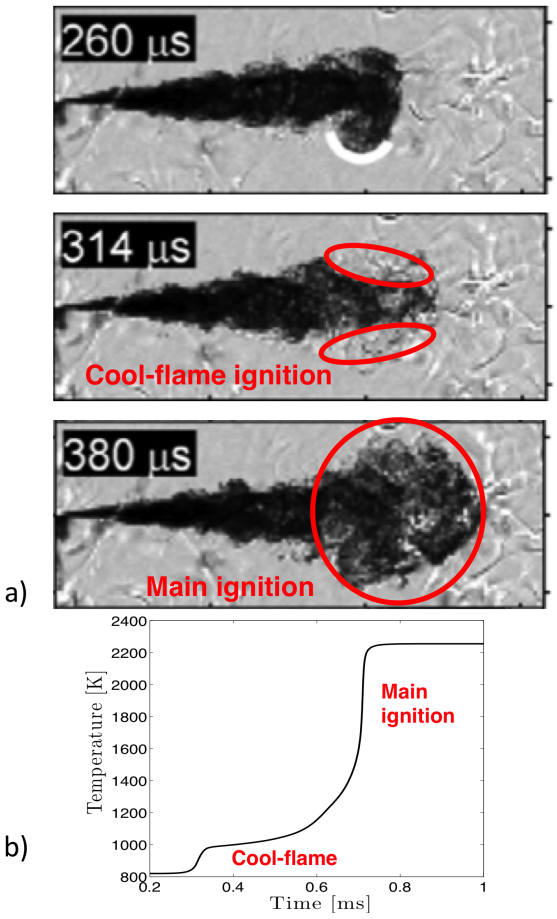

Figure 5.4. a) Two-stage ignition can be observed in the Schlieren images from Skeen et al. [2]. At $t = 260\ \mu s$ the n-dodecane jet produces a clear Schlieren effect due to its cold temperature (363 K) compared to the ambient (900 K). At $t = 314\ \mu s$ the Schlieren disappears due to the small temperature increase caused by the first stage of the ignition. At $t = 380\ \mu s$ the main ignition is clearly observable as the temperature in the reactive region is above 2000 K. b) Time evolution of the temperature in a Perfectly Stirred Reactor computation using the skeletal chemical scheme by Luo et al. [3] (105 species) at conditions relevant for Spray-A (i.e., a mixture of n-dodecane in air, $p = 60\ bar$, $\phi = 1$ and $T = 820\ K$).

Advanced UQ to design chemistry model

In the context of chemistry models for CFD simulation one interesting aspect is that large uncertainties exist in complex chemical mechanisms and their operational ranges of accuracy can be limited. Mechanisms for n-dodecane, for example, have yet to be developed and validated at pressures higher than 50 *bar*. Thus, using a complex chemical mechanism for cases such as Spray-A at 60 *bar* is not necessarily any better than a less expensive but optimized simple mechanism.

In this section we outline the framework used to design the simple chemical mechanisms. The emphasis is placed on the affordability of the kinetics and their capability in predicting autoignition with the presence of a cool-flame. Here a unique approach based on Bayesian inference [134, 135, 136, 16] is employed to design simple chemical schemes. The advantage of this approach is that it provides not only optimal parameter estimates but also the error bars on the model predictions. Bayesian inference methods are based on Bayes rules that reads as in Fig. 5.5.

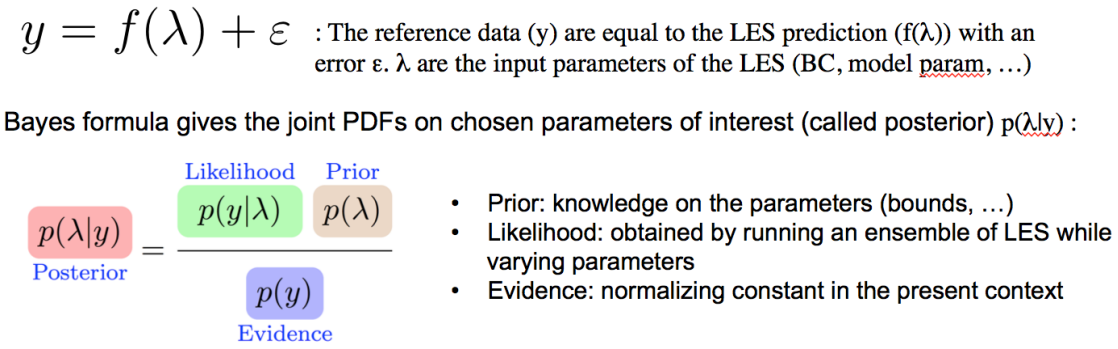

Figure 5.5. Bayes rule and principle.

The first step in the development of the chemical model was focused on getting accurate predictions of the main ignition over the full envelope of conditions encountered in the Spray-A case. Previous studies have shown that a reduced mechanism is sufficient to predict the main features of combustion processes over a wide range of temperatures, equivalence ratios, and pressures provided that the Arrhenius rate parameters are well adjusted and allowed to vary with the local conditions [137, 138, 139, 140]. It was shown in [140], for example, that a simple two-step mechanism can handle both autoignition and flame propagation by taking advantage of the fact that these processes occur over two different ranges of temperatures. Based on the results of [140], our first goal is to capture the autoignition delay time by modifying the classical two-step mechanism from Westbrook et al. [141]. This mechanism accounts for the incomplete oxidation of the n-dodecane using the following rate equations

$$C_{12}H_{26} + \frac{25}{2}O_2 \rightarrow 12CO + 13H_2O \tag{5.1}$$

$$CO + \frac{1}{2}O_2 = CO_2 \tag{5.2}$$

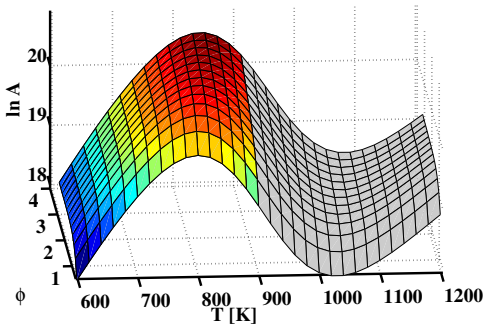

Figure 5.6. Surface of the logarithm of the pre-exponential factor versus the initial temperature T_0 and ϕ estimated using Bayesian inference using the skeletal mechanism by [3] as a reference. The colored region corresponds to parametric ranges of interest in the present study.

The corresponding reaction rates are modeled using Arrhenius laws, with key parameters taken from [142, 141] (units are *cm*, *s*, *mol*, *cal*)

$$k_1 = Ae^{\left(-\frac{E_a}{RT}\right)}[C_{12}H_{26}]^{0.25}[O_2]^{1.25} \tag{5.3}$$

$$k_{2f} = 3.98 \times 10^{14} e^{\left(-\frac{40}{RT}\right)}[CO][H_2O]^{0.5}[O_2]^{0.25} \tag{5.4}$$

$$k_{2b} = 5 \times 10^{8} e^{\left(-\frac{40}{RT}\right)}[CO_2] \tag{5.5}$$

In these expressions, R is the ideal gas constant, T is the temperature, and $[X]$ the molar concentration of species X. The term k_1 is the reaction rate of the fuel oxidation. Rates k_{2f} and k_{2b} are the forward and backward reactions in Eq. 5.2. Here, the activation energy E_a and the pre-exponential factor A are calibrated to obtain accurate autoignition delay times.

To our knowledge, there is no detailed experimental data giving the autoignition delay time of n-dodecane in air at the operating conditions of interest (pressures above 50 *bar*). Consequently, we use the skeletal chemical mechanism developed by Luo et al. [3], which uses 105 species and 420 reactions. This mechanism is preferred over a detailed mechanism for computational cost reasons and is used to generate the reference data for the statistical calibration. The approach is based on the following sequence. First, the reference data set (composed of quantities of interest such as the autoignition delay time) is built over the range of conditions of interest, which here are the equivalence ratio and temperature. Second, parameters in the chemical mechanism that we want to optimize are set as independent variables. Bayesian inference then provides the probability density function of each independent chemical variable at each point of the condition space. Surfaces of the optima can then be retrieved, such as the one presented in Fig. 5.6.

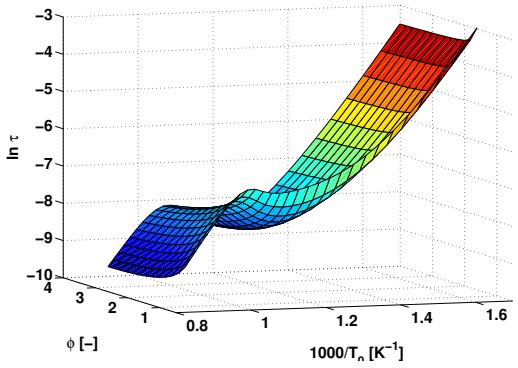

Figure 5.7. Autoignition delay time versus the initial temperature T_0 and the equivalence ratio ϕ calculated using the skeletal mechanism by [3].

The autoignition delay time calculated using the reference mechanism of Luo et al. [3] is plotted in Fig. 5.7. One can identify a negative temperature coefficient region characteristic of cool flame behavior. In the present context, the two chemical parameters that impact the auto-ignition delay time of the kinetic mechanism are A the pre-exponential factor and E_a the activation energy of the first reaction.

Bayesian inference indicates that E_a and A are tightly coupled by a linear relationship as presented in Fig. 5.8. This implies that it is possible to keep E_a constant in the $T-\phi$ plane and control the behavior of the scheme by parametrizing A.

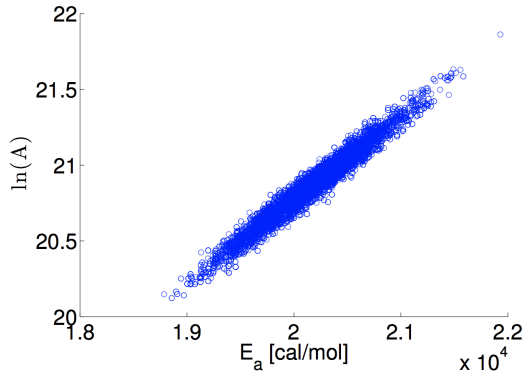

Figure 5.8. Correlation between A and E_a in the present system.

Using this approach, Bayesian inference provides an estimate of the optimal value of $E_a =$

17.8×10^3 cal/mol. Then, the optimal surface for A for ignition delay time is given by the mechanism by Luo et al. [3]. Fig. 5.6 shows the surface of lnA in the $T - \phi$ space. In this figure, the colored area represents the lnA surface in the temperature range of interest. The rest of the surface is shown to illustrate the non-linear character of lnA if considered over a wider range.

At this point, two options are available to correctly capture the ignition delay time with the two-step mechanism, either a tabulation of A in $T - \phi$ space, or an approximation of the surface by an analytical function. Here we chose to develop an analytical expression of the surface of Fig. 5.6. In order to design a generic model that can be used by a broad community with specific different simulation tools and strategies, we chose to fit the surface shown in Fig. 5.6 using functions of increasing accuracy. The first three set of functions are coming from the UQ field and are based on Legendre Polynomials. The last set comes from the practical solutions designed by Misdariis [140] and Franzelli [139] and is based on empirical hyperbolic tangential functions.

1st order expansion of $\ln(A)$

For this first function set, A or more precisely $\ln(A)$ is a linear combination of T_0 the initial temperature and ϕ the equivalence ratio:

$$\begin{aligned} E_a &= \eta_0, \\ \ln(A) &= \lambda_0 + \lambda_1 * T_0 + \lambda_2 * \phi \end{aligned} \tag{5.6}$$

We run an Adaptative Markov Chain Monte Carlo (MCMC). MCMC methods are a class of algorithms for sampling from a probability distribution based on constructing a Markov Chain that has the desired asymptotic distribution. The state of the chain after a number of steps is then used as a sample of the desired distribution. The quality of the sample improves as a function of the number of steps. The MCMC method is used to approximate a multi-dimensional integral using an ensemble of "walkers" that move semi-randomly. The walkers do not spend too much time in low-probability regions but will "wander" longer in high-probability areas. An example of the marching progress of the method is shown in Fig. 5.9 for the case presented in Eq. 5.6. The joint PDFs of the parameters of Eq. 5.6 are presented in Fig 5.10.

The performance of the 1st order model is then tested against the reference kinetic mechanism of Luo in Fig. 5.11. One can observe that the error produced by the 1st order model goes up to 40% in the range of initial temperature and equivalence ratio of interest. Tests of the second order show that the error is decreased (and gives a maximum of 20%) as the degree of freedom of the model increases. Those results are not shown to limit the size of the present report. More interesting results are however obtained with an optimized fit of the surface presented in Fig. 5.7.

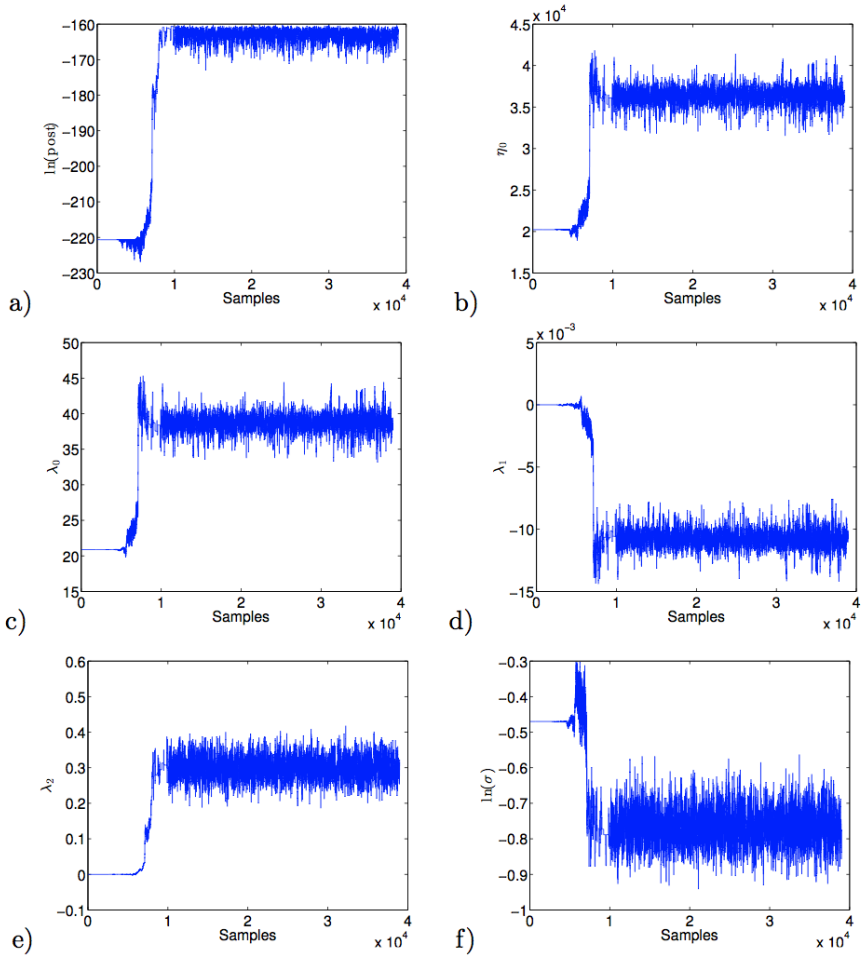

Figure 5.9. Chain of the 1st order expansion defined in Eq. 5.6.

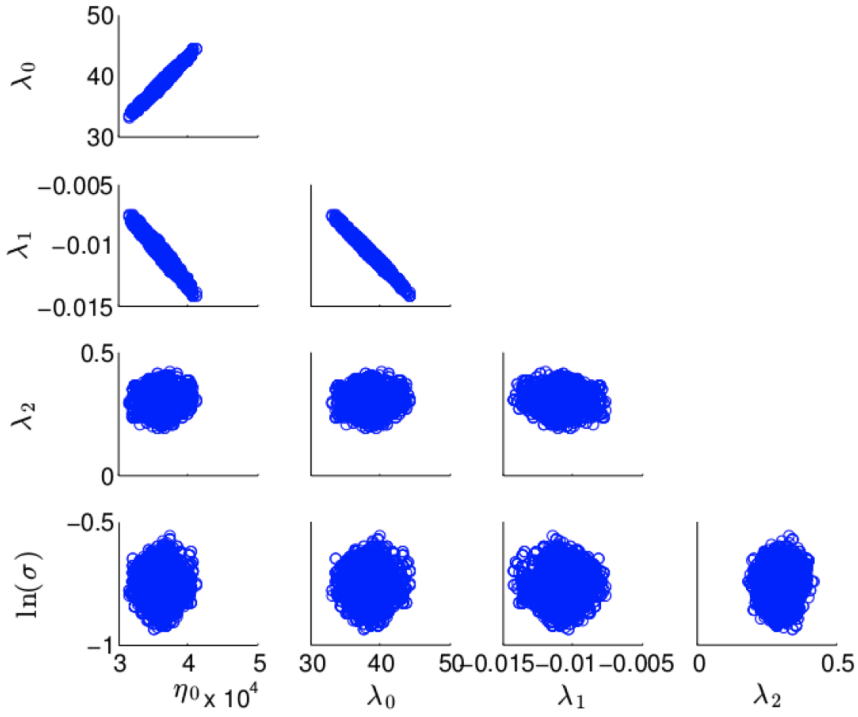

Figure 5.10. Result of the method for the 1st order expansion defined in Eq. 5.6.

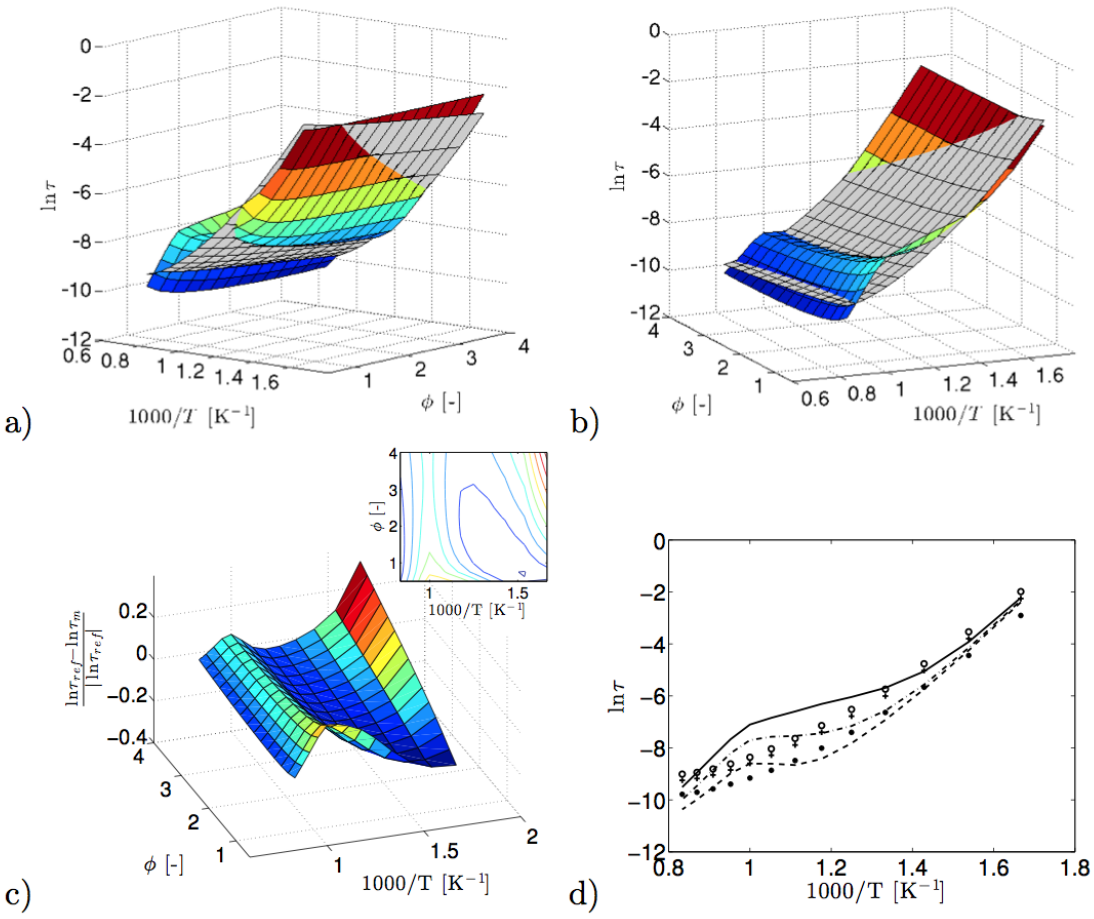

Figure 5.11. Autoignition delay time - (a-b) Comparison between the reference data (colored surface) and the simple model data (gray surface). (c) Relative error of the model with respect to the reference data. (d) Comparison between the reference data (lines) and the simple model data (symbols) for three different equivalence ratios: (— and o) $\phi = 0.5$, (-·- and +) $\phi = 1$, (- - - and •) $\phi = 3$.

a_1	$-1.1813\,10^{1}$
a_2	$-2.0593\,10^{2}$
a_3	$-1.0701\,10^{1}$
a_4	$9.0240\,10^{-1}$
a_5	$-7.4711\,10^{-3}$
a_6	$1.3826\,10^{-3}$
a_7	$5.4015\,10^{0}$
a_8	$7.5159\,10^{-2}$
a_9	$-4.4904\,10^{-5}$

Table 5.2. Parameters of the function given in Eq. 5.8.

Inference of an informed fit for $\ln(A)$

This approach is similar to the one followed by Misdariis [140] and Franzelli [139], where a fit function is elaborated for $\ln A$ in $T-\phi$ space, see Eq. 5.8.

$$E_a = \eta_0, \tag{5.7}$$

$$\ln A = a_1 + a_2 e^{a_3\phi} + a_4 \tanh((a_5 + a_6\phi)T_0 + a_7) + a_8 T_0 + a_9 T_0^2. \tag{5.8}$$

The corresponding parameters are shown in Table 5.2. Figure 5.12 provides verification of the performance of the two-step mechanism for predicting the autoignition delay time and flame temperature compared to the reference chemical mechanism given by Luo et al. [3]. Figure 5.12a) shows that the reduced optimized scheme is able to capture ignition delay with good accuracy over the range of conditions of interest. Figure 5.12b) shows the relative error $\varepsilon = (\tau_{Luo} - \tau_{2step})/\tau_{Luo}$ on ignition delay time. The maximum error is 13 percent.

Summary

In this work we have extended detailed cold-flow studies performed previously using the Large Eddy Simulation (LES) technique to reacting flow cases using the Engine Combustion Network (www.sandia.gov/ECN) Spray-A injector with n-dodecane as the fuel. Simulations are performed by identically matching the operating conditions used in the experiments. At these conditions recent theoretical studies have shown that real-fluid effects are dominant. Thus, sophisticated real-fluid thermodynamics and transport must be included. Based on these new insights, a series

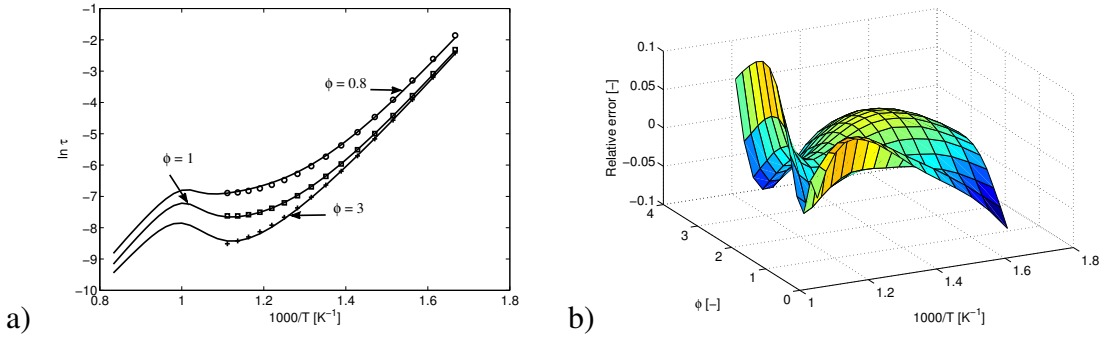

Figure 5.12. a) Comparison of the autoignition delay time provided by the current two-step mechanism (symbols) with the reference mechanism of Luo et al. [3] (lines) for three different equivalence ratios. b) Relative error $\varepsilon = (\tau_{Luo} - \tau_{2step})/\tau_{Luo}$ on the ignition delay time provided by the present two-step mechanism. The maximum error is 13 percent.

of highly resolved calculations are performed that treat real-fluid multiphase thermodynamics and transport applicable to the high-pressure phenomena observed in the experiments. Non-reacting results showed very good agreement with experimental measurements and observations lending confidence in the approach. This framework is then combined with a novel combustion closure using a set of simple but optimized chemical mechanisms that efficiently capture turbulence-chemistry interactions and cool/hot flame ignition with equal levels of fidelity. An initial two-step chemical mechanism was designed that predicts the autoignition delay time and the flame propagation over ranges of temperature and equivalence ratio relevant to the Spray-A case. These ranges were quantified using high-resolution LES results that show the transient mixing state of the injected jet just prior to autoignition.

Design of the optimized chemical mechanism is achieved using Bayesian inference, which quantifies the optimal values of the model parameters together with the associated uncertainties. Results highlight the combined effects of turbulent scalar-mixing and turbulence-chemistry interactions on ignition in these flows. In addition, it is shown that simple chemical mechanisms, if optimized over a relevant envelope of temperatures, pressures, and equivalence ratios using advanced Uncertainty Quantification techniques, can accurately reproduce the complex ignition behavior of Diesel-like fuels with significantly reduced computational cost.

The present approach has potential to offer some useful advantages. First, the additional computational cost is very small compared to a non-reacting case as only three addition transport equations are required. This can provide a significant advantage in terms of the computational resources required to correctly capture turbulent scalar-mixing processes, which are critically important input to the chemical model. Scalar-mixing is the primary input to the chemical mechanism. If this

input is inaccurate, there is no way for any chemical mechanism to produce the correct results.

Using skeletal mechanisms with on the order of 100 species increases the computational requirement by a factor 20 or 30. In many cases, CFD practitioners handle this added expense by significantly reducing the spatial resolution of the computational domain, which in turn leads to a dramatic deterioration of the mixing prediction. The current work aims to find an optimal balance in requirements between the coupled system of turbulence and chemical models. As the present approach is based on an Arrhenius formulation, its implementation in most research and design codes is greatly facilitated as well as its interface with any turbulent combustion closure. In future work, the uncertainties on the input parameters will be propagated through the LES to gain insights into the uncertainty on the simulation results.

Chapter 6

Conclusion

The development of advanced transportation, propulsion, and power systems requires an in depth understanding of the complex turbulence and reacting flow processes involved. Large-eddy-simulation (LES) is a well known method of choice for studying complex thermo-physics in a wide range of propulsion and power systems. It provides a means to study coupled turbulent combustion and flow mechanisms in parameter spaces that are unattainable using direct-numerical-simulation (DNS), with a degree of fidelity that can be far more accurate than conventional engineering methods such as the Reynolds- averaged Navier-Stokes (RANS) approximation. However, development of predictive LES is complicated by the interdependence of different subgrid-scale models, competition between modeling and numerical errors, model variability, and numerical implementation. Errors and ambiguities are multiplying, and control of accuracy has become a critical aspect in the development of predictive LES for design. Because of the lack of a formal approach, it is generally accepted that in a typical simulation cycle, only 20% of the computational time is actually usable. The rest is spent in case preparation, assessment, and validation. When accuracy is not sufficient, results can be misleading and intractably erroneous due to factors such as poor numerics, poor grid quality, under-resolution in space and time, ill-posed boundary conditions, and inaccurate models.

This project was aimed at quantifying the quality and accuracy of state-of-the-art LES in a manner that addresses the complex interdependencies between errors. The approach facilitates control of the tradeoffs between cost, accuracy, and uncertainties as a function of fidelity, models, and numerical methods employed. This work was organized around three main goals: (1) Create new metrics to assess simulation quality and enhance our predictive capabilities, (2) Provide better fundamental insights in combustion science and (3) Develop advanced models at conditions relevant for industry.

The first point has been addressed by carefully assessing existing methods. Current methods were identified as not reliable enough and it has been concluded that a set of clear metrics were required to measure quality of our simulations. Two types of metrics have been tested: (a) Statistically converged flow quantities, such as mean and rms of scalars and momentum. (b) Local and spatial spectra of power density of turbulent quantities. Those metrics must be used in the context of parametric studies on grid spacing. The required quality for our simulations is reached when those metrics stop evolving while the computational grid is further refine. At this point we maximize the accuracy of the LES while limiting the computational cost. Those metrics have been tested in many different configurations from two-dimensional mixing layer to full three-dimensional jet

in cross flow. They have been proven to be very good criteria to assess grid convergence and are powerful indicators of when numerical and models errors decouple. The advantage of the metrics based on converged turbulent moments is that they can be compared directly with experimental measurements. They are then necessary in a validation context.The spectral metrics however contain more information concerning the local turbulent mechanisms and can be used to detect abnormal flow behavior due to contamination of the numerical framework or limitation in models. The spectral metrics can be used to indicate if statistics are predicted for the right reasons or not. Even though those parameters seems trivial, they have to be used in a proper way and the present project provides guidance on the method. This approach is now systematically employed for each of our simulations and have helped identifying optimal griding strategies to maximize accuracy while keeping simulation costs at affordable levels.

The second point is a direct consequence of the previous one. In all configurations studied, the use of the metrics has led to validated numerical accuracies at a level that revealed new fundamental physics. In the jet in cross flow study, the quality of the LES allowed us to described in detail the different turbulent topological structures present in the flow. The analysis provided a comprehensive description of their evolution and interaction and their role in mixing. Various turbulent scales have been mapped (integral scales, Taylor-micro scales, turbulent spectra) and a similar spatial evolution has been observed: scales grow near-linearly before turbulent breakdown of the jet, then a '1/3' power law is observed, consistently with a wake scaling. This information is of prime importance for engineering as it provides guidelines to properly design a LES grid. This shows that a linear stretching of the mesh from injection point to the far-field would be too dissipative and might impact the far-field predictions of turbulent mixing by filtering out key turbulent structures present in the wake of the jet. For this reason, we recommend keeping a stretch rate smaller than $y/d^{1/3}$ to follow the growth rate of the integral scale along the jet centerline and in its wake. Smaller cells, however, should be placed at the outer edge of the jet to capture the interaction between the jet and the cross-flow. This part of the work has improved our understanding of the fluid mechanics in such flows. We envision that industry will benefit from the detailed topological description of the turbulence generated by a jet-in-cross-flow to optimize mixing in applications where such configuration is present. This is for example the case in gas-turbines for aircraft propulsion or power generation.

The third aspect is model assessment and model development. Models in LES are based on specific assumptions and parameters with inherent uncertainties. In this project we coupled state-of-the-art Uncertainty Quantification (UQ) methods developed at Sandia to analyze model uncertainties in high-fidelity LES. This has never been done before (and is rarely done in the community) as classical UQ methods require thousands of computational runs that cannot be provided by LES alone for cost reasons. The main idea of the present project is to use a limited number of LES computations to build a "surrogate" that possesses the same behavior as the solver in the parameter space of interest. Here the parameter space is three-dimensional as three uncertain quantities are considered: the Smagorinsky coefficient and the turbulent Prandtl and Schmidt numbers. To minimize the cost of the construction of the surrogate, a sparse quadrature method has been employed to provide the points to compute in the parameter space. Then the surrogate is used to perform a global sensitivity study of the three input parameters using methods derived from Monte Carlo methods which requires hundreds of thousands of samples. This is why a surrogate is used as

running directly 10^5 runs is impossible with LES. The study provided unintuitive insights of the coupling between models. This work proved that non-intrusive methods and high-performance computing can enable relevant UQ analysis in a LES context to study the complex interaction between errors. UQ is also used in the present context to develop optimized chemistry models to predict complex ignition characteristics in diesel engines while keeping the computational cost at an affordable level. Using these models, we are able to keep very refined computational grid and control the balance between the accuracy of the different models. This project has provided the foundation for a new avenue of research for LES. In addition. it has provided a strong link with UQ experts at the CRF and elsewhere. This, in turn, is expected to strengthen our ability to solicit funding from external sources to further our research in this area.

This page intentionally left blank.

References

[1] B. Dally, A. Masri, R. Barlow, G. Fiechtner, Instantaneous and mean compositional structure of bluff-body stabilized nonpremixed flames, Combustion and Flame 114 (1-2) (1998) 119–148.

[2] S. A. Skeen, J. Manin, L. M. Pickett, Simultaneous formaldehyde plif and high-speed schlieren imaging for ignition visualization in high-pressure spray flames, Proceedings of the Combustion Institute (2014) 3167–3174.

[3] Z. Luo, S. Som, S. M. Sarathy, M. Plomer, W. J. Pitz, D. E. Longman, T. Lu, Development and validation of an n-dodecane skeletal mechanism for diesel spray-combustion applications, Combustion Theory and Modelling 18 (2) (2014) 187–203.

[4] J. Meyers, B. J. Geurts, M. Baelmans, Database analysis of errors in large-eddy simulation, Physics of Fluids 15 (9) (2003) 2740–2755, doi: 10.1063/1.1597683.

[5] J. Meyers, P. Sagaut, B. J. Geurts, Optimal model parameters for multi-objective large-eddy simulations, Physics of Fluids 18 (095103) (2006) 1–12, doi: 10.1063/1.2353402.

[6] A. Kempf, B. Geurts, J. Oefelein, Error analysis of large-eddy simulation of the turbulent non-premixed sydney bluff-body flame, Combustion and Flame 158 (12) (2011) 2408–2419.

[7] A. Cook, J. Riley, G. Kosály, A laminar flamelet approach to subgrid-scale chemistry in turbulent flows, Combustion and Flame 109 (3) (1997) 332–341.

[8] R. Rebba, S. Mahadevan, S. Huang, Validation and error estimation of computational models, Reliability Engineering & System Safety 91 (10) (2006) 1390–1397.

[9] P. J. Roache, Verification and validation in computational science and engineering, Hermosa, 1998.

[10] I. Celik, O. Karatekin, Numerical experiments on application of richardson extrapolation with nonuniform grids, Journal of fluids engineering 119 (3) (1997) 584–590.

[11] I. B. Celik, J. Li, Assessment of numerical uncertainty for the calculations of turbulent flow over a backward-facing step, International journal for numerical methods in fluids 49 (9) (2005) 1015–1031.

[12] L. Eça, M. Hoekstra, On the grid sensitivity of the wall boundary condition of the k-ω turbulence model, Journal of fluids engineering 126 (6) (2004) 900–910.

[13] F. Stern, R. Wilson, J. Shao, Quantitative v&v of cfd simulations and certification of cfd codes, International journal for numerical methods in fluids 50 (11) (2006) 1335–1355.

[14] F. M. Hemez, Uncertainty quantification and the verification and validation of computational models, Damage Prognosis for Aerospace, Civil and Mechanical Systems (2005) 201–220.

[15] J. Zádor, I. G. Zsely, T. Turányi, Local and global uncertainty analysis of complex chemical kinetic systems, Reliability Engineering & System Safety 91 (10) (2006) 1232–1240.

[16] Y. M. Marzouk, H. N. Najm, L. A. Rahn, Stochastic spectral methods for efficient Bayesian solution of inverse probelms, Journal of Computational Physics 224 (2) (2007) 560–586.

[17] M. Khalil, G. Lacaze, J. C. Oefelein, H. N. Najm, Uncertainty quantification in les of a turbulent bluff-body stabilized flame, Proceedings of the Combustion Institute 35 (2) (2015) 1147–1156.

[18] N. Wiener, The homogeneous chaos, Am. J. Math. 60 (1938) 897–936.

[19] B. Debusschere, H. Najm, P. Pébay, O. Knio, R. Ghanem, O. Le Maître, Numerical challenges in the use of polynomial chaos representations for stochastic processes, SIAM Journal on Scientific Computing 26 (2) (2004) 698–719.

[20] X. Zhang, D. Pelletier, J.-Y. Tré, panier, R. Camarero, Numerical assessment of error estimators for euler equations, AIAA journal 39 (9) (2001) 1706–1715.

[21] S. E. Gant, Reliability issues of les-related approaches in an industrial context, Flow, turbulence and combustion 84 (2) (2010) 325–335.

[22] J. C. Oefelein, Thermophysical characteristics of shear-coaxial lox–h2 flames at supercritical pressure, Proc. Combust. Inst. 30 (2) (2005) 2929–2937.

[23] J. Oefelein, Mixing and combustion of cryogenic oxygen-hydrogen shear-coaxial jet flames at supercritical pressure, Combust. Sci. Tech. 178 (1-3) (2006) 229–252.

[24] J. C. Oefelein, Large eddy simulation of turbulent combustion processes in propulsion and power systems, Progress in Aerospace Sciences 42 (1) (2006) 2–37.

[25] J. Oefelein, V. Yang, Modeling high-pressure mixing and combustion processes in liquid rocket engines, J. Prop. Power 14 (5).

[26] J. Oefelein, V. Yang, Special issue: Supercritical fluid transport and combustion, Combust. Sci. Tech. 178 (1-3).

[27] M. Oschwald, J. J. Smith, R. Branam, J. Hussong, A. Schik, B. Chehroudi, D. Talley, Injection of fluids into supercritical environments, Combust. Sci. Tech. 178 (2006) 49–100.

[28] B. Chehroudi, Recent experimental efforts on high-pressure supercritical injection for liquid rockets and their implications, International Journal of Aerospace Engineering 2012.

[29] W. Mayer, J. Tellar, R. Branam, G. Schneider, J. Hussong, Raman measurement of cryogenic injection at supercritical pressure, Heat and Mass Transfer 39 (2003) 709–719.

[30] M. Oschwald, Supercritical nitrogen free jet investigated by spontaneous raman scattering, Experiments in Fluids 27 (1999) 497–506.

[31] M. Oschwald, M. Micci, Spreading angle and centerline variation of density of supercritical nitrogen jets, Atomization and Sprays 12 (1-3) (2002) 91–106.

[32] B. Chehroudi, R. Cohn, D. Talley, Cryogenic shear layers: Experiments and phenomenological modeling of the initial growth rate under subcritical and supercritical conditions, International Journal of Heat and Fluid Flow 23 (2002) 554–563.

[33] D. Davis, B. Chehroudi, Measurements in an acoustically driven coaxial jet under sub-, near-, and supercritical conditions, Journal of propulsion and power 23 (2) (2007) 364–374.

[34] H. Eroglu, N. Chigier, Z. Farago, Coaxial atomizer liquid intact lengths, Physics of Fluids A: Fluid Dynamics 3 (1991) 303.

[35] I. Leyva, B. Chehroudi, D. Talley, Dark core analysis of coaxial injectors at sub-, near-, and supercritical conditions in a transverse acoustic field, in: 43rd AIAA Joint Propulsion Conference and Exhibit, 2007, pp. 4342–4359.

[36] J. Locke, S. Pal, R. Woodward, R. Santoro, High speed visualization of lox/gh2 rocket injector flowfield: Hot-fire and cold-flow experiments, in: Proc. of 46th AIAA/ASME/SAE/ASEE Jt Propuls Conference Exhib, AIAA, 2010, pp. 1–18.

[37] A. Roy, C. Segal, C. Joly, Spreading angle and core length analysis of supercritical jets, AIAA journal 51 (8) (2013) 2009–2014.

[38] J. Bellan, Supercritical (and subcritical) fluid behavior and modeling: drops, streams, shear and mixing layers, jets and sprays, Progress in energy and combustion science.

[39] R. S. Miller, K. G. Harstad, J. Bellan, Direct numerical simulations of supercritical fluid mixing layers applied to heptane-nitrogen, Journal of Fluid Mechanics 436 (2001) 1–39.

[40] N. Okong'o, J. Bellan, Consistent boundary conditions for multicompoment real gas mixtures based on characteristic waves, J. Comput. Phys. 176 (2002) 330–344.

[41] J. Bellan, Theory, modeling and analysis of turbulent supercritical mixing, Combust. Sci. Tech. 178 (2006) 253–281.

[42] J. Foster, R. S. Miller, A priori analysis of subgrid mass diffusion vectors in high pressure turbulent hydrogen/oxygen reacting shear layer flames, Phys. Fluids 24 (7) (2012) 75114.

[43] L. C. Selle, N. A. Okong'o, J. Bellan, K. G. Harstad, Modelling of subgrid-scale phenomena in supercritical transitional mixing layers: An a priori study, J. Fluid Mech. 593 (2007) 57–91.

[44] E. S. Taskinoglu, J. Bellan, A posteriori study using a dns database describing fluid disintegration and binary-species mixing under supercritical pressure: heptane and nitrogen, J. Fluid Mech. 645 (1) (2010) 211–254.

[45] J. Oefelein, A perspective on les and its application to liquid rocket combustion systems (2001).

[46] N. Zong, H. Meng, S.-Y. Hsieh, V. Yang, A numerical study of cryogenic fluid injection and mixing under supercritical conditions, Physics of Fluids 16 (2004) 4248–4261.

[47] N. Zong, V. Yang, Cryogenic fluid jets and mixing layers in transcritical and supercritical environments, Combust. Sci. Tech. 178 (2006) 193–227.

[48] N. Zong, V. Yang, Near-field flow and flame dynamics of lox/methane shear-coaxial injector under supercritical conditions, Proceedings of the Combustion Institute 31 (2) (2007) 2309–2317.

[49] T. Schmitt, L. Selle, B. Cuenot, T. Poinsot, Large-eddy simulation of transcritical flows, Comptes Rendus Mécanique 337 (6-7) (2009) 528–538.

[50] T. Schmitt, L. Selle, A. Ruiz, B. Cuenot, Large-eddy simulation of supercritical-pressure round jets, AIAA Journal 48 (9) (2010) 2133–2144.

[51] T. Schmitt, Y. Méry, M. Boileau, S. Candel, Large-eddy simulation of oxygen/methane flames under transcritical conditions, Proceedings of the Combustion Institute In Press, Corrected Proof (2010) –.

[52] T. Schmitt, J. Rodriguez, I. Leyva, S. Candel, Experiments and numerical simulation of mixing under supercritical conditions, Physics of Fluids 24 (5) (2012) 055104–055104.

[53] H. Terashima, M. Koshi, Approach for simulating gas-liquid-like flows under supercritical pressures using a high-order central differencing scheme, Journal of Computational Physics.

[54] H. Terashima, S. Kawai, N. Yamanishi, High-resolution numerical method for supercritical flows with large density variations, AIAA journal 49 (12) (2011) 2658–2672.

[55] B. Chehroudi, D. Talley, E. Coy, Visual characteristics and initial growth rate of round cryogenic jets at subcritical and supercritical pressures, Physics of Fluids 14 (2) (2002) 850–861.

[56] E. Villermaux, H. Rehab, Mixing in coaxial jets, Journal of Fluid Mechanics 425 (1) (2000) 161–185.

[57] L. Selle, G. Lartigue, T. Poinsot, R. Koch, K.-U. Schildmacher, W. Krebs, B. Prade, P. Kaufmann, D. Veynante, Compressible large-eddy simulation of turbulent combustion in complex geometry on unstructured meshes, Combust. Flame 137 (4) (2004) 489–505.

[58] S. Roux, G. Lartigue, T. Poinsot, U. Meier, C. Bérat, Studies of mean and unsteady flow in a swirled combustor using experiments, acoustic analysis and large eddy simulations, Combust. Flame 141 (2005) 40–54.

[59] P. Wolf, G. Staffelbach, L. Y. Gicquel, J.-D. Müller, T. Poinsot, Acoustic and large eddy simulation studies of azimuthal modes in annular combustion chambers, Combustion and Flame.

[60] O. Vermorel, S. Richard, O. Colin, C. Angelberger, A. Benkenida, D. Veynante, Towards the understanding of cyclic variability in a spark ignited engine using multi-cycle LES, Combust. Flame 156 (8) (2009) 1525–1541.

[61] B. Enaux, V. Granet, O. Vermorel, C. Lacour, C. Pera, C. Angelberger, T. Poinsot, Les and experimental study of cycle-to-cycle variations in a spark ignition engine, Proc. Combust. Inst. 33 (2011) 3115–3122.

[62] A. Roux, L. Y. M. Gicquel, S. Reichstadt, N. Bertier, G. Staffelbach, F. Vuillot, T. Poinsot, Analysis of unsteady reacting flows and impact of chemistry description in large eddy simulations of side-dump ramjet combustors, Combust. Flame 157 (2010) 176–191.

[63] N. Gourdain, L. Gicquel, M. Montagnac, O. Vermorel, M. Gazaix, G. Staffelbach, M. García, J.-F. Boussuge, T. Poinsot, High performance parallel computing of flows in complex geometries - part 1: methods, Computational Science and Discovery 2 (November) (2009) 015003 (26pp).

[64] N. Gourdain, L. Gicquel, G. Staffelbach, O. Vermorel, F. Duchaine, J.-F. Boussuge, T. Poinsot, High performance parallel computing of flows in complex geometries - part 2: applications, Computational Science and Discovery 2 (November) (2009) 015004 (28pp).

[65] D. Papamoschou, A. Roshko, The compressible turbulent shear layer: an experimental study, J. Fluid Mech. 197 (1988) 453–477.

[66] L. Raynal, Instabilite et entrainement a l'interface d'une couche de melange liquide-gaz., Ph.D. thesis, Universite Joseph Fourier, Grenoble (1997).

[67] A. Ruiz, Unsteady numerical simulations of transcritical turbulent combustion in liquid rocket engines, Ph.D. thesis, Institut National Polytechnique de Toulouse (2012).

[68] A. Ruiz, G. Lacaze, J. C. Oefelein, R. Mari, B. Cuenot, L. Selle, T. Poinsot, A numerical benchmark for validation of high reynolds number supercritical flows with large density gradients, AIAA Journal 42 (1) (2015) 2–37.

[69] J. Jeong, F. Hussain, On the identification of a vortex, Journal of Fluid Mechanics 285 (69) (1995) 69–94.

[70] R. H. Kraichnan, Inertial ranges in two dimensional turbulence, Phys. Fluids 10 (7) (1967) 1417–1423.

[71] G. K. Batchelor, Computation of the energy spectrum in homogeneous two dimensional turbulence, Phys. Fluids 12 (12) (1969) II–233–II–239.

[72] M. Rutgers, Forced 2d turbulence: experimental evidence of simultaneous inverse energy and forward enstrophy cascades, Physical review letters 81 (11) (1998) 2244–2247.

[73] P. Marmottant, E. Villermaux, et al., On spray formation, Journal of Fluid Mechanics 498 (1) (2004) 73–111.

[74] J.-P. Matas, S. Marty, A. Cartellier, Experimental and analytical study of the shear instability of a gas-liquid mixing layer, Physics of Fluids 23 (9) (2011) 094112.

[75] R. J. Margason, Fifty years of jet in cross flow research, in: In AGARD, Computational and Experimental Assessment of Jets in Cross Flow 41 p (SEE N94-28003 07-34), Vol. 1, 1993, pp. 7 – 34.

[76] S. Muppidi, K. Mahesh, Direct numerical simulation of round turbulent jets in crossflow, Journal of Fluid Mechanics 574 (2007) 59–84.

[77] S. Muppidi, K. Mahesh, Direct numerical simulation of passive scalar transport in transverse jets, Journal of Fluid Mechanics 598 (2008) 335–360.

[78] J. Ling, F. Coletti, S. D. Yapa, J. K. Eaton, Experimentally informed optimization of turbulent diffusivity for a discrete hole film cooling geometry, International Journal of Heat and Fluid Flow 44 (2013) 348–357.

[79] L. L. Yuan, R. L. Street, Trajectory and entrainment of a round jet in crossflow, Physics of Fluids 10 (1998) 2323.

[80] J. Schlüter, T. Schönfeld, Les of jets in cross flow and its application to a gas turbine burner, Flow, Turbulence and Combustion 65 (2) (2000) 177–203.

[81] X. Guo, W. Schröder, M. Meinke, Large-eddy simulations of film cooling flows, Computers & Fluids 35 (6) (2006) 587 – 606.

[82] P. Renze, W. Schröder, M. Meinke, Large-eddy simulation of film cooling flows at density gradients, International Journal of Heat and Fluid Flow 29 (1) (2008) 18 – 34.

[83] A. Rozati, D. K. Tafti, Large-eddy simulations of leading edge film cooling: Analysis of flow structures, effectiveness, and heat transfer coefficient, International Journal of Heat and Fluid Flow 29 (1) (2008) 1 – 17.

[84] S. Mendez, F. Nicoud, et al., Large-eddy simulation of a bi-periodic turbulent flow with effusion, Journal of Fluid Mechanics 598 (2008) 27–66.

[85] A. R. Karagozian, Transverse jets and their control, Progress in Energy and Combustion Science 36 (5) (2010) 531 – 553.

[86] K. Mahesh, The interaction of jets with crossflow, Annual Review of Fluid Mechanics 45 (2013) 379–407.

[87] S. Smith, M. Mungal, Mixing, structure and scaling of the jet in crossflow, Journal of Fluid Mechanics 357 (1) (1998) 83–122.

[88] J. W. Shan, P. E. Dimotakis, Reynolds-number effects and anisotropy in transverse-jet mixing, Journal of Fluid Mechanics 566 (2006) 47–96.

[89] L. Su, M. Mungal, Simultaneous measurements of scalar and velocity field evolution in turbulent crossflowing jets, Journal of fluid mechanics 513 (1) (2004) 1–45.

[90] J. Eggels, F. Unger, M. Weiss, J. Westerweel, R. Adrian, R. Friedrich, F. Nieuwstadt, Fully developed turbulent pipe flow: a comparison between direct numerical simulation and experiment, Journal of Fluid Mechanics 268 (1) (1994) 175–209.

[91] U. Filobello-Nino, H. Vazquez-Leal, R. Castaneda-Sheissa, A. Yildirim, L. Hernandez-Martinez, D. Pereyra-Diaz, A. Perez-Sesma, C. Hoyos-Reyes, An approximate solution of blasius equation by using hpm method., Asian Journal of Mathematics & Statistics 5 (2).

[92] P. Freymuth, On transition in a separated laminar boundary layer, Journal of Fluid Mechanics 25 (04) (1966) 683–704.

[93] H. Becker, T. Massaro, Vortex evolution in a round jet, Journal of fluid mechanics 31 (03) (1968) 435–448.

[94] T. Fric, A. Roshko, Vortical structure in the wake of a transverse jet, Journal of Fluid Mechanics 279 (1994) 1–47.

[95] G. Broze, F. Hussain, Transitions to chaos in a forced jet: intermittency, tangent bifurcations and hysteresis, Journal of Fluid Mechanics 311 (1996) 37–71.

[96] C. da SILVA, O. Métais, On the influence of coherent structures upon interscale interactions in turbulent plane jets, Journal of Fluid Mechanics 473 (2002) 103–145.

[97] L. L. Yuan, R. L. Street, J. H. Ferziger, Large-eddy simulations of a round jet in crossflow, Journal of Fluid Mechanics 379 (1999) 71–104.

[98] M. S. Uberoi, P. Freymuth, Turbulent energy balance and spectra of the axisymmetric wake, Phys. Fluids 13 (9) (1970) 2205–2210.

[99] P. D. Welch, The use of fast fourier transform for the estimation of power spectra: a method based on time averaging over short, modified periodograms, IEEE Transactions on audio and electroacoustics 15 (2) (1967) 70–73.

[100] J. Smagorinsky, General circulation experiments with the primitive equations. I. The basic experiment, Monthly Weather Review 91 (1963) 99–164.

[101] D. K. Lilly, On the application of the eddy viscosity concept in the inertial subrange of turbulence, Tech. Rep. NCAR-123, National Center for Atmospheric Research, Boulder, Colorado (1966).

[102] S. B. Pope, Turbulent Flows, Cambridge University Press, Cambridge, United Kingdom, 2000.

[103] S. Ghosal, An analysis of numerical errors in large eddy simulation of turbulence, J. Comput. Phys. 125 (1996) 187–206.

[104] B. J. Geurts, J. Fröhlich, A framework for predicting accuracy limitations in large-eddy simulation, Physics of Fluids 14 (6) (2002) 41–44, doi: 10.1063/1.1480830.

[105] J. Meyers, P. Sagaut, On the model coefficients for the standard and the variational multi-scale smagorinsky model, J. Fluid Mech. 569 (2006) 287–319.

[106] M. Mueller, G. Iaccarino, H. Pitsch, Chemical kinetic uncertainty quantification for Large Eddy Simulation of turbulent nonpremixed combustion, in: Thirty-Fourth Symposium (International) on Combustion, Vol. 34, The Combustion Institute, 2013, pp. 1299–1306.

[107] D. Lucor, J. Meyers, P. Sagaut, Sensitivity analysis of large-eddy simulations to subgrid-scale-model parametric uncertainty using polynomial chaos, Journal of Fluid Mechanics 585 (2007) 255–279.

[108] J. Warnatz, Resolution of gas phase and surface combustion chemistry into elementary reactions, in: Twenty-Fourth Symposium (International) on Combustion, Vol. 24, The Combustion Institute, 1992, pp. 553–579.

[109] M. Smooke, H. Rabitz, Y. Reuven, F. Dryer, Application of sensitivity analysis to premixed Hydrogen-Air flames, Combustion Science and Technology 59 (1988) 295–319.

[110] F. Duchaine, F. Boudy, D. Durox, T. Poinsot, Sensitivity analysis of transfer functions of laminar flames, Combustion and Flame 158 (12) (2011) 2384–2394.

[111] R. Ghanem, P. Spanos, Stochastic Finite Elements: A Spectral Approach, Springer Verlag, New York, 1991.

[112] D. Xiu, G. Karniadakis, The Wiener-Askey polynomial chaos for stochastic differential equations, SIAM Journal on Scientific Computing 24 (2) (2002) 619–644.

[113] H. Najm, Uncertainty Quantification and Polynomial Chaos Techniques in Computational Fluid Dynamics, Annual Review of Fluid Mechanics 41 (1) (2009) 35–52.

[114] O. L. Maître, O. Knio, Spectral Methods for Uncertainty Quantification: With Applications to Computational Fluid Dynamics (Scientific Computation), 1st Edition, Springer, 2010.

[115] O. Ernst, A. Mugler, H.-J. Starkloff, E. Ullmann, On The Convergence of Generalized Polynomial Chaos Expansions, ESAIM: Mathematical Modelling and Numerical Analysis 46 (2012) 317–339.

[116] R. Ghanem, Hybrid Stochastic Finite Elements and Generalized Monte Carlo Simulation, ASME Journal of Applied Mechanics 65 (1998) 1004–1009.

[117] O. Le Maître, M. Reagan, H. Najm, R. Ghanem, O. Knio, A stochastic projection method for fluid flow II. Random process, Journal of Computational Physics 181 (2002) 9–44.

[118] F. Nobile, R. Tempone, C. Webster, A sparse grid stochastic collocation method for partial differential equations with random input data, SIAM Journal on Numerical Analysis 46 (5) (2008) 2309–2345.

[119] G. D. Wyss, K. H. Jorgensen, A user's guide to LHS: Sandia's latin hypercube sampling software, Tech. rep., Sandia Technical Report SAND98-0210 (February 1998).

[120] A. Masri, B. Dally, R. Barlow, C. Carter, The structure of the recirculation zone of a bluff-body combustor, in: Symposium (International) on Combustion, Vol. 25, Elsevier, 1994, pp. 1301–1308.

[121] B. Dally, D. Fletcher, A. Masri, Flow and mixing fields of turbulent bluff-body jets and flames, Combustion Theory and Modelling 2 (2) (1998) 193–219.

[122] U. Piomelli, J. Ferziger, P. Moin, J. Kim, New approximate boundary conditions for large eddy simulations of wall-bounded flows, Physics of Fluids A: Fluid Dynamics 1 (1989) 1061.

[123] G. Erlebacher, M. Hussaini, C. Speziale, T. Zang, Toward the large-eddy simulation of compressible turbulent flows, Journal of Fluid Mechanics 238 (1) (1992) 155–185.

[124] A. Reynolds, The variation of turbulent prandtl and schmidt numbers in wakes and jets, International Journal of Heat and Mass Transfer 19 (7) (1976) 757–764.

[125] A. Saltelli, K. Chan, M. Scott (Eds.), Sensitivity Analysis, Wiley, Chichester, 2000.

[126] A workshop to identify research needs and impacts in predictive simulation for internal combustion engines (PreSICE), http://science.energy.gov/bes/news-and-resources/reports/, sponsored by the U.S. Department of Energy, Office of Science – Basic Energy Sciences Program and Office of Energy Efficiency and Renewable Energy – Vehicle Technologies Program (March 2011).

[127] R. N. Dahms, J. Manin, L. M. Pickett, J. C. Oefelein, Understanding high-pressure gas-liquid interface phenomena in diesel engines, Proceedings of the Combustion Institute 34 (2013) 1667–1675.

[128] R. N. Dahms, J. C. Oefelein, On the transition between two-phase and single-phase interface dynamics in multicomponent fluids at supercritical pressures, Physics of Fluids 25 (092103) (2013) 1–24.

[129] J. Manin, M. Bardi, L. M. Pickett, R. N. Dahms, J. C. Oefelein, Microscopic investigation of the atomization and mixing processes of diesel sprays injected into high pressure and temperature environments, Fuel 134 (2014) 531–543.

[130] J. Oefelein, G. Lacaze, R. Dahms, A. Ruiz, A. Misdariis, Effects of real-fluid thermodynamics on high-pressure fuel injection processes, SAE International Journal of Engines 7 (3) (2014) 1–12.

[131] G. Lacaze, A. Misdariis, A. Ruiz, J. C. Oefelein, Analysis of high-pressure diesel fuel injection processes using LES with real-fluid thermodynamics and transport, Proceedings of the Combustion InstituteAccepted.

[132] R. N. Dahms, J. C. Oefelein, Non-equilibrium gas-liquid interface dynamics in high-pressure liquid injection systems, Proceedings of the Combustion InstituteAccepted.

[133] L. M. Pickett, Engine combustion network, www.sandia.gov/ECN, Sandia National Laboratories, Combustion Research Facility, Livermore, California (2005-2014).

[134] A. Gelman, J. B. Carlin, H. S. Stern, D. B. Dunson, A. Vehtari, D. B. Rubin, Bayesian data analysis, CRC press, 2013.

[135] D. S. Sivia, J. Skilling, Data Analysis: A Bayesian Tutorial, Oxford University Press, 2006.

[136] A. Mohammad-Djafari, Bayesian inference for inverse problems, in: Bayesian inference and Maximum Entropy Methods in Science and Engineering, Vol. 617, AIP Publishing, 2002, pp. 477–496.

[137] A. L. Sánchez, A. Lépinette, M. Bollig, A. Liñán, B. Lázaro, The reduced kinetic description of lean premixed combustion, Combustion and flame 123 (4) (2000) 436–464.

[138] E. Fernández-Tarrazo, A. L. Sánchez, A. Liñán, F. A. Williams, A simple one-step chemistry model for partially premixed hydrocarbon combustion, Combustion and Flame 147 (1D2) (2006) 32 – 38.

[139] B. Franzelli, E. Riber, M. Sanjose, T. Poinsot, A two-step chemical scheme for large eddy simulation of kerosene-air flames, Combustion and Flame 157 (2010) 1364–1373.

[140] A. Misdariis, O. Vermorel, T. Poinsot, A methodology based on reduced schemes to compute autoignition and propagation in internal combustion engines, in: Proceedings of the Combustion Institute, Vol. 35, 2015, pp. 3001–3008.

[141] C. K. Westbrook, F. L. Dryer, Simplified reaction mechanisms for the oxidation of hydrocarbon fuels in flames, Combustion Science and Technology 27 (1981) 31–43.

[142] F. L. Dryer, I. Glassman, High-temperature oxidation of CO and CH_4, in: Proceedings of the Combustion Institute, Vol. 14, 1973, pp. 987–1003.

[143] S. Conti, C. W. Anderson, M. C. Kennedy, A. O'Hagan, A bayesian analysis of complex dynamic computer models, in: Proc. of the 4th International Conference on Sensitivity Analysis of Model Output, 2004, pp. 147 – 156.

[144] C. K. Westbrook, W. J. Pitz, O. Herbinet, H. J. Curran, E. J. Silke, A comprehensive detailed chemical kinetic reaction mechanism for combustion of n-alkane hydrocarbons from n-octane to n-hexadecane, Combustion and Flame 156 (1) (2009) 181–199.

[145] M. Bardi, R. Payri, L. Malbec, G. Bruneaux, L. Pickett, J. Manin, T. Bazyn, C. Genzale, Engine combustion network: Comparison of spray and combustion characterization in different combustion vessels, Atomization and Sprays 22 (10) (2012) 807–842.

[146] G. Smith, D. Golden, M. Frenklach, N. Moriarty, B. Eiteneer, M. Goldenberg, C. Bowman, R. Hanson, S. Song, W. Gardiner Jr, L. V.V., Q. Z., Gri-mech 3.0 (1999), URL http://www.me. berkeley. edu/gri_mech/. Last visited Nov. 2013.

[147] N. Peters, Turbulent combustion, Cambridge University Press, 2000.

[148] Y. Choi, C. L. Merkle, Time-derivative preconditioning for viscous flows, Sverdrup Technology, Incorporated, Lewis Research Center Group, 1991.

[149] A. Karagozian, An analytical model for the vorticity associated with a transverse jet, AIAA journal 24 (3) (1986) 429–436.

[150] S. Muppidi, K. Mahesh, Study of trajectories of jets in crossflow using direct numerical simulations, Journal of Fluid Mechanics 530 (5) (2005) 81–100.

[151] S. Muppidi, K. Mahesh, Two-dimensional model problem to explain counter-rotating vortex pair formation in a transverse jet, Physics of Fluids (1994-present) 18 (8) (2006) 085103.

[152] R. J. Margason, The path of a jet directed at large angles to a subsonic free stream, National Aeronautics and Space Administration, 1968.

[153] R. H. Kraichnan, Inertial-range transfer in two and three dimensional turbulence, J. Fluid Mech. 47 (1971) 525–535.

[154] C. Pantano, Direct simulation of non-premixed flame extinction in a methane–air jet with reduced chemistry, Journal of Fluid Mechanics 514 (2004) 231–270.

[155] P. E. Dimotakis, R. C. Miake-Lye, D. A. Papantoniou, Structure and dynamics of round turbulent jets, Physics of Fluids 26 (11) (1983) 3185–3192.

[156] B. Hu, M. P. Musculus, J. C. Oefelein, The influence of large-scale structures on entrainment in a decelerating transient turbulent jet revealed by large eddy simulation, Physics of Fluids 24 (2012) 045106.

[157] H. Terashima, S. Kawai, N. Yamanishi, A high-resolution numerical method for supercritical flows with large density variations, AIAA Journal .

[158] A. Roy, C. Segal, Experimental study of fluid jet mixing at supercritical conditions, Journal of propulsion and power 26 (6) (2010) 1205–1211.

[159] I. Leyva, Dark core analysis of coaxial injectors at sub-, near-, and supercritical conditions in a transverse acoustic field, Tech. rep., DTIC Document (2007).

[160] B. Chehroudi, D. Talley, E. Coy, Fractal geometry and growth rate changes of cryogenic jets near the critical point, in: 35th Joint Propulsion Conference, Los Angeles, CA, Vol. AIAA 99-2489, 1999, pp. 1–13.

[161] G. Searby, A. Nicole, M. Habiballah, E. Laroche, Prediction of the efficiency of acoustic damping cavities, J. Prop. Power 24 (3) (2008) 516–523.

[162] B. Knapp, Z. Farago, M. Oschwald, Interaction of LOX/GH2-Spray Combustion with Acoustics, in: 45th AIAA, Reno, NV, 2007, pp. 1–9.

[163] B. Chehroudi, Physical Hypothesis for the Combustion Instability in Cryogenic Liquid Rocket Engines, J. Prop. Power 26 (6) (2010) 1153–1160.

[164] V. Yang, W. Anderson, Liquid rocket engine combustion instability, Aiaa, 1995.

[165] D. Harrje, F. Reardon, Liquid propellant rocket instability, Tech. Rep. Report SP-194, NASA (1972).

[166] B. Van Leer, Towards the ultimate conservative difference scheme IV. A new approach to numerical convection, J. Comput. Phys. 23 (1977) 276–299.

[167] P. Jorgenson, E. Turkel, Central difference tvd schemes for time dependent and steady state problems, Journal of Computational Physics 107 (2) (1993) 297 – 308.

[168] G. Ribert, N. Zong, V. Yang, L. Pons, N. Darabiha, S. Candel, Counterflow diffusion flames of general fluids: Oxygen/hydrogen mixtures, Combustion and Flame 154 (2008) 319–330.

[169] M. Klein, A. Sadiki, J. Janicka, A digital filter based generation of inflow data for spatially developing direct numerical or large eddy simulations, Journal of Computational Physics 186 (2) (2003) 652–665.

[170] G. Van Albada, B. Van Leer, W. Roberts Jr, A comparative study of computational methods in cosmic gas dynamics, Springer, 1997.

[171] B. Van Leer, Towards the ultimate conservative difference scheme. ii. monotonicity and conservation combined in a second-order scheme, Journal of Computational Physics 14 (4) (1974) 361 – 370.

[172] R. C. Swanson, E. Turkel, On central-difference and upwind schemes, J. Comput. Phys. 101 (2) (1992) 292 – 306.

[173] P. Roe, Approximate riemann solvers, parameter vectors and difference schemes, J. Comput. Phys. 43 (1981) 357–372.

[174] P. Roe, Characteristic-based schemes for the euler equations, Annual review of fluid mechanics 18 (1) (1986) 337–365.

[175] F. Harlow, J. Welch, Numerical calculation of time-dependent viscous incompressible flow of fluid with free surface, Phys. Fluids 8 (12) (1965) 2182–2189.

[176] A. L. Gaitonde, A dual time method for two dimensional unsteady incompressible flow calculations, International journal for numerical methods in engineering 41 (6) (1998) 1153–1166.

[177] A. Jameson, W. Schmidt, E. Turkel, Numerical solution of the euler equations by finite volume methods using runge-kutta time stepping schemes, in: A. p. 81-1259 (Ed.), 14th Fluid and Plasma Dynamic Conference, Palo Alto, 1981, pp. 1–19, ref lolo.

[178] J. M. Weiss, W. A. Smith, Preconditioning applied to variable and constant density flows, AIAA journal 33 (11) (1995) 2050–2057.

[179] C. L. Venkateswaran, S.and Merkle, Dual time-stepping and preconditioning for unsteady computations, AIAA journal.

[180] P. Buelow, S. Venkateswaran, C. Merkle, Effect of grid aspect ratio on convergence, AIAA Journal 32 (12) (1994) 2401–2408.

[181] J. Withington, V. Yang, J. Shuen, A time-accurate implicit method for chemically reacting flows at all mach numbers, in: 29th AIAA Aerospace Sciences Meeting, Vol. 1, 1991, pp. 1–13.

[182] J. C. Oefelein, Simulation and analysis of turbulent multiphase combustion processes at high pressures, MI Dissertations Publishing, 1997.

[183] C. Merkle, A. M., Time-accurate unsteady incompressible flow algorithms based on artificial compressibility, in: 8th Computational Fluid Dynamics Conference, Vol. 32, 1987, pp. 2401–2408.

[184] Y. Choi, C. L. Merkle, The application of preconditioning in viscous flows, Journal of Computational Physics 105 (2) (1993) 207–223.

[185] S. Takahashi, Preparation of a generalized chart for the diffusion coefficients of gases at high pressures, journal of Chemical Engineering of Japan 7 (6) (1974) 417–420.

[186] J. Hirschfelder, F. Curtiss, R. Bird, Molecular theory of gases and liquids, John Wiley & Sons, New York, 1964.

[187] J. Ely, H. J. M. Hanley, Prediction of transport properties. 2. Thermal conductivity of pure fluids and mixtures, Industrial & Engineering Chemistry Fundamentals 22 (1) (1983) 90–97.

[188] R. C. Reid, J. M. Prausnitz, B. E. Polling, The properties of liquids and gases, Vol. fourth ed., McGraw Hill, New York, 1987.

[189] T. Poinsot, D. Veynante, Theoretical and numerical combustion, R.T. Edwards, 2nd edition., 2005.

DISTRIBUTION:

1	MS 0899	Technical Library, 8944 (electronic copy)
1	MS 0359	D. Chavez, LDRD Office, 1911

Sandia National Laboratories